
SCATTERING FROM ROUGH SURFACES WITH A VEGETATED COVER

B.A. Davis

R.J. Adams

G.S. Brown

ElectroMagnetic Interactions Laboratory

Brandley Department of Electrical and Computer Engineering

Virginia Polytechnic Institute & State University

Blacksburg VA 24061-0111

FINAL REPORT : June 1996 – June 1999

APPROVED FOR PUBLIC RELEASE: DISTRIBUTION UNLIMITED



AIR FORCE RESEARCH LABORATORY

Sensors Directorate

Electromagnetics Technology Division

80 Scott Dr

Hanscom AFB MA 01731-2909

20020827 040

REPORT DOCUMENTATION PAGE

Form Approved
OMB No. 0704-0188

Public reporting burden for this collection of information is estimated to average 1 hour per response, including the time for reviewing instructions, searching existing data sources, gathering and maintaining the data needed, and completing and reviewing the collection of information. Send comments regarding this burden estimate or any other aspect of this collection of information, including suggestions for reducing this burden, to Washington Headquarters Services, Directorate for Information Operations and Reports, 1215 Jefferson Davis Highway, Suite 1204, Arlington, VA 22202-4302, and to the Office of Management and Budget, Paperwork Reduction Project (0704-0188), Washington, DC 20503.

1. AGENCY USE ONLY (Leave blank)		2. REPORT DATE August 25, 1999	3. REPORT TYPE AND DATES COVERED Final Report June 1996 - June 1999	
4. TITLE AND SUBTITLE Scattering from Rough Surfaces with a Vegetated Cover			5. FUNDING NUMBERS C - F19628-96-C-0071 PE - 62702F PR - 4600 TA - 15 WU - 23	
6. AUTHOR(S) B.A. Davis, R.J. Adams, G.S. Brown				
7. PERFORMING ORGANIZATION NAME(S) AND ADDRESS(ES) ElectroMagnetic Interactions Laboratory Bradley Department of Electrical and Computer Engineering Virginia Polytechnic Institute & State University Blacksburg, VA 24061-0111			8. PERFORMING ORGANIZATION REPORT NUMBER	
9. SPONSORING/MONITORING AGENCY NAME(S) AND ADDRESS(ES) Air Force Research Laboratory AFRL/SNHE 80 Scott Road Hanscom AFB, MA 01731-2909			10. SPONSORING/MONITORING AGENCY REPORT NUMBER AFRL-SN-HS-TR-2002-012	
11. SUPPLEMENTARY NOTES				
12a. DISTRIBUTION AVAILABILITY STATEMENT Approved for public release; distribution unlimited			12b. DISTRIBUTION CODE A	
13. ABSTRACT (Maximum 200 words) This report summarizes the research to date on describing the incoherent pulse response of a foliage layer on top of a rough surface under conditions of a relatively narrowband, narrow beamwidth illumination. The incoherent impulse response for the foliage is developed in terms of a multi-convolutional description of the incoherent scattering process. The surface scattering is described by the MOMI-based numerical method. The interaction between a cylinder located above a rough surface is used to determine the separation distance for which the interaction between the foliage scattered fields and the rough surface may be ignored. The resulting model is designed to be matched to foliage scattering data in order to "calibrate" the model scattering parameters.				
14. SUBJECT TERMS FOPEN, wave propagation, terrain scattering, foliage shadowing			15. NUMBER OF PAGES 110	
			16. PRICE CODE	
17. SECURITY CLASSIFICATION OF REPORT UNCLASSIFIED	18. SECURITY CLASSIFICATION OF THIS PAGE UNCLASSIFIED	19. SECURITY CLASSIFICATION OF ABSTRACT UNCLASSIFIED	20. LIMITATION OF ABSTRACT UL	

Table of Contents

LIST OF FIGURES.....	V
INTRODUCTION AND SCOPE OF THE PROBLEM	1
1.1 FOLIAGE ABOVE A ROUGH SURFACE: AN APPROACH RATIONALE	1
1.2 THE MAJOR CONTRIBUTORS TO THE RETURN WAVEFORM.....	4
1.2.1 <i>Scattering from a Volume of Discrete, Closed Body Scatterers</i>	5
1.2.2 <i>Scattering from a Rough Surface</i>	7
1.2.3 <i>Interaction between the Foliage and the Rough Surface</i>	8
1.3 GOALS OF THIS RESEARCH.....	10
2 ESTIMATING THE ISOLATED SURFACE RETURN POWER.....	12
2.1 INTEGRAL EQUATION FORMULATION OF ROUGH SURFACE SCATTERING AND THE METHOD OF ORDERED MULTIPLE INTERACTIONS	12
2.2 THE INCOHERENT POWER VIA THE IMPULSE RESPONSE METHOD.....	17
3 ESTIMATING THE RETURN POWER COMPONENTS.....	21
3.1 INTRODUCTION TO THE USE OF A RADIATIVE TRANSFER APPROACH	21
3.2 DERIVATION OF A VOLUME/SURFACE IMPULSE RESPONSE APPROACH	22
3.3 INCOHERENT SCATTERED POWER: THE VOLUME (FOLIAGE) RETURN	28
3.4 INCOHERENT SCATTERED POWER: THE ROUGH SURFACE RETURN.....	34
4 INTERACTION BETWEEN THE FOLIAGE AND THE SURFACE	40
4.1 CAPABILITIES, LIMITATIONS AND AN EXAMPLE RETURN WAVEFORM FOR THE RADIATIVE TRANSFER APPROACH	44
4.2 MODIFIED SINGLE SCATTER THEORY FOR A SINGLE SCATTERER OVER A ROUGH SURFACE	49
4.2.1 <i>Introduction</i>	49
4.2.2 <i>Development of the Model</i>	51
4.2.3 <i>Conclusions and Future Efforts</i>	60
4.3 EXACT SOLUTION TO THE SINGLE SCATTERER ABOVE A ROUGH SURFACE	62
4.3.1 <i>Extension of the MOMI to Closed Bodies</i>	63
4.3.2 <i>A Combined Field Formulation</i>	66
4.3.3 <i>Selecting an optimal CFIE: A multiple scattering approach</i>	66
4.3.4 <i>Example Results for TE Polarization</i>	74
4.3.5 <i>Conclusions and Future Efforts</i>	79
4.4 APPROXIMATE ANALYTICAL SOLUTION FOR THE MOMENTS OF A SINGLE SCATTERER ABOVE A ROUGH SURFACE	83

4.4.1	<i>The Reduced Integral Representation.....</i>	84
4.4.2	<i>Reduction for a Circular Disk (3-D) Scatterer above a Rough Surface.....</i>	86
4.4.3	<i>Conclusions and Future Work.....</i>	89
5	CONCLUSIONS AND FUTURE ACTION	91
6	REFERENCES.....	ERROR! BOOKMARK NOT DEFINED.
7	APPENDIX A: FIRST ORDER MULTIPLE SCATTERING	96
7.1	REVIEW OF CLASSICAL SINGLE SCATTER THEORY	98
7.2	THE SCATTERED PULSE	102

List of Figures

FIGURE 1: THE INCIDENT FIELD	4
FIGURE 2: THE TOTAL INCIDENT FIELD WITH RESPECT TO THE SURFACE	6
FIGURE 3: SURFACE TO FOLIAGE INTERACTION	8
FIGURE 4: THE SECOND ORDER APPROXIMATE SCATTERED FIELD FROM THE FOLIAGE AND SURFACE COMBINATION	10
FIGURE 5: PROBLEM GEOMETRY FOR THE DERIVATION OF BOUNDARY INTEGRAL EQUATIONS	12
FIGURE 6: THE GEOMETRY FOR THE IMPULSE RESPONSE METHOD	17
FIGURE 7: THE GEOMETRY DESCRIBING THE VOLUME AND SURFACE. NOTE THAT DOTTED LINES INDICATE AVERAGE LEVELS FOR THE ASSOCIATED BOUNDARY.	22
FIGURE 8: SCATTERING GEOMETRY FOR THE INTENSITY [ISHIMARU, 1997].....	23
FIGURE 9: THE TOTAL INCIDENT FIELD WITH RESPECT TO THE SURFACE.....	40
FIGURE 10: THE FIRST ORDER APPROXIMATE SCATTERED FIELD FROM THE FOLIAGE AND SURFACE COMBINATION	41
FIGURE 11: THE SECOND ORDER APPROXIMATE SCATTERED FIELD FROM THE FOLIAGE AND SURFACE COMBINATION.....	42
FIGURE 12: COMPOSITE WAVEFORM FOR 1, 5 AND 10 DEGREE ANTENNA BEAMWIDTHS.....	47
FIGURE 13: COMPONENTS OF THE 1-DEGREE CASE: VOLUME + SURFACE RETURNS.....	47
FIGURE 14: COMPOSITE WAVEFORM FOR 1, 5 AND 10 DEGREE ANTENNA BEAMWIDTHS	48
FIGURE 15: COMPONENTS OF THE 1-DEGREE CASE: VOLUME + SURFACE RETURNS.....	48
FIGURE 16: PARTICLE AND SURFACE SCATTERING EVENTS.....	50
FIGURE 17: GEOMETRY FOR FOLIAGE-SURFACE-FOLIAGE SCATTERING EVENT.....	52
FIGURE 18: THE GEOMETRY OF THE SCATTERER.....	53
FIGURE 19 :ORDERING OF THE UNKNOWNNS	65
FIGURE 20: CONTOURS OF THE LARGEST EIGENVALUE OF P_M (IN DB) AS A FUNCTION OF THE COMPLEX CONSTANT α FOR CIRCULAR CYLINDERS	71
FIGURE 21: CONTOURS OF LARGEST EIGENVALUE OF P_M (IN DB) AS A FUNCTION OF THE COMPLEX CONSTANT α FOR CIRCULAR CYLINDERS.....	72
FIGURE 22: CONTOURS OF LARGEST EIGENVALUES OF P_M (IN DB) AS A FUNCTION OF THE COMPLEX CONSTANT α FOR ELLIPTICAL CYLINDERS HAVING $A/B = 8$	73
FIGURE 23: CONTOURS OF LARGEST EIGENVALUES OF P_M (IN DB) AS A FUNCTION OF THE COMPLEX CONSTANT α FOR ELLIPTICAL CYLINDERS HAVING $A/B = 8$	74
FIGURE 24: SCATTERER OVER A RANDOMLY ROUGH SURFACE.....	75
FIGURE 25: THE SINGLE SCATTER APPROXIMATION: (A) CURRENTS INDUCED ON THE	76
FIGURE 26: THE SINGLE SCATTER APPROXIMATION: (A) CORRECTIONS TO CURRENTS INDUCED ON THE SURFACE (B) CORRECTION TO CURRENTS INDUCED ON THE CYLINDER	77

FIGURE 27: 6 WAVELENGTH ELLIPSE, 60 WAVELENGTHS ABOVE A GAUSSIAN ROUGH SURFACE77

FIGURE 28: 6 WAVELENGTH ELLIPSE, 20 WAVELENGTHS ABOVE A GAUSSIAN ROUGH SURFACE78

FIGURE 29: 6 WAVELENGTH ELLIPSE, 5 WAVELENGTHS ABOVE A GAUSSIAN ROUGH SURFACE79

FIGURE 30: GEOMETRY FOR THE REDUCED INTEGRAL EQUATION APPROACH.....84

1 Introduction and Scope of the Problem

1.1 Foliage above a Rough Surface: An Approach Rationale

When studying scattering from the combination of a foliage layer above a rough surface, one must deal with the scattering from the foliage, the rough surface, and the interaction between the two. Of these three components to the fundamental scattering problem, the foliage scattering and the interaction scattering are definitely the most difficult to analyze.

Foliage by itself presents a real challenge to the analyst because of the many-body aspects of the problem. In addition, modeling foliage scattering from first principles is further complicated by the fact that the scatterers are irregular at best and generally ill defined. From an electromagnetic point of view, leaves do not all look to be identical and twigs, branches, and limbs conform to no particular shape! Thus, except for very low and very high frequency limits, it is almost impossible to compute the scattering pattern of the basic "constituents" of foliage. We do know a bit about the typical volume fraction of foliage and how this is partitioned between leaves and the woody components, and we have some idea of the range of complex dielectric constant variation for wood and leaf materials [1]. Yet another unknown is the variation of foliage density with depth into a canopy. Finally, even though foliage is quite frequently classified as on the edge of being a volumetrically sparse medium, this does not mean that there is a lack of strong electromagnetic interactions between the various scattering components, e.g., twigs, branches, leaves, etc. Furthermore, for European forests that have been well managed and not logged (also called old growth forests), the volume fractional density of the biomaterial may be as large as 5%.

When dealing with independently scattering objects and scattering from rough surfaces, it is possible to convert single-frequency models of the individual scattering cross sections (for the discrete objects) and the scattering cross section per unit area (for the extended surface scattering) into models for the incoherent time-dependent scattered waveform produced under pulse illumination. For strongly interacting individual scatterers, this simplification is not usually possible, the reason being that it is not sufficient to know that the scatterer is in a volume because its *location within the volume* must also be known.

What can be done then to resolve this dilemma? First, we know that we can always extract an effective "scattering cross section per unit illuminated volume, σ_v " from airborne radar data, e.g., the scattered power P_r received by a pulsed radar is given by

$$P_r = P_t \frac{G^2(\theta_i, \phi_i) \lambda^2}{(4\pi)^2 R^4} \sigma \quad (1)$$

where the effective scattering cross is given by

$$\sigma = (cT/2)(R\Phi_{az})(R\Theta_{el})\sigma_v \quad (2)$$

Solving (1) and (2) for σ_v yields

$$\sigma_v = \frac{P_r}{P_t} \frac{(4\pi)^2 R^2}{G^2(\theta_i, \phi_i) (cT/2)(\Phi_{az}\Theta_{el})} \quad (3)$$

In the above equations P_r is the received or scattered power, P_t is the transmitted power, $G^2(\theta_i, \phi_i)$ is the two-way antenna gain in the indicated direction, c is the speed of light, T is the pulse length, R is the range to the volume, Φ_{az} is the antenna's azimuthal beamwidth, and Θ_{el} is its elevation beamwidth. Of course, some of these factors are a function of time indicating what portion of the volume scatterers are being illuminated by the incident pulse waveform as it passes through the scattering medium. Equation (3) is actually an approximation in that one should integrate over the volume bounded by the antenna gain pattern weighting and the pulse width extent. The important point is that incoherent power waveform data from a pulsed radar can be converted into an effective "scattering cross section per unit illuminated volume". It should be noted that, within the resolution limits imposed by the radar pulse width and antenna beamwidth, the σ_v extracted from the data may be a function of the slant path distance (R) into the medium.

The next step in the process is to compare these measured data with our models and it is here that things become difficult. *First, as noted above there are no tractable "first-principles" models for propagation and scattering by a foliated environment under conditions of strong interaction (multiple scattering).* Secondly, those models that claim to be "more" applicable to such an environment usually are deeply imbedded with involved and tedious computations whose physical meaning is marginal at best. This quandary means that

a decision must be made as to how to best proceed, i.e., an *approach rationale* must be developed.

The approach rationale followed in developing the model presented in this report is as follows. First, it is well known that the end users of such models are extremely skeptical of any model that does not contain some measurements in its development. That is, they are concerned that the model be designed so that it is capable of at least reproducing known measurements. Consequently, we felt it essential to involve measured data in our model. The second element of this model is based upon the realization that it is possible to develop a somewhat general model for media that is not too strongly interacting and this model may be "matched" to data to determine the actual parameters that are embedded in the model and, perhaps, to extend it beyond its known range of validity. In short, the model parameters can be determined by matching actual measured data to the scattering results predicted by the model. It should be noted that such an approach avoids long and questionable computations based on one's *estimate* of what actually causes the scattering and how it does this. The reason for avoiding such computations is very simple – there is no way to estimate how applicable they will be since the accuracy of the overall model is unknown. By matching the model to data, we are in effect extending the model's accuracy through the use of "effective parameters" that are "calibrated" by the data. In summary then, our approach has been to do the best we can to develop a model that is accurate but not overly (computationally) detailed, match it to measured foliage scattering data to generate the model parameters ("effective parameters"), and then investigate the accuracy of extending the model to other situations using the existing "effective parameters".

The remainder of this report details efforts to develop the "best" model that we can for the foliage and its interaction with the terrain using the above rationale. We emphasize that while it may not be esthetically pleasing to have to resort to measurements to truly complete the model, this guarantees that the *model parameters* derived from the data will be valid and, in fact, may compensate for certain deficiencies in the model. Given the end-goal of predicting foliage scattering and penetration and trying to come up with new methods/techniques to penetrate foliage, such an approach as this may be the most appropriate!

1.2 The Major Contributors to the Return Waveform

Ideally, in estimating the returned signal from foliage covered terrain, a scattering model will include self and mutual interactions among the constituent components. In the following sections, a brief description of each significant interaction will be presented. The presentation in these sections will follow the integral equation approach.

We begin by considering the incident field, \bar{E}^{inc} , that exists in free space in the absence of the foliage and the surface, see Figure 1. With introduction of a scatterer, i.e. foliage, the total field is found to be a superposition of the incident field \bar{E}^{inc} and the field scattered by the scatterer, \bar{E}^s .

$$\bar{E}^{total} = \bar{E}^{inc} + \bar{E}^s$$

Consequently, our first task will be the construction of the scattered field produced for the i^{th} scatterer, \bar{E}_i^s , of the N objects which comprise the volume of scatterers.

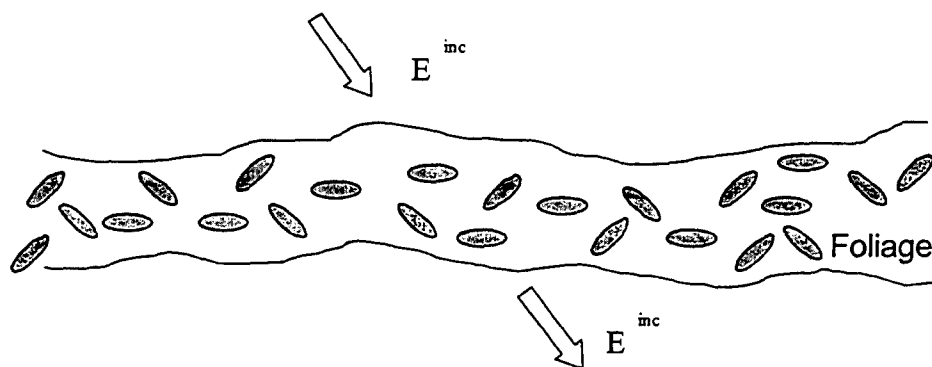


Figure 1: The Incident Field

1.2.1 Scattering from a Volume of Discrete, Closed Body Scatterers

Each component of the foliage (leaves, twigs, branches, etc.) will scatter energy from the incident field. Isolated, each scatterer's effect can be assessed using an integral equation approach that leads to a method of Moments (MOM) formulation. Consequently, the scattering solution is found in terms of a vector scattering pattern with respect to the incident field and the incident field's angle of arrival. This scattering pattern is then used to construct the scattered field due to an object. Typically, the scattering pattern is derived using the far-field approximation and assuming an incident plane wave.

Considering a volume of N scatterers without mutual interaction, the scattering patterns of the individual members can be used to construct the volume response in the direction of observation. When the location, shape or size of the individual scatterers are uncorrelated, a simple summation of the scattered power waveform from each scatterer is possible. This describes the results of the single scatter theory and first order multiple scattering, see Appendix A. First order multiple scattering plays a central role in the model proposed in this report. It is presented in a general form in Appendix A and a restricted form in Chapter 2.

If multiple scattering within the volume is expected to play an important role, interactions among the discrete scatterers must be considered. An exact solution would consider not only the scattering from each individual object, but the full interaction between them. One method of solution that accounts for full interaction between N objects is the solution of the associated N -coupled integral equations. Using the equivalence principle, the scatterers may be replaced by equivalent currents that radiate in free space. In addition to the requirement for more computing power than is commonly available, the exact solution for the N -coupled integral equations for propagation through the foliage would require an abundance of detailed data and a number of realizations to create acceptable averages. Consequently, some approximations must be made.

The reduction of the problem for backscatter and propagation through the random foliage can be achieved in several ways, depending on the level of interactions to be included. For propagation of the mean field, approximations in the literature include, but are not limited to the following

- Single scattering theory (see Appendix A)
- First order multiple scattering theory (see Appendix A)
- The Foldy-Lax-Twersky Integral Equation

Higher order moments of the field can also be handled by forming the proper moments in the first two cases. These higher order moments are necessary in order to account for the propagation of pulses. Twersky, among others, has developed integral equations that describe the higher order moments which include some level of multiple scattering [Ishimaru, 1997]; various approximate solutions exist for these equations. In addition, there are also hybrid techniques, such as the Distorted Wave Born Approximation (DWBA) [Lang, 1981]. Lang used the Foldy-Lax-Twersky Integral Equation in order to establish the mean field; he then used the single scattering theory for particles immersed in an equivalent media derived from the mean field to find the second moment. Our approach is similar to this DWBA approach.

Whether single scatter theory or multiple scatter theory is used, we will construct a composite scattered field, \bar{E}_f^s , due to the volume of scatterers, see Figure 2. In the integral equation formulation, the scattered field results from an induced current, J_{sn} , on each of the N scatterers, see Figure 2.

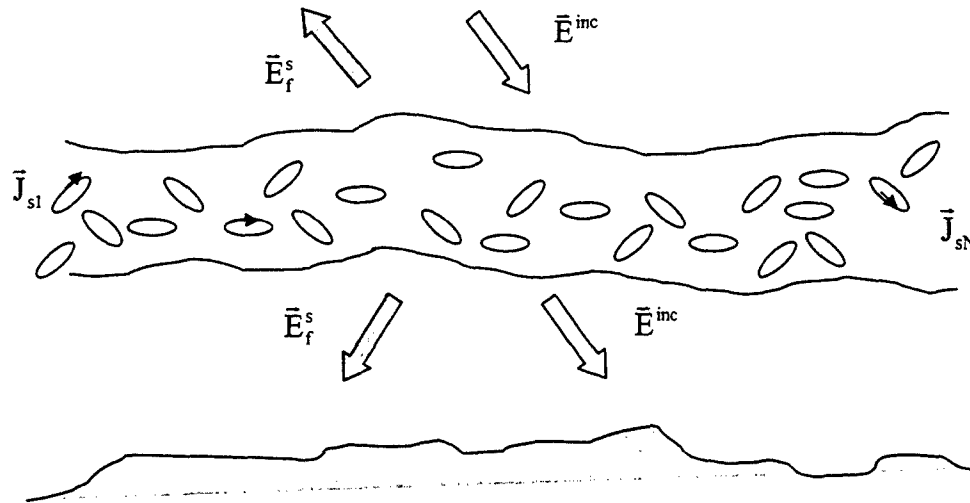


Figure 2: The total incident field with respect to the surface

Initially, we present a derivation of the scattered field from the volume using a reduced form of the radiative transfer approach that results in a form of the first order multiple scattering

result; see Chapter 4 and Appendix A. The limitations of this result are discussed at the end of Appendix A in the context of the first order multiple scattering results.

1.2.2 Scattering from a Rough Surface

To model the multiple scattering that takes place along the surface, there are several techniques available. Numerical implementations typically use the integral equation formulation. Given a field incident on a statistically rough terrain, the integral equation technique, typically numerically implemented with the Method of Moments (MOM), can yield exact results for a given realization. Average results for a collection of realizations are found using Monte Carlo methods. A solution method for the MOM formulation that is of interest in this report is the Method of Ordered Multiple Interactions (MOMI). It will be explored in Chapter 4 and is used to verify some assumptions in the model developed in this report. Analytical results, including Kirchhoff and perturbation approximations, may be useful in an analytically reduced integral equation formulation discussed in Chapter 4.

A time dependent analytical approach for the calculation of the incoherent power waveform from an extended rough surface that is consistent with the single scatter approach is the Impulse Response Method. This method is derived under the assumption that there exist a continuum of scattering facets on the surface that reflect a radar power waveform [Brown, 1977]. Under certain assumptions, the return *power* from each properly oriented surface facet enters into a summation. The number of these properly oriented facets per unit area of the surface defines a cross section per unit area. Chapter 2 presents a brief discussion of the impulse response method for calculating the scattering from terrain in free space, i.e. no foliage cover.

1.2.3 Interaction between the Foliage and the Rough Surface

Regardless of the modeling method used for the terrain and the volume scattering individually, there will be an additional source of multiple interactions (or multiple scattering): the interaction between the volume and the surface. Once the field scattered from the surface, \bar{E}_f^s , due to the currents induced on the surface, \bar{J}_s , is calculated, it can act as an additional field incident upon the foliage on its path back through the foliage to the radar. See the field \bar{E}_{fs}^s in Figure 3.

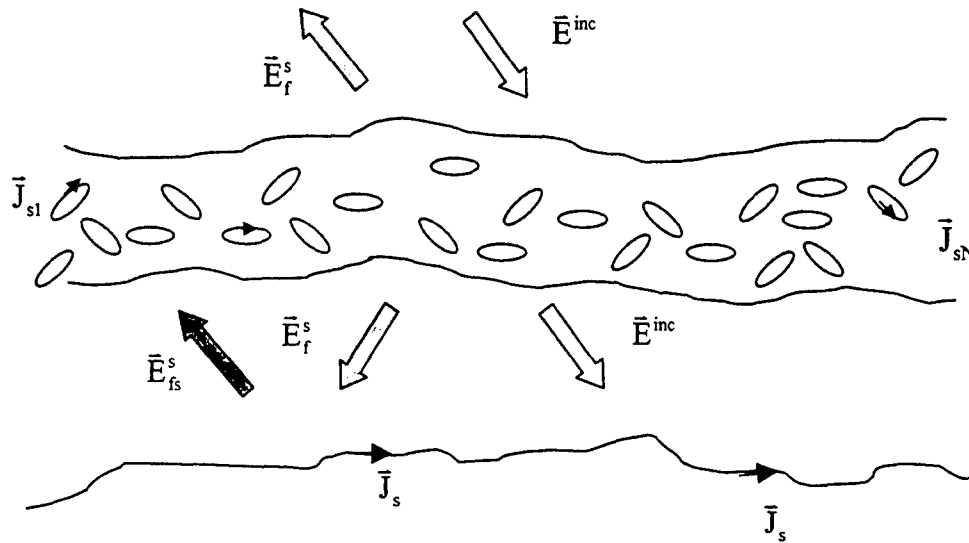


Figure 3: Surface to Foliage Interaction

This single passage (from foliage to surface, and back to foliage) does not account for the full interaction between the current induced in the foliage and the current on the surface. This single passage approximation to the interaction between the foliage and the surface represents a single interaction: the foliage-scattered field that creates the surface currents is due only to the field incident from the radar. This approximation is explored in Chapter 4 through a comparison with the exact results for a single scatterer above a rough surface. A full interaction formulation requires that the currents on the surface and on each scatterer in the foliage be coupled. Additional interaction terms would include corrections to the foliage currents due to the surface scattered field that, in turn, will produce corrections to the surface currents: an infinite series of these corrections will produce the full interaction results.

Alternatively, a coupled integral equation formulation relating the induced currents will also produce the full interaction result; this method for verification is explored in Chapter 4.

Assuming that the integral equation approach is followed, the solution for the passage from the surface through the foliage can be formulated using the equivalence principle. The *surface current*, \bar{J}_s , is permitted to radiate in free space and the resulting field acts as an additional incident field with respect to the foliage. Hence, the surface scattered field, E_{fs}^s , will induce a corrective current, \bar{J}_{sn}^s , on the n^{th} scatterer which must be vectorially added to the previous current. This current radiates a second field scattered from the foliage, \bar{E}_{fsf}^s , in addition to the scattered field due only to the foliage, \bar{E}_f^s . See Figure 4. This is a first approximation to the foliage-surface-foliage interaction.

A second order correction to the surface current will treat the incident field on the surface as

$$\bar{E}^{\text{inc on surface}} = \bar{E}^{\text{inc}} + \bar{E}_f^s + \bar{E}_{fsf}^s$$

Consequently, a new surface current \bar{J}_s is found. This current will produce a new value for the surface scattered field, \bar{E}_{fs}^s , and a new value for the field incident to the foliage from the surface. Continuing this process of iteration will produce the full interaction result.

Alternatively, like the first passage through the vegetation, this second field scattered from the foliage, \bar{E}_{fsf}^s , can be found using the single scatter approximation. This result may also be iterated, correcting the surface currents producing scattered fields. However, this result will suffer the limitations of the single scatter theory as discussed in Appendix A.

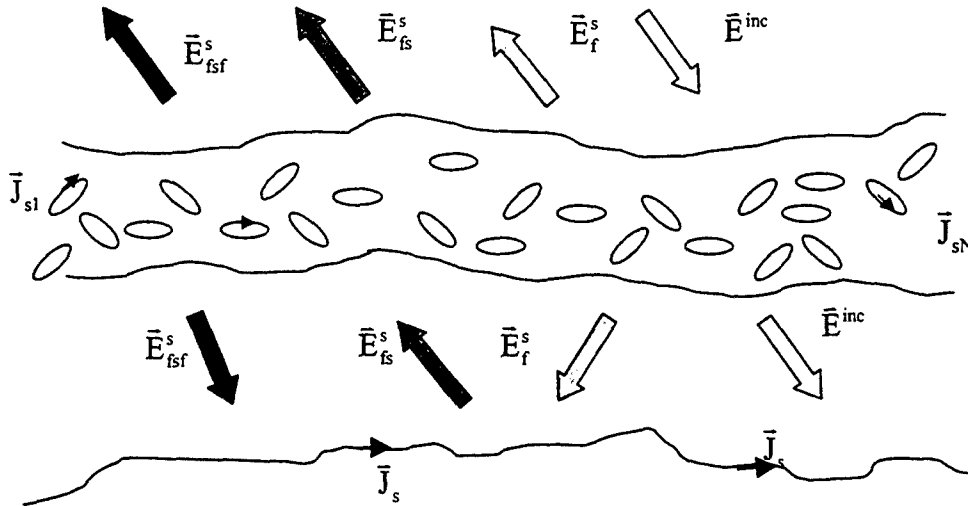


Figure 4: the second order approximate scattered field from the foliage and surface combination

1.3 Goals of this Research

The goals of this research are to produce a numerically efficient code which can incorporate measured data for calibration and accurately reproduce the general trends of an average returned waveform from terrain and foliage with similar statistics and constituents as the calibration data. Numerical efficiency is best served through the use of the impulse response approach, which casts the returned waveform into a series of convolutions and uses empirically derived parameters. Through its relation to first order multiple scattering theory, this model was found to incorporate some limiting assumptions. These assumptions are discussed in Appendix A. In order to test these assumptions, the generalized form of the radiative transfer result, first order multiple scattering model has been expanded to simulate a single scatterer over a rough surface. Some of these assumptions are quantified to a certain extent in the later sections of Chapter 4 by comparison with the “exact” numerical results. Although the simplest model, the radiative transfer result, described in Chapter 3, may not be totally adequate, at least some aspects of the convolutional formulation may be validated. In addition, the convolutional form has been retained through the use of the more general first order multiple scattering theory found in Chapter 4 and Appendix A. This development represents the major thrust of the work remaining to be done in order to verify the fully convolutional result.

In addition to verification via the first order multiple scattering, alternate formulations that incorporate more multiple scattering elements are discussed in the later sections of Chapter 4, including a reduced integral equation result. Finally, it is postulated that the results generated by a first order multiple scattering result, using Foldy-Lax-Twersky integral equation for the mean field to find the effective media, will adequately approximate the results of Lang [1981]. Consequently, a comparison with Lang's results from the Distorted Wave Born Approximation (DWBA) will be necessary. This effort is important to better understand the limitations of the model and for model verification.

2 Estimating the Isolated Surface Return Power

2.1 Integral Equation Formulation of Rough Surface Scattering and the Method of Ordered Multiple Interactions

The integral equation governing both the TE and TM polarizations in the 2-D scalar problem has been derived in many sources including [Ishimaru, 1994], by many different techniques, such as equivalence and the use of Green's Identities. Green's second identity is given by

$$f(\vec{r}) = f^i(\vec{r}) + \int_{S+S_\infty} \left\{ f(\vec{r}') \frac{\partial G(\vec{r}, \vec{r}')}{\partial n'} - G(\vec{r}, \vec{r}') \frac{\partial f(\vec{r}')}{\partial n'} \right\} ds', \quad \vec{r} \in V \quad (1)$$

In (1), V represents a certain volume in space surrounded by the closed surface S and S_∞ as shown in Figure 5.

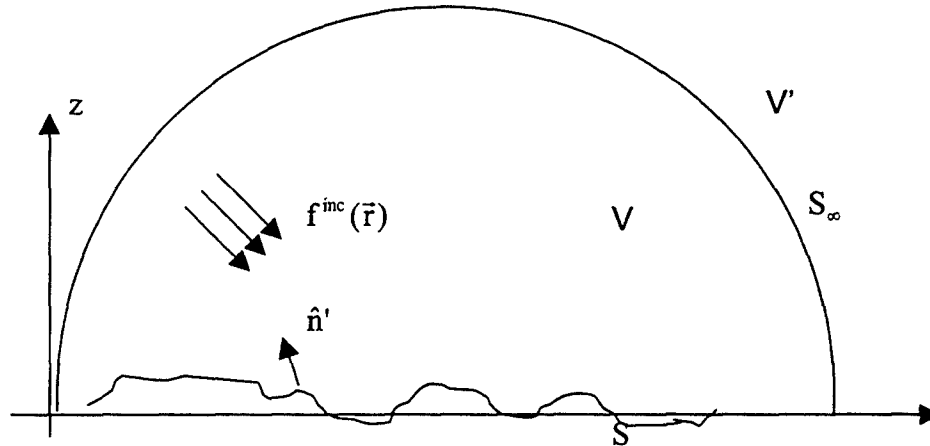


Figure 5: Problem Geometry for the Derivation of Boundary Integral Equations

Referring to Ishimaru [1994], an intermediate result derived by these methods is our starting point; we start with the following integral equation relating the total scalar field, $f(\vec{r})$, at the observation point, \vec{r} , to the incident field, $f^i(\vec{r})$:

$$f(\vec{r}) = 2f^i(\vec{r}) + \int_C \left\{ f(\vec{r}') \frac{\partial G(\vec{r}, \vec{r}')}{\partial n'} - G(\vec{r}, \vec{r}') \frac{\partial f(\vec{r}')}{\partial n'} \right\} dl', \quad \vec{r} \in C \quad (2)$$

where the contour integration is taken over a boundary enclosing the source and observation points consists of a hemisphere at infinity and a contour along the rough surface; see Figure 5.

The Green's function, $G(\bar{r}, \bar{r}')$, and its normal derivative are chosen such that their contribution is zero at infinity; hence, only the integral over the surface remains. This integration over the surface is reduced in its support by limiting the illuminated region to only a portion of the surface by use of a tapered beam. A more detailed description of this process can be found in many sources including Kapp and Brown [1996].

For 1-D surfaces, the contour length may be projected onto the x-axis. This reduces the integration to an integral over one Cartesian coordinate. Hence, employing the transformation

$$dl' = \sqrt{1 + \zeta_x^2(x')} dx' \quad (2)$$

we can construct the governing integral equations in rough surface scattering. First, the Electric Field Integral equation (EFIE), can be derived directly from (1) by enforcing the following boundary condition on the perfectly conducting surface: $f(\bar{r}) = E_y(\bar{r}) = 0$. This results in the following first kind integral equation applicable for TE polarization.

$$E_y^i(\bar{r}) = \int_{-\infty}^{\infty} \frac{\partial E_y(\bar{r}')}{\partial n'} G(\bar{r}, \bar{r}') \sqrt{1 + \zeta_x^2(x')} dx' \quad (3)$$

In deriving the Magnetic Field Integral Equation (MFIE), the following boundary condition is enforced: the normal derivative of the tangential magnetic field, $\partial f(\bar{r}') / \partial n' = \partial H_y(\bar{r}') / \partial n'$, is zero on the surface. This results in the following second kind integral equation applicable for TM polarization.

$$H_y(\bar{r}) = 2H_y^i(\bar{r}) + 2 \int_{-\infty}^{\infty} H_y(\bar{r}') \frac{\partial G(\bar{r}, \bar{r}')}{\partial n'} \sqrt{1 + \zeta_x^2(x')} dx' \quad (4)$$

In order to express the equation governing the TE polarization in the form similar to the MFIE, we take the normal derivative of both sides of (3) along the unit normal \hat{n} defined at the observation point \bar{r} . Then, we eliminate the weak singularity of the normal

derivative of the Green's function through a limiting process [Ishimaru, 1994]. This yields the following second kind integral equation for the TE polarization

$$\frac{\partial E_y(\vec{r})}{\partial n} = 2 \frac{\partial E_y^i(\vec{r})}{\partial n} - 2 \int_{-\infty}^{\infty} \frac{\partial E_y(\vec{r})}{\partial n'} \frac{\partial G(\vec{r}, \vec{r}')}{\partial n} \sqrt{1 + \zeta_x^2(x')} dx' \quad (5)$$

The discretized versions of the above equations, when properly sampled, yield large, full matrices that scale as the number of unknowns squared. Scattering from a rough terrain, formulated with this integral equation approach typically was limited to small surfaces or narrow incident beams due to the matrix storage and inversion requirements of the conventional method of moments (MOM). Solving the integral equations numerically via the Method of Ordered Multiple Interactions (MOMI), however, has reduced this computation time and storage without approximation [Kapp and Brown, 1996]. Rewriting the above form of the second kind integral equations as

$$J(x) = J^i(x) + \int_D K(x, x') J(x') dx' \quad (6)$$

where $J(x)$ is the unknown surface current, $K(x, x')$ is the kernel or the propagator, and $J^i(x)$ is known, the Kirchhoff current. Although the domain of integration D is infinite by design, it can be made finite with the use of the appropriate tapered incident field. For the TE and TM cases, respectively

$$\begin{aligned} J^i(x) &= 2 \frac{\partial E_y^i(x, z)}{\partial n} \Big|_{z=\zeta(x)}, & J^i(x) &= 2 H_y^i(x, z) \Big|_{z=\zeta(x)} \\ J(x') &= \frac{\partial E(x', z')}{\partial n'} \Big|_{z'=\zeta(x')}, & J(x') &= H_y(x', z') \Big|_{z'=\zeta(x')} \\ K(x, x') &= -2 \frac{\partial G(x, x')}{\partial n} \sqrt{1 + \zeta_x^2(x')}, & K(x, x') &= 2 \frac{\partial G(x, x')}{\partial n'} \sqrt{1 + \zeta_x^2(x')} \end{aligned}$$

After discretizing the resulting second kind equation and expressing it in a vector-matrix form

$$J = J^i + PJ \quad (7)$$

In (7) both J (unknown) and J^i (known) are vectors and P is a square propagator matrix. The discretization is commonly carried out by taking values of surface height, current and propagator at the uniform grid $\{x_m\}$ of N discrete points separated by the spacing Δx . In this case, the m^{th} element of each one of the above vectors and the $(m,n)^{\text{th}}$ element of the propagator matrix are given by

$$J_m = J(x_m), \quad J_m^i = J^i(x_m) \quad \text{and} \quad P_{mm} = P(x_m, x_n) \Delta x.$$

The off diagonal elements, P_{mn} with $m \neq n$, of the discretized propagator matrix P are given by

$$P_{mn} = -2 \frac{\partial G(x_m, x_n)}{\partial n_m} \sqrt{1 + \zeta_x^2(x_n)}, \quad P_{nm} = 2 \frac{\partial G(x_m, x_n)}{\partial n'_n} \sqrt{1 + \zeta_x^2(x_n)}$$

where $x_m = (2m - 1)\Delta x - N \Delta x/2$, $m = 1, \dots, N$ (observation point on the surface)

$x_n = (2n - 1)\Delta x - N \Delta x/2$, $n = 1, \dots, N$ (source point on the surface)

for the TE case and the TM case, respectively. The diagonal elements (usually called “self terms”), however, require special treatment and are given by, [Toporkov et. al, 1998],

$$P_{mm} = \pm \frac{\zeta_{xx}(x_m)}{2\pi[1 + \zeta_x^2(x_m)]} \Delta x.$$

The upper sign corresponds to the TM case and the lower sign to the TE case and $\zeta_{xx}(x_m)$ is the surface curvature at the point.

Direct matrix inversion becomes prohibitively large, requiring the storage of the $N \times N$ propagator matrix, where N is the number of unknowns. Furthermore, the computation time for LU decomposition scales as $N^3/3 + N^2 - 5N/6$ [Kapp and Brown 1996]; here decomposing the original propagator matrix results in a lower triangular matrix, L and an upper triangular matrix, U . The MOMI approach to the scattering problem recasts the integral equation into a discretized form that is amenable to solution via simple forward elimination and back substitution without the enormous memory

requirements of LU decomposition. After some manipulation, the discretized MFIE can be written in the following form

$$J = [I - U]^{-1} [I - L]^{-1} J^i + [I - U]^{-1} [I - L]^{-1} LUJ \quad (8)$$

Although it appears that matrix inversion is still needed to solve (8), it can be shown that alternating forward and back substitution may solve this equation. The first term, J_B , has been called the “new Born term”. The following is a general iterative solution whose first term is J_B and the remaining terms are

$$J = \sum_{n=0}^{\infty} \left\{ [I - U]^{-1} [I - L]^{-1} LU \right\}^n [I - U]^{-1} [I - L]^{-1} J^i \quad (9)$$

The “new Born term” ($n = 0$) contains all orders of multiple scattering which are continuously forward scattered, continuously backward scattered, and those which are first forward scattered and then backward scattered. Numerical simulations have shown that the “new Born term” itself is adequate for most practical surfaces. For very rough perfectly conducting surfaces, a maximum of two MOMI iterations has typically proven to be sufficient.

2.1 The Incoherent Power via the Impulse Response Method

The use of the impulse response method has been well established in literature for the calculation of the average incoherent power returned from the ocean surface under pulse illumination. One of the advantages of this approach is numerical: the average return power can be recast into a series of convolutions. The result, consequently, is found easily and efficiently using the Fast Fourier Transform, the FFT.

The power due to an incremental area with a given backscattering cross section is derived directly from the radar equation. Subsequently, extending this power to include the effects of the entire surface will lead to an expression for the returned power [Brown, 1977]. The average power returned from an element of area, dA , with a cross-section per unit area $\sigma^0(\theta, \phi)$ is given by the standard radar equation; see Figure 6.

$$dP_R(t) = \frac{P_T(t)\lambda^2 G^2(\theta, \phi) \sigma^0(\theta, \phi)}{(4\pi)^3 R^4} dA \quad (1)$$

where R = range from the radar to the elemental area, dA

$G(\theta, \phi)$ = antenna gain at the given angles

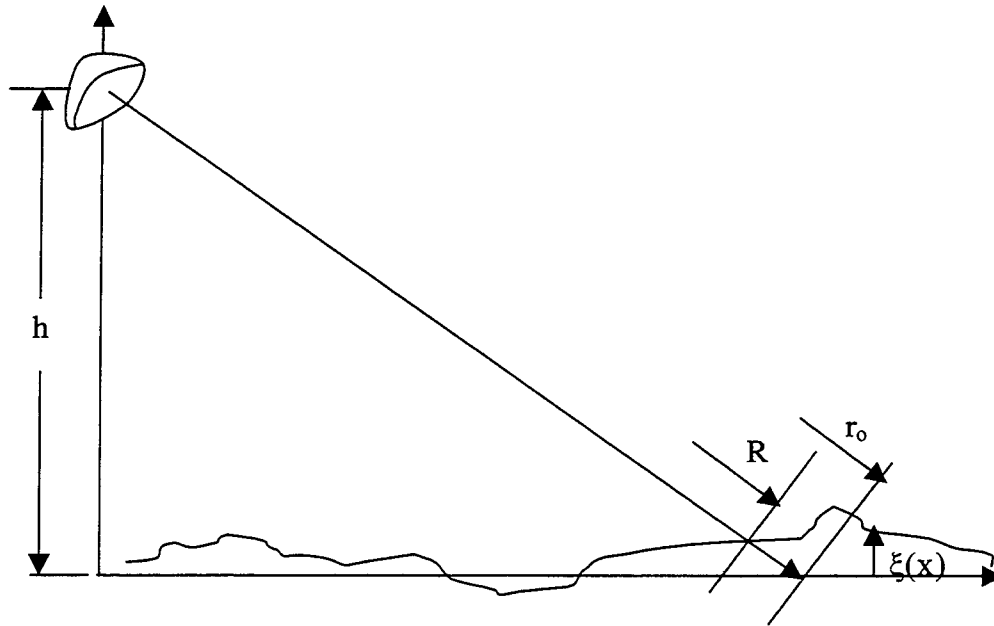


Figure 6: The Geometry for the Impulse Response Method

The average power returned from a distributed target, such as the terrain in this case, is calculated by a superposition of backscattered power from each elemental surface area, dA . A superposition of power is appropriate since the scattering surface is assumed to have a sufficiently random nature; there is no coherent return. The average backscattered power returned from the illuminated surface can be written as

$$P_R(t) = \frac{\lambda^2}{(4\pi)^3} \int_0^\infty \int_0^{2\pi} \frac{P_T \left(t - \frac{2(r_0 - \xi(x, y) \sec \theta)}{c_0} \right)}{(r_0 - \xi(x, y) \sec \theta)^4} G^2(\theta, \phi) \sigma^0(\theta, \phi) \rho \, d\phi \, d\rho \quad (2)$$

where the slant range to the terrain has been re-written: $R = r_0 - \xi(x, y) \sec \theta$. Since the integration is over the flat surface, cylindrical coordinates can be replaced with the radar coordinates ($r_0^2 = \rho^2 + h^2 \Rightarrow r_0 \, dr_0 = \rho \, d\rho$), and the range to the surface can be approximated by the mean range for the evaluation of amplitude terms. Hence, the returned power can be re-written

$$P_R(t) \cong \frac{\lambda^2}{(4\pi)^3} \int_0^\infty \int_0^{2\pi} \frac{P_T \left(t - \frac{2(r_0 - \xi(x, y) \sec \theta)}{c_0} \right)}{r_0^4} G^2(\theta, \phi) \sigma^0(\theta, \phi) r_0 \, d\phi \, dr_0 \quad (3)$$

The average power returned from the surface can then be found by evaluating the expectation with respect to the surface heights.

$$\langle P_R(t) \rangle \cong \int_{-\infty}^\infty \frac{\lambda^2}{(4\pi)^3} \int_0^{2\pi} \int_0^\infty \frac{P_T \left(t - \frac{2(r_0 - \xi(x, y) \sec \theta)}{c_0} \right)}{r_0^4} G^2(\theta, \phi) \sigma^0(\theta, \phi) r_0 \, d\phi \, dr_0 \, p_\xi(\xi) \, d\xi$$

Introducing the change of variables,

$$\tilde{\xi}(x, y) = \frac{2 \xi(x, y) \sec \theta}{c_0} \Rightarrow p_{\tilde{\xi}}(\tilde{\xi}) = \frac{c_0}{2 \sec \theta} p_\xi \left(\frac{c_0}{2 \sec \theta} \tilde{\xi} \right)$$

we express the average returned power as

$$\langle P_R(t) \rangle \cong \frac{\lambda^2}{(4\pi)^3} \int_0^{2\pi} \int_0^\infty \int_{-\infty}^\infty \frac{P_T \left(t - \frac{2r_0}{c_0} - \tilde{\xi}(x, y) \right)}{r_0^4} p_{\tilde{\xi}}(\tilde{\xi}) \, d\tilde{\xi} \, G^2(\theta, \phi) \sigma^0(\theta, \phi) r_0 \, d\phi \, dr_0$$

Recognizing the convolutional form in the random variable, $\tilde{\xi}$, we re-write the power received as

$$\langle P_R(t) \rangle \cong \frac{\lambda^2}{(4\pi)^3} \int_0^\infty \int_0^{2\pi} \frac{P_T\left(t - \frac{2r_0}{c_0}\right) \otimes p_{\tilde{\xi}}\left(t - \frac{2r_0}{c_0}\right)}{r_0^3} G^2(\theta, \phi) \sigma^0(\theta, \phi) d\phi dr_0 \quad (4)$$

Substituting for the constant delay term,

$$t' = \frac{2r_0}{c_0}$$

and introducing the shifting properties of the Dirac Delta Function, the power received is written as follows

$$\begin{aligned} \langle P_R(t) \rangle &\cong \int_{-\infty}^{\infty} \frac{\lambda^2}{(4\pi)^3} \int_0^\infty \int_0^{2\pi} \frac{P_T(t-t') \otimes p_{\tilde{\xi}}(t-t')}{r_0^3} G^2(\theta, \phi) \sigma^0(\theta, \phi) d\phi dr_0 \delta\left(t' - \frac{2r_0}{c_0}\right) dt' \\ &\equiv \int_{-\infty}^{\infty} \frac{\lambda^2}{(4\pi)^3} \int_0^\infty \int_0^{2\pi} \frac{P_T(t-t') \otimes p_{\tilde{\xi}}(t-t')}{r_0^3} G^2(\theta, \phi) \sigma^0(\theta, \phi) d\phi dr_0 \delta\left(t' - \frac{2r_0}{c_0}\right) dt' \end{aligned}$$

Consequently, the average scattered intensity from a rough surface can be expressed as a series of convolutions

$$\langle P_r(t) \rangle = P_T(t) \otimes p_{\tilde{\xi}}(t) \otimes P_{FS}(t) \quad (5)$$

From equation in (5), the last term represents the average backscattered power from a transmitted impulse function and has been called the “Flat Surface Impulse Response” (FSIR)

$$P_{FS}(t) = \frac{\lambda^2}{(4\pi)^3} \iint_{\text{Surface}} \frac{\delta\left(t - \frac{2r_0}{c}\right)}{r_0^4} G^2(\theta, \phi) \sigma^0(\theta, \phi) dA \quad (6)$$

where: $\delta(*)$ = a Dirac delta function which accounts for the two way propagation delay

λ = wavelength of the carrier

$G(\theta, \phi)$ = radar antenna gain

$\sigma(\theta, \phi)$ = surface scattering cross section per unit area

dA = elemental surface area, $dA = r_0 dr_0 d\phi = \rho d\rho d\phi$

r_0 = slant range from the radar to the mean surface at dA

h = radar height above surface

3 Estimating the Return Power Components

3.1 Introduction to the use of a Radiative Transfer Approach

A full wave approach to the multiple scattering problem presents many analytical and numerical challenges even in tenuous, i.e. sparse, media; consequently, the simpler ideas and the more tractable numerics of radiative transfer present an appealing alternative. However, since phase information is lost, the multiple scattering phenomena described by transfer theory are not well understood. In addition, transfer theory may only have a certain range of validity. There exist at least two different levels of modeling the environment in radiative transfer theory. The first and most abundant in the literature is a level that can become quite detailed. Typical examples of this are found in references [Ulaby, 1990] and [Karam, 1997]. The second approach treats radiative transfer as a theory that deals in bulk media and effective parameters. A typical example of this approach would include Schwering [1985]. In this section, we present the formulation of a simple radiative transfer model for predicting the return power waveform from a rough surface with a vegetated cover that is based on measured parameters.

A computationally efficient method for the determination of the scattered power density can be found in [Brown, 1977] for a rough surface and [Newkirk and Brown, 1996] for a rough surface covering a penetrable volume. This approach creates a numerically efficient method since the incoherent return can be cast as a series of convolutions. Henceforth referred to as the Impulse Response approach, this method as applied to rough surfaces has been briefly reviewed in Chapter 2. Although the Impulse Response approach was originally derived from the radar equation, it leads to a volume return waveform that can be derived from radiative transfer theory [Adams and Brown, 1998a]. This idea will be extended to the volume response of vegetation over a rough surface in the next section.

3.2 Derivation of a Volume/Surface Impulse Response Approach

The geometry for the radiative transfer approach is given in Figure 7 below. In this figure, the first two boundaries' (enclosing the canopy) height statistics are described by the same random variable, $\xi(x)$ and the third (rough terrain) boundary's height statistics are described by the random variable, $\zeta(x)$. The mean heights of the layer boundaries, d_1 and d_2 , are deterministic distances. Hence, we have implicitly assumed a zero mean surface with a layer of vegetation whose average thickness is d_1 . This vegetative layer has mean height above ground equal to a constant, d_2 .

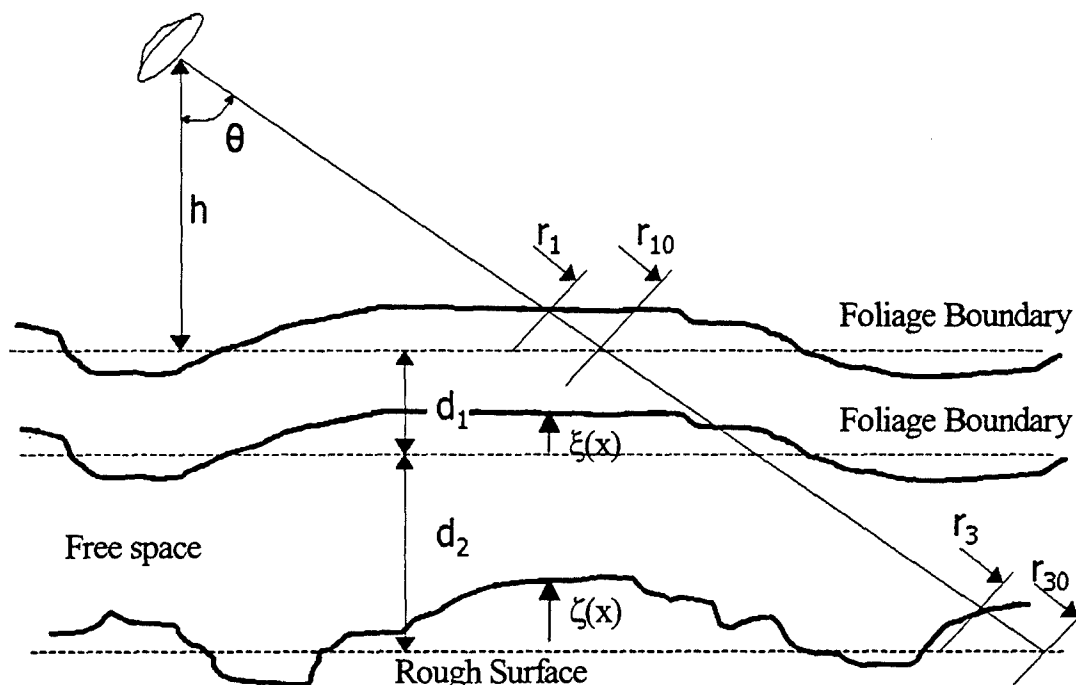


Figure 7: the geometry describing the volume and surface. Note that dotted lines indicate average levels for the associated boundary.

Beginning with a general form of the radiative transfer equation for the incoherent power density or the intensity in the medium, a simple form of the radiative transfer equation amenable to solution via convolution will be derived. The geometry for the general radiative transfer equation is given in Figure 8

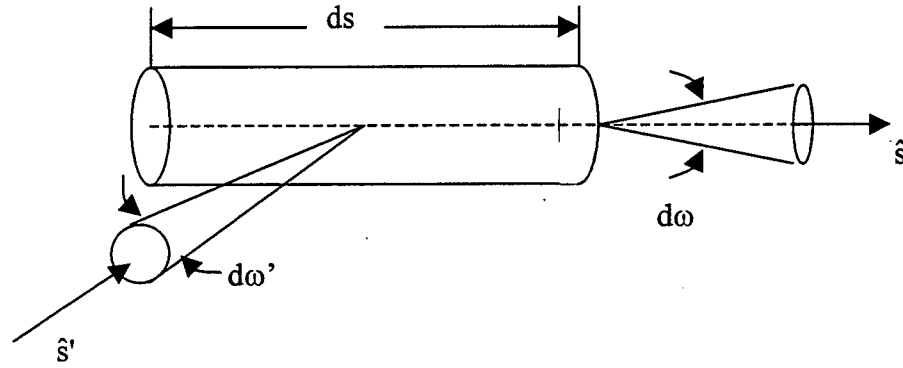


Figure 8: Scattering geometry for the intensity [Ishimaru, 1997]

Assuming that the scattering process is polarization insensitive, we will use the scalar radiative transfer equation, which relates the differential change in the power density over volume ds . This is written as (including the time dependent variation)

$$\frac{\partial I(\hat{s}; \vec{r}, t)}{\partial s} = -\rho \sigma_t I(\hat{s}; \vec{r}, t) + \frac{\rho \sigma_t}{4\pi} \iint_{4\pi} p(\hat{s}, \hat{s}') I(\hat{s}'; \vec{r}, t) d\omega' + J_s(\hat{s}; \vec{r}) - \frac{1}{c_s(\vec{r})} \frac{\partial}{\partial t} I(\hat{s}; \vec{r}, t) \quad (1)$$

where

- $I(\hat{s}; \vec{r})$ is the power density in the \hat{s} direction at the position: \vec{r}
- \hat{s} is a direction of the power density
- ρ is the scatterer density
- $\sigma_t(\vec{r})$ is the scatterers total cross section which is the sum of the absorbing and scattering cross sections: $\sigma_t(\vec{r}) = \sigma_{abs}(\vec{r}) + \sigma_{sc}(\vec{r})$ and as written here, may be a function of position \vec{r} .
- $p(\hat{s}, \hat{s}')$ is the scattering function of each scatterer; (prime denotes incident direction(s)) and is related to the amplitude of the field scattering function squared.
- $J_s(\hat{s}; \vec{r})$ is the source function (emission sources)

Referring to equation (1), the change in power in the \hat{r} direction is proportional to the power incident on the differential volume element. This power is then depleted by absorption as well as scattering into other directions. On the other hand, the power, as it propagates through the differential volume, increases by an amount due to scattering into the \hat{r} direction from other directions \hat{r}' as well as energy emitted inside the differential volume:

We can now derive an impulse response representation by making the following assumption regarding the scattering function (or classically, the phase function), $p(\hat{r}, \hat{r}')$. It will be assumed that each scatterer scatters energy in *the forward and backward directions, exclusively*.

$$p(\hat{s}, \hat{s}') = \frac{2}{\sigma_t} [\sigma_f \delta(\hat{s}' - \hat{s}) + \sigma_b \delta(\hat{s}' + \hat{s})]$$

where σ_f and σ_b are the position dependent forward and backward scattering cross section of each scatterer, respectively. These may be functions of depth into the media, shown explicitly by the \bar{r} dependence, as well as the scattering angle. In addition, we will assume that there are no emission sources present; consequently, the source term, $J_s(\hat{s}; \bar{r})$, is zero. This is a good assumption for active sensing techniques [Ulaby, 1986].

With this scattering function assumed, the radiative transfer equation is recast into a greatly simplified form. Since the direction of power density propagation \hat{s} has been limited to the radial direction, \hat{r} , the equation governing the power density can be written as a first order partial differential equation in two variables: time and distance. Implicitly assuming the \bar{r} dependence in the cross section parameters, the simplified equation of transfer becomes

$$\frac{\partial I(\hat{r}; \bar{r}, t)}{\partial r} = -\rho \sigma_t I(\hat{r}; \bar{r}, t) + \rho [\sigma_f I(\hat{r}; \bar{r}, t) + \sigma_b I(-\hat{r}; \bar{r}, t)] - \frac{1}{c_s(\bar{r})} \frac{\partial I(\bar{r}, \hat{r}, t)}{\partial t}$$

In order to further simplify the equation of transfer, we split it into two parts: downwelling, that power density which propagates in the forward hemisphere and upwelling, that power density which propagates in the backward hemisphere as defined by the direction of propagation, \hat{r} .

Let us first consider the downwelling intensity. In its solution, we will assume that the upwelling power density does not act as a source for the downwelling power density or $\sigma_b(r) = 0$. At this time, we consider this event to be second order scattering that may be neglected. Next, we define an effective extinction coefficient per unit volume $\tilde{k}_e(\bar{r}) = \rho \sigma_t(\bar{r}) - \rho \sigma_f(\bar{r})$. We then assume a media that is radially distributed which results in the modified effective extinction coefficient: $\tilde{k}_e(r) = \rho \sigma_t(r) - \rho \sigma_f(r)$. Hence, implementing these assumptions, we find the greatly simplified equation

$$\frac{\partial I(\hat{r}; \bar{r}, t)}{\partial r} = -\tilde{k}_e(r) I(\hat{r}; \bar{r}, t) - \frac{1}{c_s(\bar{r})} \frac{\partial I(\hat{r}; \bar{r}, t)}{\partial t} \quad (2)$$

Since it has been assumed that the upwelling power density does not contribute to the downwelling, there is no coupling of power from the upwelling into the downwelling. Consequently, given an initial power density at the upper foliage boundary with free space, $I_0(t - t')$ where t' is a range dependent delay, the solution for the downwelling power density is found in closed form. The method of characteristics yields a time-shifted argument for the power density, while the distance dependence can be found by simple integration.

$$I(\hat{r}; r, \theta, \phi, t) = I_0 \left(t - \frac{r_1}{c_0} - \int_{r_1}^r \frac{d\mu}{c_s(\mu)} \right) \exp \left\{ - \int_{r_1}^r \tilde{k}_e(\mu) d\mu \right\} \quad (3)$$

where $I_0(t - t')$ is the time-delayed incident power envelope; the time delay is a function of the range in free space from the antenna to the canopy (r_1) and the range into the medium which may have a range dependent group velocity, $c_s(r)$. Note that the downwelling power density is directed in the \hat{r} direction or along a radial path from the source antenna.

The differential equation governing the upwelling power density has a similar form; however, the downwelling power density acts as a source for the upwelling. In addition, the upwelling power density is directed in the $-\hat{r}$ direction or along a reverse radial path toward the source antenna. Consequently, the governing differential equation is the same with the exception of the coupling term relating the upwelling and the downwelling

intensities. The differential equation governing the upwelling power density is expressed below.

$$\frac{\partial I(-\hat{r}; \bar{r}, t)}{\partial r} = -\tilde{k}_e(r) I(-\hat{r}; \bar{r}, t) - \frac{1}{c_s(\bar{r})} \frac{\partial I(-\hat{r}, \hat{s}, t)}{\partial t} + \sigma_b(r, \theta, \phi) I(\hat{r}; r, t) \quad (4)$$

Subsequently, substituting the solution for the downwelling power density into equation (4), the following differential equation is created governing the upwelling power density

$$\begin{aligned} \frac{\partial I(-\hat{r}; \bar{r}, t)}{\partial r} = & -\tilde{k}_e(r) I(-\hat{r}; \bar{r}, t) - \frac{1}{c_s(\bar{r})} \frac{\partial I(-\hat{r}, \hat{s}, t)}{\partial t} \\ & + \sigma_b(r, \theta, \phi) I_o \left(t - \frac{r_1}{c_0} - \int_{r_1}^r \frac{d\mu}{c_s(\mu)} \right) \exp \left\{ - \int_{r_1}^r \tilde{k}_e(\mu) d\mu \right\} \end{aligned} \quad (5)$$

The attenuated downwelling power density that passes through the foliage layer and is subsequently scattered by the underlying surface acts as a source for the upwelling power density at the foliage layer's lower boundary. In addition, the downwelling power density continuously contributes to the upwelling power density due to the coupling term. Note that this source was absent in the differential equation for the downwelling. Consequently, in formulating the solution, the upwelling power density has two independent sources: the power waveform backscattered by the surface and the backscattered downwelling power density from within the volume. Finally, the upwelling power density is evaluated at the top of the canopy ($r = r_1$). Again, invoking the method of characteristics as a solution method for the time dependence, the resulting solution of equation (6) has two independent terms

$$\begin{aligned} I(-\hat{r}; r=r_1, \theta, \phi, t) = & \sigma_s(\theta, \phi) I_o \left(t - \frac{r_1}{c_0} - 2 \int_{r_1}^{r_2} \frac{d\mu}{c(\mu)} \right) \exp \left\{ - 2 \int_{r_1}^{r_2} \tilde{k}_e(\mu) d\mu \right\} \\ & + \int_{r_1}^{r_2} \sigma_b(\alpha) I_o \left(t - \frac{r_1}{c_0} - 2 \int_{r_1}^{\alpha} \frac{d\mu}{c(\mu)} \right) \exp \left\{ - 2 \int_{r_1}^{\alpha} \tilde{k}_e(\mu) d\mu \right\} d\alpha \end{aligned} \quad (6)$$

where

$$\sigma_s(\theta, \phi) = \sigma_s^0(\theta, \phi) dA, \text{ the surface's scattering cross section}$$

$$\begin{aligned}
r_1 &= r_{10} + \xi(x) \sec \theta \\
r_2 &= r_{10} + d_1 \sec \theta + \xi(x) \sec \theta \\
r_3 &= r_{10} + (d_1 + d_2) \sec \theta + \zeta(x) \sec \theta
\end{aligned}$$

This expression shows a simple superposition of two terms; the first term is the rough surface return propagated back up through the foliage and the second term represents the foliage scattered return. In order to construct the average return power in the impulse response format, these two responses are averaged and manipulated to yield an impulse response term in each case. However, an additional assumption is necessary for a fully convolutional result similar to that given in the literature for a rough surface alone: the random variables, $\zeta(x)$ and $\xi(x)$, describing the canopy and the rough surface, respectively, must be assumed to be independent.

3.3 Incoherent Scattered Power: the Volume (Foliage) Return

In the formulation of the scattering from a rough surface with a vegetative cover, we have assumed that scattering occurs exclusively in the forward and backward directions; this implied that the power density in radial direction \hat{r} does not interact with the power density in any other radial direction. This in turn has led to a closed form result for the downwelling intensity and consequently, an uncoupled relatively simple equation for the upwelling power density, equation (6) in the previous section. The two terms of the solution in (6) can be simplified independently. Each represents a different scattering phenomena, surface and volume scattering. In this section we examine the foliage or volume return.

We begin with the second term of equation (6) for the upwelling power density, the volume response. After substitution for the slant range variables (r_1, r_2, \dots) with the associated distance and random variables as a function of antenna pointing angle, θ ,

$$\begin{aligned} r_1 &= r_{10} + \xi(x) \sec \theta \\ r_2 &= r_{10} + d_1 \sec \theta + \xi(x) \sec \theta \\ r_3 &= r_{10} + (d_1 + d_2) \sec \theta + \zeta(x) \sec \theta \end{aligned}$$

the power density is found to be approximated by the following

$$\begin{aligned} I(-\hat{r}; r, \theta, \phi, t) &= \int_{r_{10} + \xi(x) \sec \theta}^{r_{10} + \xi(x) \sec \theta + d_1 \sec \theta} \sigma_b(\alpha) \exp \left\{ -2 \int_{r_{10} + \xi(x) \sec \theta}^{\alpha} \tilde{k}_e(\mu) d\mu \right\} \\ &\cdot I_0 \left(t - \frac{(r_{10} + \xi(x) \sec \theta)}{c_0} - 2 \int_{r_{10} + \xi(x) \sec \theta}^{\alpha} \frac{d\mu}{c(\mu)} \right) d\alpha \end{aligned} \quad (1)$$

In general, following a slightly modified version of the method of Adams and Brown [1998a], and assuming a layered media with parallel boundaries, the average power density can be expressed as

$$\begin{aligned} \langle I(-\hat{r}; r, \theta, \phi, t) \rangle &= \int_{-\infty}^{\infty} \int_{r_{10} + \xi(x) \sec \theta}^{r_{10} + \xi(x) \sec \theta + d_1 \sec \theta} \sigma_b(\alpha) \exp \left\{ -2 \int_{r_{10} + \xi(x) \sec \theta}^{\alpha} \tilde{k}_e(\mu) d\mu \right\} \\ &\cdot I_0 \left(t - \frac{(r_{10} + \xi(x) \sec \theta)}{c_0} - 2 \int_{r_{10} + \xi(x) \sec \theta}^{\alpha} \frac{d\mu}{c(\mu)} \right) d\alpha p_{\xi}(\xi) d\xi \end{aligned} \quad (2)$$

In order to create a convolutional form, the integration limits must be extended to infinity. The upper limit may be extended to infinity by *assuming that the extinction coefficient becomes very large once the range extends beyond the lower foliage boundary*; this will effectively eliminate the volume return after the lower foliage boundary is surpassed. The lower limit of integration, on the other hand, can be extended by the use of the unit step function, $u(r - r_1)$. Consequently, the average power density can be rewritten in terms of integrals with infinite limits. Under the change of variables, $\mu' = \mu - [r_{10} + \xi(x) \sec \theta]$, the expression for the upwelling power density becomes

$$\begin{aligned} \langle I(-\hat{r}; r, \theta, \phi, t) \rangle = & \int_{-\infty}^{\infty} \int_{-\infty}^{\infty} \sigma_b(\alpha) I_o \left(t - \frac{(r_{10} + \xi(x) \sec \theta)}{c_0} - 2 \int_0^{\alpha - [r_{10} + \xi(x) \sec \theta]} \frac{d\mu'}{c(\mu')} \right) \\ & \cdot \exp \left\{ -2 \int_0^{\alpha - [r_{10} + \xi(x) \sec \theta]} \tilde{k}_e(\mu') d\mu' \right\} u(\alpha - [r_{10} + \xi(x) \sec \theta]) d\alpha p_{\xi}(\xi) d\xi \end{aligned} \quad (3)$$

Assuming that there is no volume return from the atmosphere between the antenna and the foliage crown, the backscattering cross section, which is a function of distance, can also be shifted by the slant range. Defining two new functions

$$g(\gamma) = 2 \int_0^{\gamma} \frac{d\mu'}{c(\mu')} \quad (4)$$

$$E(\gamma) = \sigma_b(\gamma) \exp \left\{ -2 \int_0^{\gamma} \tilde{k}_e(\mu') d\mu' \right\} u(\gamma) \quad (5)$$

the average upwelling power density at the upper foliage layer can be rewritten

$$\langle I(-\hat{r}; r, \theta, \phi, t) \rangle = \int_{-\infty}^{\infty} \int_{-\infty}^{\infty} I_o \left(t - \frac{r_1}{c_0} - g[\alpha - r_1] \right) E(\alpha - r_1) d\alpha p_{\xi}(\xi) d\xi \quad (6)$$

where it has been previously defined that $r_1 = (r_{10} + \xi(x) \sec \theta)$. Following the method of Adams and Brown, [1998a], the following definitions are constructed which transform distance into time

$$t' = g[\alpha - r_1] \Rightarrow \alpha - r_1 = g^{-1}(t')$$

$$dt' = g'[\alpha - r_1]d\alpha = g'(g^{-1}(t'))d\alpha$$

Substituting these expressions into the average upwelling power density of equation (6), the average upwelling power density is reconstructed in the following form

$$\begin{aligned} \langle I(-\hat{r}; r, \theta, \phi, t) \rangle &= \int_{-\infty}^{\infty} \int_{-\infty}^{\infty} I_o \left(t - \frac{r_1}{c_0} - t' \right) \frac{E(g^{-1}(t'))}{g'(g^{-1}(t'))} dt' p_{\xi}(\xi) d\xi \\ &= \int_{-\infty}^{\infty} \int_{-\infty}^{\infty} I_o \left(t - \frac{r_1}{c_0} - t' \right) \tilde{E}(t') dt' p_{\xi}(\xi) d\xi \end{aligned} \quad (7)$$

where a new function has been defined:

$$\tilde{E}(t) = \frac{E(g^{-1}(t))}{g'(g^{-1}(t))}$$

Noting that expression (7) contains a convolution in the variable z , we perform the z integration, leaving the result in the form of a convolution (with convolution represented by the symbol: \otimes) shown in brackets below

$$\langle I(-\hat{r}; r=r_1, \theta, \phi, t) \rangle = \int_{-\infty}^{\infty} \left\{ I_o \left(t - \frac{r_1}{c_0} \right) \otimes \tilde{E} \left(t - \frac{r_1}{c_0} \right) \right\} p_{\xi}(\xi) d\xi$$

Substituting for the slant range in terms of the distance to the mean height and the random variable representing the distribution about the mean, i.e. $r_1 = (r_{10} + \xi(x) \sec \theta)$

$$\langle I(-\hat{r}; r=r_1, \theta, \phi, t) \rangle = \int_{-\infty}^{\infty} \left\{ I_o \left(t - \frac{(r_{10} + \xi(x) \sec \theta)}{c_0} \right) \otimes \tilde{E} \left(t - \frac{(r_{10} + \xi(x) \sec \theta)}{c_0} \right) \right\} p_{\xi}(\xi) d\xi$$

First, we substitute for the constant delay term: we let

$$t_0 = \frac{r_{10}}{c_0}$$

Then we make a change of variables with respect to the random variable representing the crown height statistics; we form a new random variable and its associated probability density function

$$\tilde{\xi}(x) = \frac{\xi(x) \sec \theta}{c_0},$$

$$p_{\tilde{\xi}}(t) = \frac{c_0}{\sec \theta} p_{\xi}\left(\frac{c_0 t}{\sec \theta}\right)$$

Consequently, the average upwelling power density becomes

$$\langle I(-\hat{r}; r=r_1, \theta, \phi, t) \rangle = \frac{c_0}{\sec \theta} \int_{-\infty}^{\infty} \{ I_o(t - t_0 - \tilde{\xi}) \otimes \tilde{E}(t - t_0 - \tilde{\xi}) \} p_{\tilde{\xi}}(\tilde{\xi}) d\tilde{\xi}$$

Again, the average upwelling power density is re-expressed in the following convolutional form with respect to the modified surface height random variable

$$\langle I(-\hat{r}; r=r_1, \theta, \phi, t) \rangle = \frac{c_0}{\sec \theta} I_o(t - t_0) \otimes \tilde{E}(t - t_0) \otimes p_{\tilde{\xi}}(t - t_0) \quad (8)$$

Finally, in order to find the total power returning toward the radar, we integrate the power density over a surface. In this case, a convenient surface is the top of the canopy. Allowing for full penetration of the incident power density (i.e. no reflection from the boundary separating free space from the foliage), we substitute for the incident power density at the canopy (expressed in the $\{ \}$ brackets below) weighted by the antenna gain $G(\theta, \phi)$ in the direction (θ, ϕ) ,

$$I_o(\theta, \phi, t - t_0) = \frac{G(\theta, \phi)}{4\pi r_{10}^2} P_T(t - t_0)$$

Furthermore, we must assume a narrow beamwidth such that $\sec \theta \approx \sec \theta_0$ (boresight direction: θ_0). This is required since the integral to be performed over the radial coordinate implicitly contains θ dependence; otherwise, a convolutional form can not be obtained. Allowing for the additional delay due to the transmission back to the antenna (an additional t_0) from the canopy and the receiving antenna's effective aperture, the following result is obtained

$$\begin{aligned} \langle P_R(t) \rangle = & \int_0^\infty \int_0^{2\pi} \frac{c_0}{\sec \theta_0} \left\{ \frac{G(\theta, \phi)}{4\pi r_{10}^2} P_T(t - 2t_0) \right\} \otimes \tilde{E}(t - 2t_0) \otimes p_{\tilde{\xi}}(t - 2t_0) \\ & \cdot \frac{\lambda^2 G(\theta, \phi)}{(4\pi)^2 r_{10}^2} r_{10} d\phi dr_{10} \end{aligned}$$

substituting the original expression for t_0 , we find

$$\begin{aligned} \langle P_R(t) \rangle = & \frac{c_0}{\sec \theta_0} \int_0^\infty \int_0^{2\pi} \left\{ \frac{G(\theta, \phi)}{4\pi r_{10}^2} P_T\left(t - \frac{2r_{10}}{c_0}\right) \right\} \otimes \tilde{E}\left(t - \frac{2r_{10}}{c_0}\right) \otimes p_{\tilde{\xi}}\left(t - \frac{2r_{10}}{c_0}\right) \frac{\lambda^2 G(\theta, \phi)}{(4\pi)^2 r_{10}^2} r_{10} d\phi dr_{10} \\ = & \frac{\lambda^2}{(4\pi)^3} \frac{c_0}{\sec \theta_0} \int_0^\infty \int_0^{2\pi} \left\{ \frac{G^2(\theta, \phi)}{r_{10}^3} P_T\left(t - \frac{2r_{10}}{c_0}\right) \right\} \otimes \tilde{E}\left(t - \frac{2r_{10}}{c_0}\right) \otimes p_{\tilde{\xi}}\left(t - \frac{2r_{10}}{c_0}\right) d\phi dr_{10} \end{aligned}$$

Exploiting the shifting properties of the Dirac delta function and rearranging the resulting integrals yields

$$\begin{aligned} \langle P_R(t) \rangle = & \frac{\lambda^2}{(4\pi)^3} \frac{c_0}{\sec \theta_0} \int_{-\infty}^\infty P_T(t - t') \otimes \tilde{E}(t - t') \otimes p_{\tilde{\xi}}(t - t') \\ & \cdot \int_0^\infty \int_0^{2\pi} \frac{G^2(\theta, \phi)}{r_{10}^3} \delta\left(t' - \frac{2r_{10}}{c_0}\right) d\phi dr_{10} dt' \\ = & \int_{-\infty}^\infty \left\{ P_T(t - t') \otimes \tilde{E}(t - t') \otimes p_{\tilde{\xi}}(t - t') \right\} P_{FS'}(t') dt' \\ = & P_T(t) \otimes \tilde{E}(t) \otimes p_{\tilde{\xi}}(t) \otimes P_{FS'}(t) \end{aligned}$$

where the transmitted power waveform is given by $P_T(t)$ and the modified Flat Surface Impulse Response function (see Chapter 2) is given by

$$P_{FS'}(t) = \frac{\lambda^2}{(4\pi)^3} \frac{c_0}{\sec \theta_0} \int_0^\infty \int_0^{2\pi} \frac{G^2(\theta, \phi)}{r_{10}^3} \delta\left(t - \frac{2r_{10}}{c_0}\right) d\phi dr_{10} \quad (9)$$

the modified probability density function for the crown height statistics is given by

$$p_{\tilde{\xi}}(t) = \frac{c_0}{\sec \theta_0} P_{\xi}\left(\frac{c_0 t}{\sec \theta_0}\right) \quad (10)$$

and $\tilde{E}(t)$ is a function relating decay to depth of penetration into the foliage layer

$$\tilde{E}(t) = \frac{E(g^{-1}(t))}{g'(g^{-1}(t))} \quad (11)$$

This general solution for the volume response can be modified to yield a simpler result. Assuming that the *velocity is constant in each layer* of the medium, the solution becomes more apparent. Here, we assume that medium 1 contains the leaves and branches (group velocity is c_{v1}) and medium 2 is the trunk region (group velocity c_{v2}). The starting point for the upwelling power density due to the volume return (along a radial in the \hat{r} direction) is then given by

$$I(-\hat{r}; r, \theta, \phi, t) = \int_{r_{10} + \xi(x) \sec \theta_1}^{r_{10} + \xi(x) \sec \theta + d_1 \sec \theta} \sigma_b(\alpha) I_0 \left(t - \frac{(r_{10} + \xi(x) \sec \theta)}{c_0} - \frac{2[\alpha - (r_{10} + \xi(x) \sec \theta)]}{c_{v1}} \right) \\ \cdot \exp \left\{ -2 \int_{r_{10} + \xi(x) \sec \theta_1}^{\alpha} \tilde{k}_e(\mu) d\mu \right\} d\alpha$$

After following the previous procedure, the average power as a function of time, scattered from a volume with an irregular interface at the crown can be expressed in the convolutional form

$$\langle P(t) \rangle = P_T(t) \otimes P_{FS}(t) \otimes p_{\tilde{\xi}}(t) \otimes \tilde{E}(t)$$

where in this particular case,

$$t' = g(r') = \frac{2r'}{c} \Rightarrow r' = g^{-1}(t') = \frac{ct'}{2} \quad \text{and} \quad g'(r) = \frac{2}{c} = \text{constant}$$

Hence, for a group velocity in the volume given by c_v ,

$$\tilde{E}(t) = \frac{E(g^{-1}(t))}{g'(g^{-1}(t))} = \frac{E(c_v t / 2)}{2 / c_v} = \frac{c_v}{2} \sigma_b \exp \left\{ -2 \int_0^{c_v t / 2} \tilde{k}_e(\mu') d\mu' \right\} u(c_v t / 2)$$

Note that the unit step function $u(t)$ "turns on" when $t = 0$.

3.1 Incoherent Scattered Power: the Rough Surface Return

We start with the expression for the power density attenuated by the foliage in its downward passage, scattered from the surface, and then attenuated by the foliage in its upward passage; this is the first term of equation (6) in Section 3.1. Note that the geometry of Figure 3.1-1 still applies

$$I(-\hat{r}; r=r_1, \theta, \phi, t) = \sigma_s(\theta, \phi) I_0 \left(t - \frac{2r_1}{c_0} - 2 \int_{r_1}^{r_3} \frac{d\mu}{c(\mu)} \right) \exp \left\{ -2 \int_{r_1}^{r_3} \tilde{k}_e(\mu) d\mu \right\} \quad (1)$$

Substituting for the power density using the following relationship

$$I(r, \theta, \phi, t) = \frac{P_T(t) G(\theta, \phi)}{4\pi r^2} \quad (2)$$

where I is the power density (sometimes called intensity), P_T is the power waveform and the \hat{r} direction is specified by the angles θ and ϕ . The average power returned from within the illuminated region can be evaluated by integrating over a surface encompassing the illuminated area. In this case, we choose to integrate over the area at the top of the canopy ($r = r_1$). Hence, substituting the power waveform for the incident power density in equation (1) via the relationship in equation (2) and performing the ensemble average over the random variables, the total average power *at the crown* is

$$\langle P(t) \rangle = \iint_{\substack{\text{surface at} \\ r = r_{10}}} \left\langle \sigma_s(\theta, \phi) \frac{G(\theta_a, \phi_a)}{4\pi r^2} P_T \left(t - \frac{r_1}{c_0} - 2 \int_{r_1}^{r_3} \frac{d\mu}{c(\mu)} \right) \exp \left\{ -2 \int_{r_1}^{r_3} \tilde{k}_e(\mu) d\mu \right\} \right\rangle dS \quad (3)$$

where the surface scattering cross section per unit area, $\sigma_s^0(\theta, \phi)$, has been included. The angles (θ, ϕ) are spherical coordinates centered at the antenna and can be related to the variables of integration. Also in this expression, the antenna gain has a boresight angle given by (θ_0, ϕ_0) and the angles (θ_a, ϕ_a) are spherical coordinates defined with respect to this antenna boresight direction which may also be related to the variables of integration.

Although the solution procedure can proceed with a propagation speed, $c(\bar{r})$, and an effective extinction coefficient, $\tilde{k}_e(\bar{r})$ that vary with position as assumed in (3), the following results are simplified since they are based on a constant group velocity and extinction coefficient in each layer.

- Free space, the group velocity is c_0
- Layer 1, the canopy region, the group velocity is c_{v1} , the effective extinction coefficient is \tilde{k}_{e1} , $r \in (r_1, r_2)$
- Layer 2 the trunk region, the group velocity is c_{v2} , the effective extinction coefficient is \tilde{k}_{e2} , $r \in (r_2, r_3)$

Hence, the integrals with respect to the radial distance within the argument of the transmitted power may be easily performed, yielding the average power *at the radar*

$$\langle P(t) \rangle = \iint_{\substack{\text{surface at} \\ r = r_{10}}} \left\langle \sigma_s^0(\theta, \phi) \frac{\lambda^2 G^2(\theta_a, \phi_a)}{(4\pi)^3 r^4} P_T \left(t - \frac{2r_1}{c_0} - \frac{2(r_2 - r_1)}{c_{v1}} - \frac{2(r_3 - r_2)}{c_{v2}} \right) \exp \left\{ -2 \int_{r_1}^{r_3} \tilde{k}_e(\mu) d\mu \right\} \right\rangle dS$$

The final results will be cast in a convolutional form for the average returned power. After expanding the transmitted power waveform's delay time argument in terms of the random variables and constant terms,

$$\begin{aligned} r_1 &= r_{10} + \xi(x) \sec \theta \\ r_2 &= r_{10} + d_1 \sec \theta + \xi(x) \sec \theta \\ r_3 &= r_{10} + (d_1 + d_2) \sec \theta + \zeta(x) \sec \theta \end{aligned}$$

and performing the integrations with respect to the extinction coefficients, the average return power as a function of time becomes

$$\begin{aligned}
\langle P_R(t) \rangle = & \iint_{\text{Surface at } r=r_{10}} \frac{\lambda^2 G^2(\theta_a, \phi_a)}{(4\pi)^3 r^4} \sigma_s^0(\theta, \phi) \\
& \cdot \int_{-\infty}^{\infty} \int_{-\infty}^{\infty} P_T \left(t - \frac{2r_{10} \sec \theta}{c_0} - \frac{\xi(x) \sec \theta}{c_0} - \frac{2d_1 \sec \theta}{c_{v1}} - \frac{2d_2 \sec \theta}{c_{v2}} - \frac{2[\zeta(x) - \xi(x)] \sec \theta}{c_{v2}} \right) \\
& \cdot \exp \left\{ -2\tilde{k}_{e1} d_1 \sec \theta - 2\tilde{k}_{e2} (d_2 + \zeta(x) - \xi(x)) \sec \theta \right\} p_\xi(\xi) p_\zeta(\zeta) d\xi d\zeta r dr d\phi
\end{aligned} \quad (4)$$

where $p_\xi(\xi)$ and $p_\zeta(\zeta)$ are the probability density functions for the boundary heights of the foliage volume and the rough surface, respectively. Rearranging and substituting for the constant terms, equation (4) is rewritten

$$\begin{aligned}
\langle P_R(t) \rangle = & \iint_{\text{Surface at } r=r_{10}} \frac{\lambda^2 G^2(\theta_a, \phi_a)}{(4\pi)^3 r^4} \sigma_s^0(\theta, \phi) \exp \left\{ -2 \sec \theta (\tilde{k}_{e1} d_1 - \tilde{k}_{e2} d_2) \right\} \\
& \cdot \int_{-\infty}^{\infty} \int_{-\infty}^{\infty} P_T \left(t - t_0 - \frac{2\xi(x) \sec \theta}{c_a} - \frac{2\zeta(x) \sec \theta}{c_{v2}} \right) \\
& \cdot \exp \left\{ 2\tilde{k}_{e2} \xi(x) \sec \theta \right\} p_\xi(\xi) d\xi \exp \left\{ -2\tilde{k}_{e2} \zeta(x) \sec \theta \right\} p_\zeta(\zeta) d\zeta r dr d\phi
\end{aligned} \quad (5)$$

where $\tilde{k}_{e1}, \tilde{k}_{e2}$ are the effective extinction coefficients in medium 1 and 2, respectively; and

$$\begin{aligned}
t_0 &= \frac{2r_{10} \sec \theta}{c_0} - \frac{2d_1 \sec \theta}{c_{v1}} - \frac{2d_2 \sec \theta}{c_{v2}} \\
\frac{2}{c_a} &= \left(\frac{1}{c_0} - \frac{2}{c_{v2}} \right)
\end{aligned}$$

Performing a change of variables which transform distance into time

$$\begin{aligned}
t_1 &= \frac{2\zeta(x) \sec \theta}{c_{v2}} \Rightarrow d\zeta = \frac{c_{v2}}{2 \sec \theta} dt_1 \\
t_2 &= \frac{2\xi(x) \sec \theta}{c_a} \Rightarrow d\xi = \frac{c_a}{2 \sec \theta} dt_2
\end{aligned}$$

and defining some new functions,

$$\begin{aligned} f_{t1}(t_1) &= \exp\left\{-\tilde{k}_{e2} c_{v2} t_1\right\} p_{t1}(t_1) \\ f_{t2}(t_2) &= \exp\left\{\tilde{k}_{e2} c_a t_2\right\} p_{t2}(t_2) \end{aligned}$$

Noting that the probability density functions describing the boundaries must also be transformed,

$$\begin{aligned} p_{t1}(t_1) &= \frac{c_{v2}}{2 \sec \theta} p_{\zeta}\left(\frac{c_{v2} t_1}{2 \sec \theta}\right) \\ p_{t2}(t_2) &= \frac{c_a}{2 \sec \theta} p_{\xi}\left(\frac{c_a t_2}{2 \sec \theta}\right) \end{aligned}$$

we find that the average returned power can be expressed as

$$\begin{aligned} \langle P_R(t) \rangle &= \iint_{\substack{\text{Surface at} \\ r=r_{10}}} \frac{\lambda^2 G^2(\theta_a, \phi_a)}{4(4\pi)^3 r_{10}^4} \sigma_s(\theta, \phi) \exp\left\{-2 \sec \theta (\tilde{k}_{e1} d_1 - \tilde{k}_{e2} d_2)\right\} \\ &\quad \frac{c_a c_{v2}}{4 \sec \theta} \int_{-\infty}^{\infty} \int_{-\infty}^{\infty} P_T(t - t_0 - t_1 - t_2) f_{t1}(t_1) dt_1 f_{t2}(t_2) dt_2 r_{10} dr_{10} d\phi \end{aligned} \quad (6)$$

Performing the t_1 and the t_2 integrations and expressing the result in convolutional form, which is represented with the \otimes symbol we find

$$\begin{aligned} \langle P_r(t) \rangle &= \iint_{\substack{\text{Surface at} \\ r=r_{10}}} \frac{c_a c_{v2}}{4 \sec^2 \theta} \frac{\lambda^2 G^2(\theta_a, \phi_a)}{(4\pi)^3 r_{10}^4} \sigma_s^0(\theta, \phi) \cdot \exp\left\{-2 \sec \theta (\tilde{k}_{e1} d_1 + \tilde{k}_{e2} d_2)\right\} \\ &\quad \cdot [P_T(t - t_0) \otimes f_{t1}(t - t_0) \otimes f_{t2}(t - t_0)] r_{10} dr_{10} d\phi \end{aligned}$$

Integrating over the foliage upper surface, the returned power can be recast into the following convolutional form, following the methods outlined in previous section.

$$\langle P_r(t) \rangle = P_T(t) \otimes f_{t1}(t) \otimes f_{t2}(t) \otimes P_{FS'}(t) \quad (7)$$

where $f_{t1}(t)$ and $f_{t2}(t)$ are functions which depend on the probability density functions whose random variables are functions of the random variables representing the surface and canopy statistics, $\xi(x), \zeta(x)$ as well as the extinction coefficients, and the antenna boresight angle, θ . The flat surface impulse response function (FSIR), $P_{FS'}(t)$, is similar to the standard FSIR with the modifications (among others) that account for attenuation:

$$P_{FS'}(t) = \frac{\lambda^2 c_a c_{v2}}{4(4\pi)^3} \int_0^\infty \int_0^{2\pi} \frac{\delta(t - 2r'/c)}{(r')^4} \frac{G^2(\theta_a, \phi_a) \sigma_s^0(\theta, \phi)}{\sec^2 \theta} \cdot \exp\{-2 \sec \theta (\tilde{k}_{e1} d_1 + \tilde{k}_{e2} d_2)\} r' dr' d\phi \quad (8)$$

Here the antenna gain is approximated by a circularly symmetric pattern with a pointing angle given by (θ_0, ϕ_0) and the angles (θ_a, ϕ_a) are spherical coordinates defined with respect to the antenna boresight direction. Consequently, the antenna gain can be represented by

$$G(\theta_a, \phi_a) = G_0(\theta_0, \phi_0) \exp\left\{-\frac{2}{\gamma} \sin^2 \theta_a\right\} \quad (9)$$

This expression (8) for the FSIR includes additional effective parameters related to the speeds in the different media, the incidence angle, and consequently, time or range:

$$h' = \frac{c_0}{c_{v1}} d_1 + \frac{c_0}{c_{v2}} d_2 + h$$

$$(r')^2 = (h')^2 + \rho^2$$

The integral for the FSIR can be simplified using the method presented in Brown [1977]; we begin by substituting the two-way incremental ranging time for the actual time: $\tau = t - 2r'/c$. Assuming that the beam is narrow such that the surface incremental cross section is constant over the angular extent of interest and that $\sec \theta \cong \sec \theta_0$ (boresight), the FSIR is found in the following form

$$P_{FS'}(\tau) = \frac{\lambda^2 c_0 c_a c_{v2} (h')^2 G_0^2(\theta_0, \phi_0) \sigma_s^0(\theta_0, \phi_0)}{16\pi^3 (c_0 \tau + 2h')^5} \exp\left\{-\left(\frac{c_0 \tau + 2h'}{h'}\right) (\tilde{k}_{e1} d_1 + \tilde{k}_{e2} d_2)\right\} \cdot \int_0^{2\pi} \exp\left\{-\frac{4}{\gamma} \sin^2 \theta_a\right\} d\phi \quad (10)$$

Note this expression can include an asymmetrical antenna pattern [Newkirk and Brown, 1992].

Summarizing, the final form of the solution to the average power returned due only to the rough surface can be expressed in the following convolutional form,

$$\langle P_r(t) \rangle = P_T(t) \otimes f_{t1}(t_1) \otimes f_{t2}(t_2) \otimes P_{FS'}(t) \quad (11)$$

where $f_{t1}(t_1)$ and $f_{t2}(t_2)$ are functions of time which depend on random variables which are functions of the surface and canopy statistics, $\xi(x), \zeta(x)$, as well as the extinction coefficients, and the pointing angle:

$$\begin{aligned} t_1 &= \frac{2\zeta(x) \sec \theta}{c_{v2}} \Rightarrow p_{t1}(t_1) = \frac{c_{v2}}{2 \sec \theta} p_{\zeta} \left(\frac{c_{v2} t_1}{2 \sec \theta} \right) \\ t_2 &= \frac{2\xi(x) \sec \theta}{c_a} \Rightarrow p_{t2}(t_2) = \frac{c_a}{2 \sec \theta} p_{\xi} \left(\frac{c_a t_2}{2 \sec \theta} \right) \\ f_{t1}(t_1) &= \exp \left\{ -\tilde{k}_{e2} c_{v2} t_1 \right\} p_{t1}(t_1) \\ f_{t2}(t_2) &= \exp \left\{ \tilde{k}_{e2} c_a t_2 \right\} p_{t2}(t_2) \end{aligned}$$

The modified Flat Surface Impulse Response is given by

$$P_{FS'}(t) = \frac{\lambda^2 c_a c_{v2}}{4(4\pi)^3} \int_0^\infty \int_0^{2\pi} \frac{\delta(t - 2r'/c)}{(r')^4} \frac{G^2(\theta_a, \phi_a) \sigma_s^0(\theta, \phi)}{\sec^2 \theta} \exp \left\{ -2 \sec \theta (\tilde{k}_{e1} d_1 + \tilde{k}_{e2} d_2) \right\} \rho \, d\rho \, d\phi$$

for layered media with a constant velocity in each media and where \tilde{k}_{e1} , \tilde{k}_{e2} are the effective extinction coefficients in medium 1 (foliage region) and medium 2 (trunk region), respectively.

4 Interaction between the Foliage and the Surface

The returned power from the volume must be modified by the addition of the time-delayed return from the rough surface under the random media. As previously seen, the radiative transfer method accounts for this second scattering event simply by assuming that the incident wave to the rough surface is due to an attenuated version of the original, free-space, time-delayed incident power waveform. The attenuation is due to the collection of scatterers along each radial from the antenna. After the power waveform is then scattered by the surface, it again travels back up through the foliage, suffering the same attenuation. The details of this approach were developed in the Chapter 3. A sample set of volume and surface scattered waveforms based on the radiative transfer results of Chapter 3 is given in the first section of this chapter.

Since many assumptions are inherent in the radiative transfer result, there is a question as to the validity of this approach. Can the interaction between the foliage and surface be modeled simply by this single interaction? The foliage scatters a field, \bar{E}_f^s , toward the antenna and other directions. This foliage scattered field, \bar{E}_f^s , is also incident on the rough surface in addition to the free space incident field \bar{E}^{inc} (see Figure 9). It is then scattered back through the foliage (see Figure 10) resulting in a second scattered field returned to the radar, \bar{E}_{fsf}^s , due to the foliage-surface-foliage interaction.

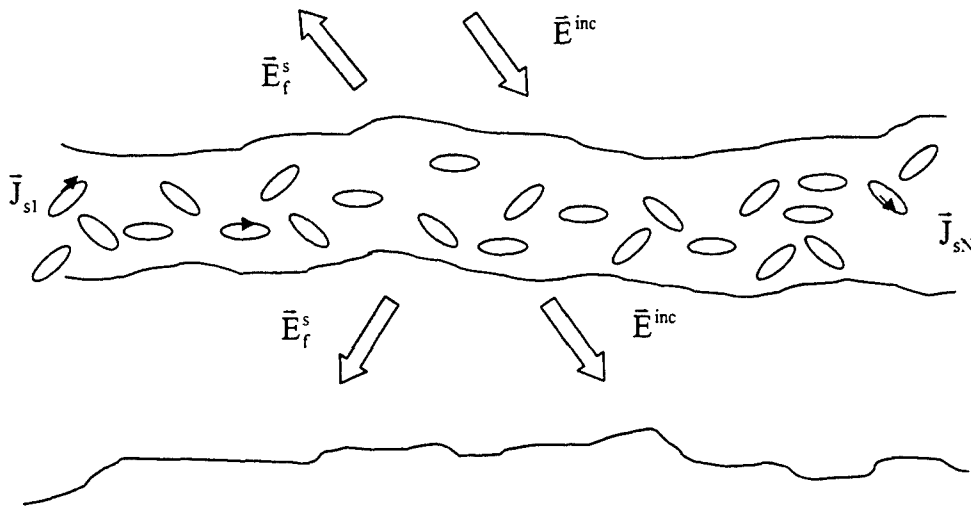


Figure 9: The total incident field with respect to the surface

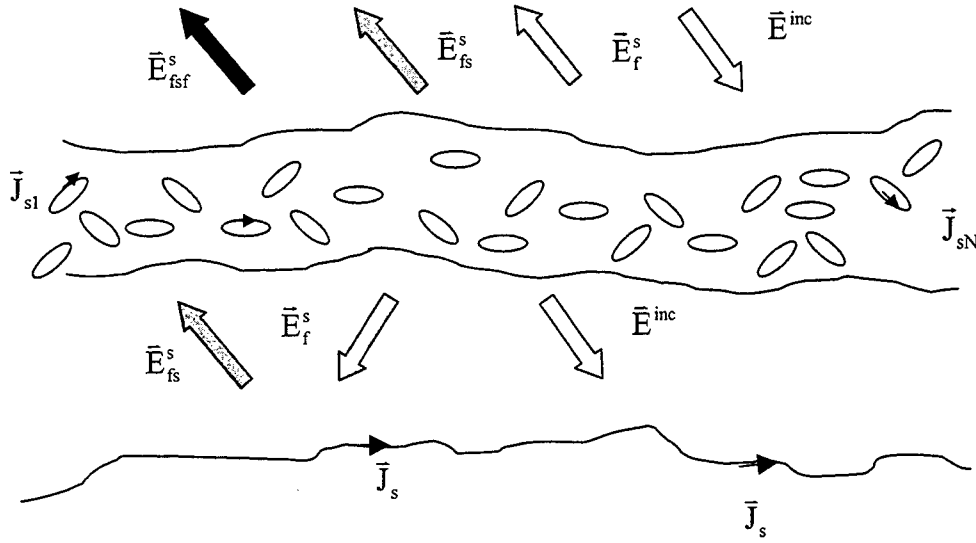


Figure 10: the first order approximate scattered field from the foliage and surface combination

Naturally, the question arises: are the multiple interactions between the foliage and the surface a necessary component in this portion of the model? That is, is there a significant second order surface interaction due to incidence of the field \vec{E}_{fsf}^s , the foliage-surface-foliage field, to the surface? In other words, when \vec{E}_{fsf}^s is incident on the surface (note the **addition** of \vec{E}_{fsf}^s into Figure 11 with respect to Figure 10) will there be a significant correction to the surface scattered field? This additional incident field will modify the surface currents, which will radiate, \vec{E}_{fsf}^s , creating a new foliage scattered field, \vec{E}_{fsfsf}^s . The third order approximation to the interaction between the foliage and the surface would repeat this process again. This process will continue indefinitely, or until the corrections become negligible. Notice that with each iteration, the final foliage scattered field is not used as an incident field for the surface.

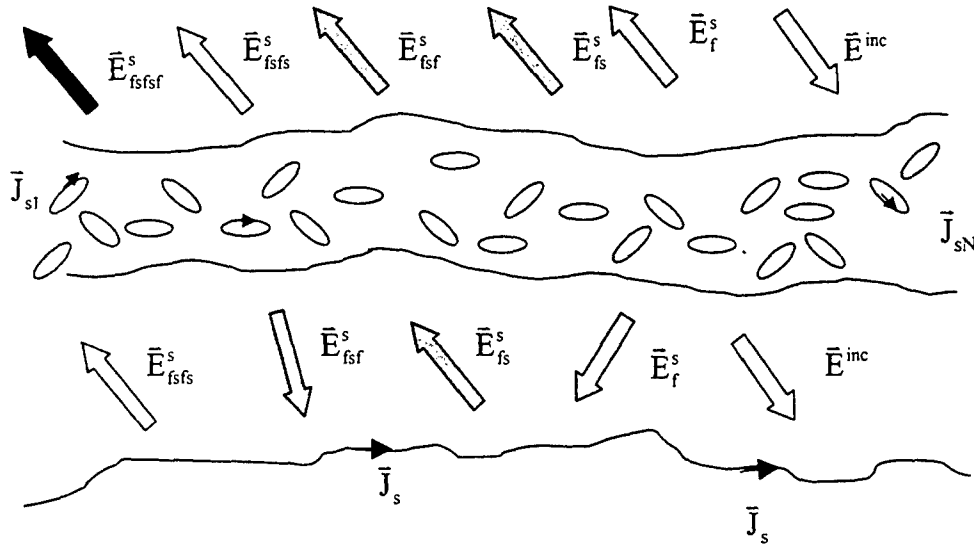


Figure 11: the second order approximate scattered field from the foliage and surface combination

Hence, extensions of this single passage event would include an infinite series of interactions between the foliage and the surface in the case of single scattering theory or fully coupled integral equations in the integral equation approach. Is the first order scattering interaction term adequate? Three methods of approximation to the second term have been or will be examined in this study:

1. Modified "First Order Multiple Scattering" theory
2. Exact formulation using the Method of Moments (MOM)
3. Reduced integral equation approach

Due to the complexity of the second approach listed only a limited number of scatterers can be placed above the surface. Hence, we will investigate the higher order interactions based on a single scatterer above a rough surface. Since the radiative transfer approach cannot simulate this situation, another approach was required. After some investigation the first listed approach was found to not only support the single scatterer

investigation, but also turned out to be a more general version of the radiative transfer result as developed in Chapter 3. This first order multiple scattering approach, under certain assumptions reduces to the result given for the radiative transfer approach. This is detailed in Appendix A.

The first approach, the modified first order multiple scattering result, does begin with a single scatterer. Hence, since the convolutional, radiative transfer approach is related to this method, we need only show that the foliage to surface to foliage interaction requires only the first order interaction, i.e. truncate the infinite series of interactions as previously described with only the first interaction to verify the assumption. A proposed method for extending this approach to a collection of discrete scatterers is also outlined. In addition, if this method were successfully implemented as a convolution, it would serve as a more general approach than the radiative transfer method as developed in the first section of this chapter.

Verification of the first order multiple scattering result will require a comparison with an exact solution. Consequently, the next section of this chapter examines the exact formulation for a single scatterer above a rough surface and solution via the efficient MOMI method as previously described. This result may serve as an exact result when compared with the first order multiple scattering solution obtained for a single scatterer above a rough surface.

Finally, in the following section, the exact integral equation method is simplified using some reasonable assumptions. This method will result in a more accurate method to simulate interaction between a single scatterer above a rough surface than the first order multiple scattering approach. In addition, it may also yield a more tractable numerical model when it is extended to a collection of scatterers above a rough surface than the full Method of Moments approach. This more accurate representation of the interaction may be required at some level of simulation.

4.1 Capabilities, Limitations and an Example Return Waveform for the Radiative Transfer Approach

Previously noted limitations of the radiative transfer result have included a limited scattering pattern for each volume scatterer and a narrow beamwidth approximation. The chosen scattering pattern demands strictly forward scattering and backward scattering. This assumptions decreases the number of coupled differential equations from N (when N scattering directions are used in a quadrature approximation to the integral in the radiative transfer equation) down to two: coupled integral equations, one governing forward and one reverse scattering. Secondly, the upwelling power density is assumed not to influence the downwelling. This last assumption is key since it allows a closed form solution for the downwelling power density. Otherwise, the solution would be in the form of two coupled differential equations.

In Appendix A, the radiative transfer result is shown to be equivalent to the first order multiple scattering result. From the first order multiple scattering analysis of Appendix A, another limitation of the radiative transfer approach has been identified: use of a narrow bandwidth approximation. This assumption is expected due to the use of a constant backscatter coefficient with respect to frequency. However, using the full, two-frequency mutual coherence function, it may be possible that the impulse response approach can be extended to broader bandwidth pulses in addition to broader beamwidth antenna patterns. This premise is still under investigation.

As a simple example, a simulation for a layered media with a constant propagation speed and constant extinction coefficient in each layer was performed. The results are shown in the following figures. The assumed parameters of the radar system are as follows:

- Waveform: Square Pulse with 5 ns pulse length
- Antenna: Gaussian pattern, 1 to 10 degree beamwidth
- 100,000m range to the surface at nadir pointing

The media is assumed to have the following bulk propagation properties (arbitrary estimates since no data was available) and Gaussian statistics:

1. The foliage layer
 - 20 meter thickness
 - effective extinction coefficient as noted
 - group velocity as noted
 - variance of the heights: 0.1 m^2
 - backscatter to forward scatter cross-section, $\sigma_f/\sigma_b : 500$
 - absorption to total scattering cross-section, $\sigma_a/\sigma_t : 0.9$
2. The trunk layer
 - 5 meter thickness
 - effective extinction coefficient as noted
 - group velocity as noted
 - backscatter to forward scatter cross-section, $\sigma_f/\sigma_b : 500$
 - absorption to total scattering cross-section, $\sigma_a/\sigma_t : 0.9$
3. The ground layer
 - Perfect electric conductor (PEC)
 - variance of the heights: 0.1 m^2

Figure 12 shows the simulated returned waveform for three different antenna beamwidths: 1, 5, and 10 degrees. As an aide to the understanding of these waveforms, the components of the composite wave for the one-degree case are shown in Figure 13; here, the composite waveform is the simple superposition of the volume and surface scattered waveforms. As you can see from Figure 13 for the one-degree beamwidth, the surface return begins after the volume return has decreased; hence in the composite waveform, the surface and volume return are still somewhat separable. The early return of the composite waveform is due to the volume response and its tail is attributable to the surface return. However, from Figure 12, for the five-degree beamwidth case, this distinction is less noticeable, whereas for the ten-degree beamwidth case, the surface and volume returns become indistinguishable.

Similarly, in Figure 14 and Figure 15, we see waveforms that are derived using the same parameters with the exception of propagation speed in the foliage and trunk regions: these have been reversed. In this case, since the electromagnetic depth of the media, commonly referred to as the optical depth, is much shorter, the surface and volume returns are easily separable. Again, Figure 15 explicitly shows the components of the composite waveform for a one-degree antenna beamwidth.

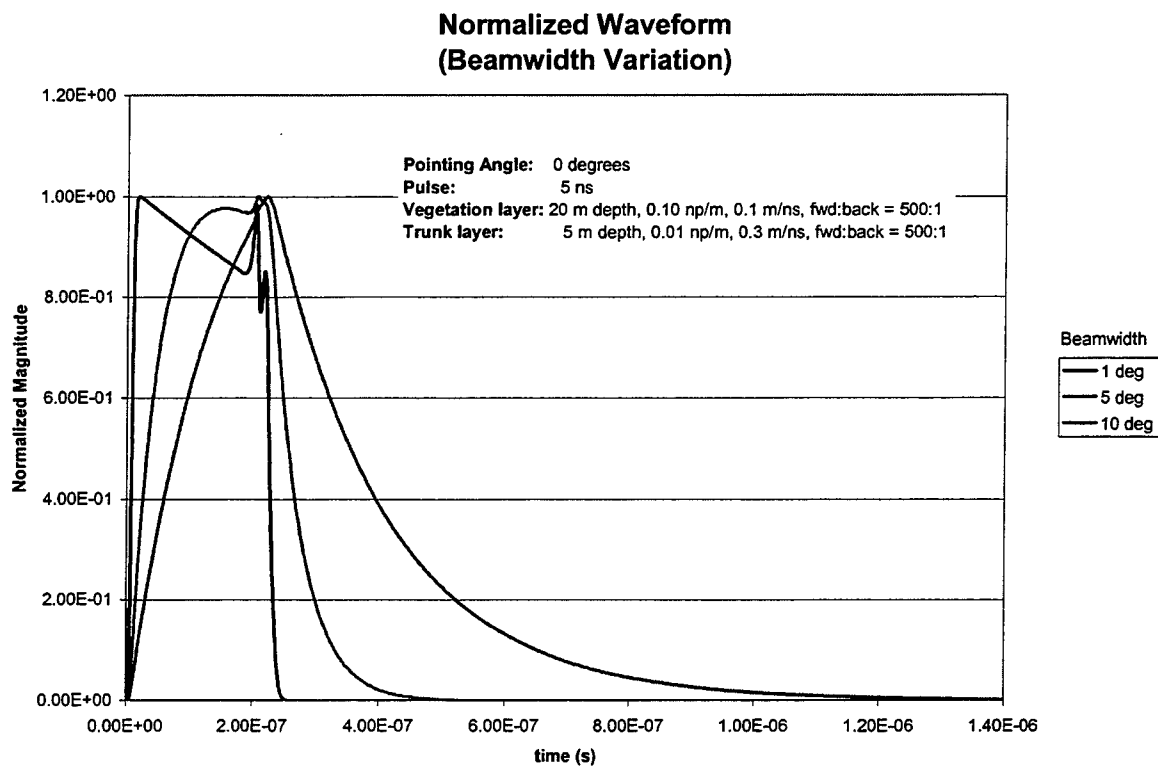


Figure 12: Composite waveform for 1, 5 and 10 degree antenna beamwidths

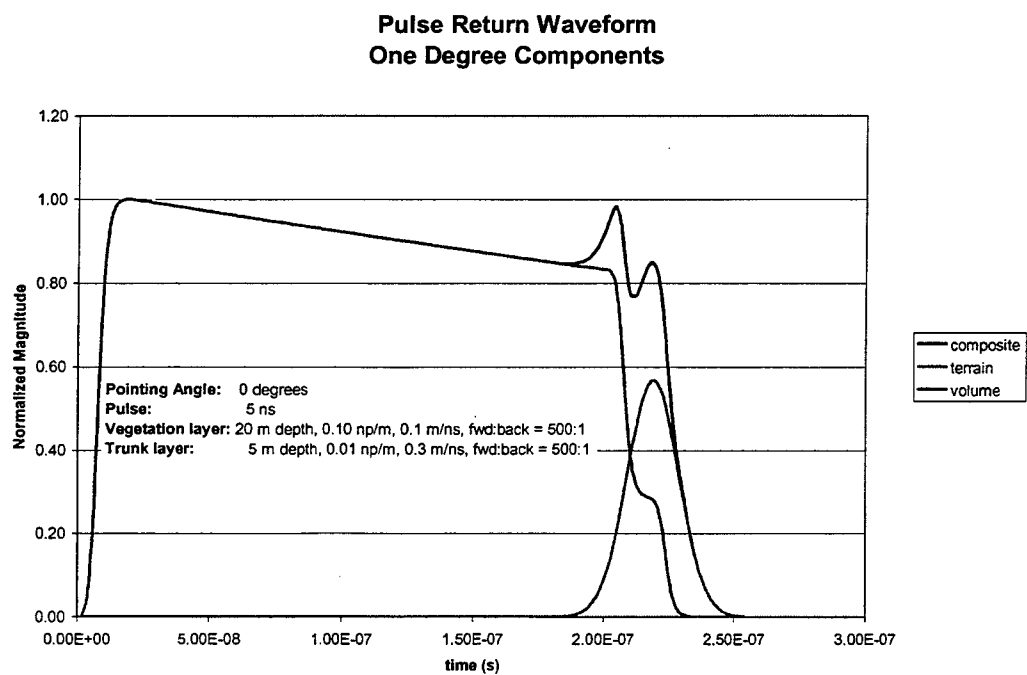


Figure 13: Components of the 1-degree case: Volume + Surface Returns

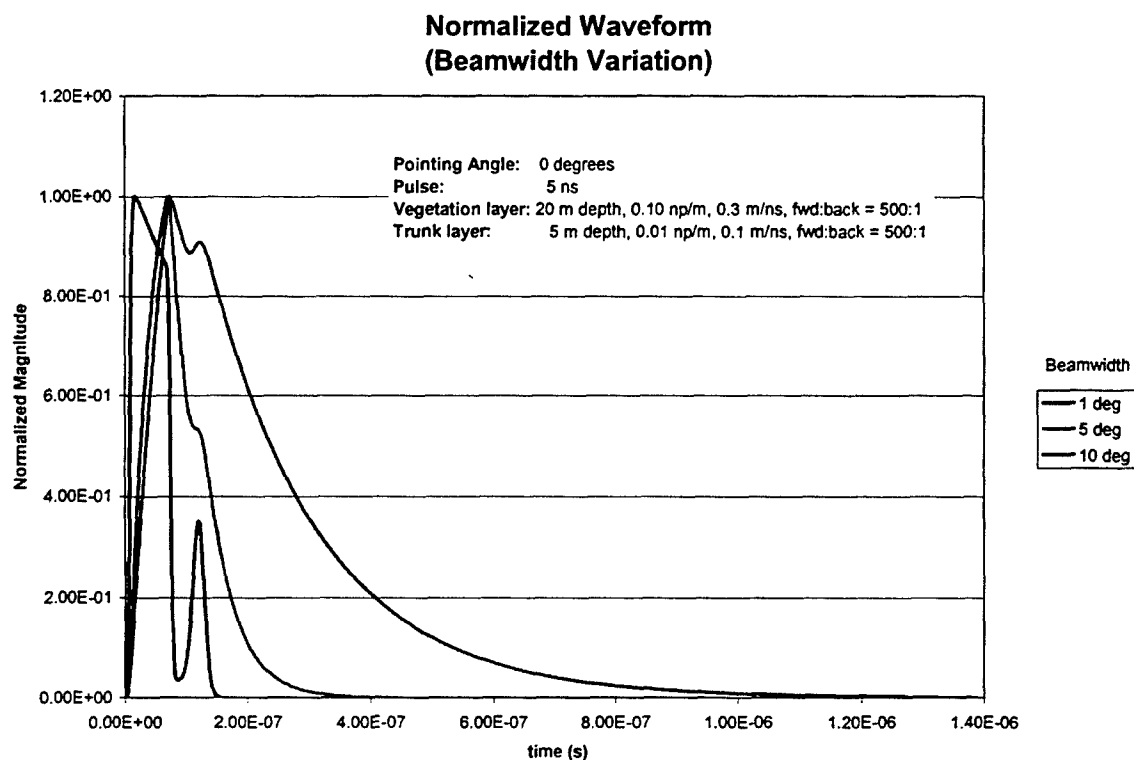


Figure 14: Composite waveform for 1, 5 and 10 degree antenna beamwidths

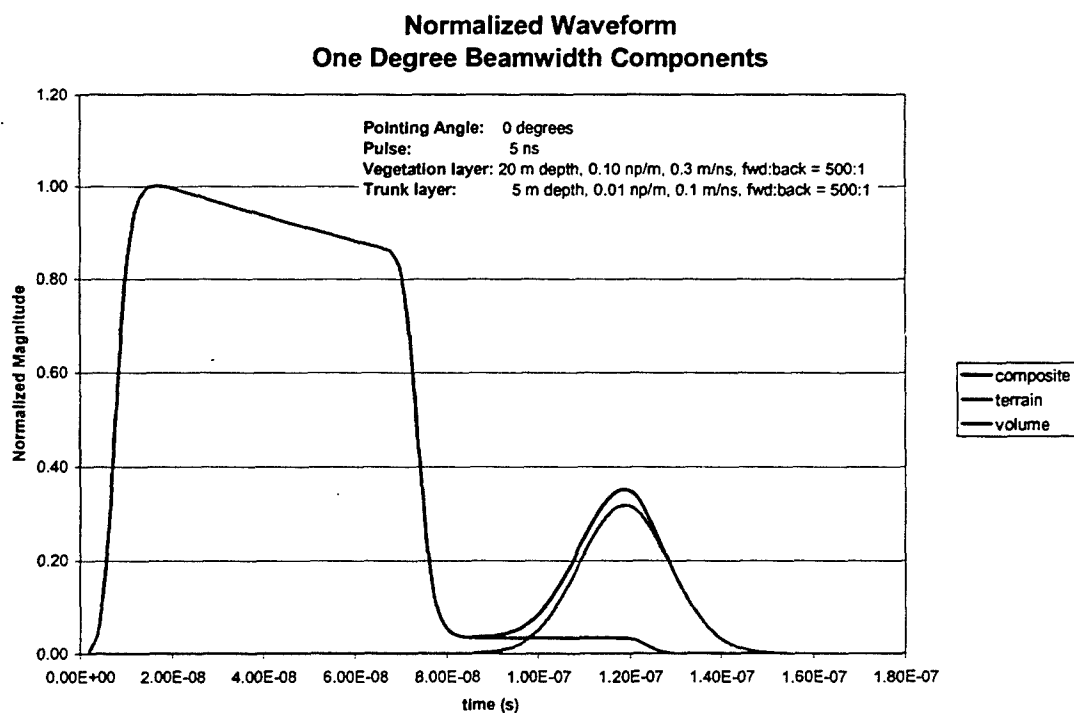


Figure 15: Components of the 1-degree case: Volume + Surface Returns

4.2 Modified Single Scatter Theory for a Single Scatterer over a Rough Surface

4.2.1 Introduction

As previously discussed the radiative transfer approach has simulated the foliage-surface-foliage scattering event with only a first order interaction in addition to some limiting assumptions. The review of the first order multiple scattering theory in Appendix A has shown not only the equivalence of this method to the radiative transfer method when the same assumptions are employed, but also a way to generalize these results to broader bandwidth, broader beam systems and less restrictive scattering functions. Consequently, in this section we hope to explore the extension of first order multiple scattering to foliage over a rough terrain. This extension will not only help remove some of the restrictions, but also provide a method to examine the validity of the first order interaction with the surface. This comparison is possible due to two reasons. First, using the first order multiple scattering results, we can produce results with multiple interactions between the foliage and the surface. Second, for a single scatterer over a rough surface, we can directly compare these results with exact numerical results as presented in the following section. The work in this section is still under development.

Appendix A has presented the first order multiple scattering result for scattering from a volume. This is based on single scatter theory and is equivalent to the radiative transfer approach previously outlined. A second important scattering event, in addition to the backscatter due to the volume alone, is the return from the surface. There are three possible mechanisms that may be responsible for this process, see Figure 16

1. Direct return from the surface in which no interaction with the volume scatterers has occurred.
2. A scattering event involving first a member of the volume of scatterers and then interaction with the surface
3. A scattering event involving first scattering from the surface and then interaction with a member of the volume of scatterers.

The first case corresponds to free space scattering by a rough surface that was discussed in Appendix A, or the radiative transfer result discussed in Chapter 3. The second and third cases have not been discussed. However, since the first case has already been discussed and the second and third cases are equivalent by reciprocity, we need only examine the second case: the scatter from the vegetation to the surface and back to the radar. If the scattering mechanism for foliage-to-surface-to-foliage is considered significant, this will be a simple extension of the results that follow.

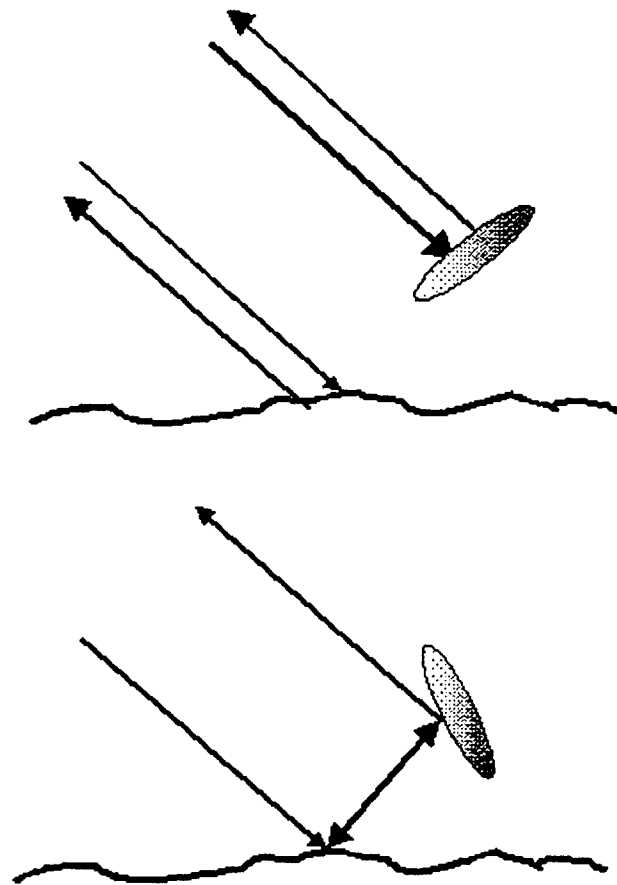


Figure 16: Particle and Surface Scattering Events

4.2.2 Development of the Model

Given the scattering pattern of the scatterer and the two-frequency mutual coherence function of the scatterer, the power density scattered toward the surface can be quantified as follows, see Appendix A [Ishimaru, 1997]:

$$I(t; \theta_s, \phi_s) = \iiint_{\text{volume of scatterers}} \left[\int_{-\infty}^{\infty} A\left(\omega_1, t - \frac{r_s}{c}\right) e^{j\omega_1 t} d\omega_1 \right] \left[\int_{-\infty}^{\infty} A\left(\omega_2, t - \frac{r_s}{c}\right) e^{j\omega_2 t} d\omega_2 \right]^* \rho dV \quad (1)$$

where r_s is the distance from the antenna to the scatterer and the product of the transfer function and the complex envelope, $U_i(\omega)$, of the incident waveform is given by

$$A(t, \omega_n) = U_i(\omega_n) \tilde{F}(\omega_n; \hat{k}_s, \hat{k}_i) g(\omega; \hat{k}_i) \frac{e^{-jk_r s}}{r_s} \exp\left\{-\int_{r_i}^{r_s} \rho \langle \sigma_t \rangle dR\right\} \quad (2)$$

and the unit vectors, $\hat{k}_s = (\theta_s, \phi_s)$, $\hat{k}_i = (\theta_i, \phi_i)$, represent the incident and scattered directions with respect to the scatterer, respectively. The function $g(\omega, \hat{k}_i)$ is related to the antenna pattern; $\tilde{F}(\omega_n; \hat{k}_s, \hat{k}_i)$ is the Fourier Transform of the scattering function $\tilde{f}(\hat{k}_s, \hat{k}_i)$, and $U_i(\omega_n)$ of the complex envelope of the incident pulse at a given frequency. See Appendix A for additional, more detailed definitions.

The expression (1) describes the pulse shape, amplitude and the scattering pattern of the scattered power waveform due to a volume of scatterers, each at a variable distance r_s from the antenna. The observation location is on the terrain at a distance r_g from each scatterer. See Figure 17. If the narrow band approximation can be used, this expression can be simplified to

$$I(t; \theta_s, \phi_s) = \iiint_{\text{volume of scatterers}} \frac{G(\theta_s, \phi_s)}{(4\pi)^3 r_s^2 r_g^2} \sigma_{bi}(\hat{k}_s, \hat{k}_i) P_T\left(t - \frac{r_s}{c}\right) \exp\left\{-\int_{r_i}^{r_s} \rho \langle \sigma_t \rangle dR\right\} \exp\left\{-\int_{r_g}^{r_s} \rho \langle \sigma_t \rangle dR\right\} \rho dV \quad (3)$$

where $\sigma_{bi}(\hat{k}_s, \hat{k}_i)$ is the bistatic scattering cross section of the scatterer assuming a scattered waveform in the \hat{k}_s direction and given an incident field in the \hat{k}_i direction at a range r_g with respect to the scatterer's local coordinates. Note that this bistatic cross section can be used due to the narrow band assumption that results in a particularly simple form for the two-frequency mutual coherence function. In general, this term is the integration of the product of the two-frequency mutual coherence function, the antenna gain as a function of frequency and the complex amplitude with its complex conjugate over all frequencies, see equation (2) and Appendix A.

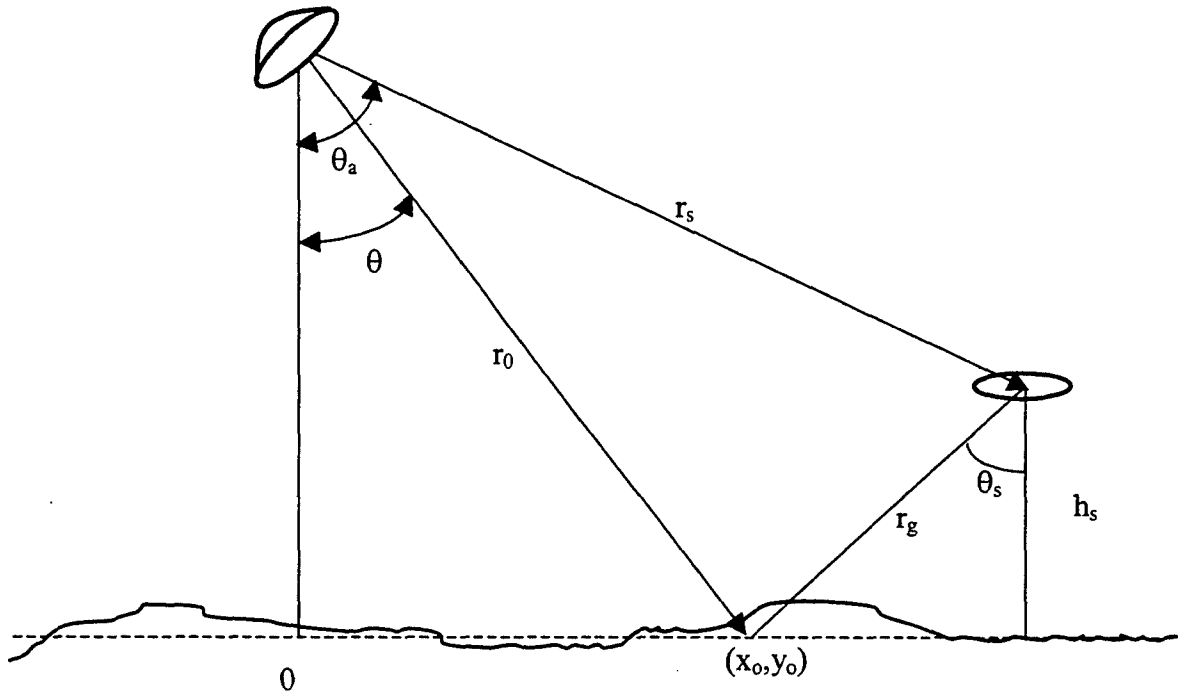


Figure 17: Geometry for Foliage-Surface-Foliage Scattering Event

Now we shall consider the scattered power density from a *single* scatterer over a rough surface. Using the geometry found in Figure 17, we can derive the first order multiple scattering result for this scatterer. In either case broadband or narrowband, the scattered power waveform created by the scatterer due to its incident field from the antenna can be thought of as a secondary source with respect to the surface and the original source, the antenna. Now the surface has two incident power waveforms: the free

space power waveform due to the antenna and the power waveform created by the scatterer. The scattered waveform from the scatterer, is described by expressions (1) and (3). Considering the power waveform scattered by the scatterer as a second source, $I(t; \theta_s, \phi_s)$ represents the product of the transmitted power waveform due to the scatterer, $P_{T,S}(t)$, as modified by an assumed “antenna pattern” for the scatterer, $G_s(\theta_s, \phi_s)$. First we will re-express equations (1) and (3) for the specific case of a single scatterer.

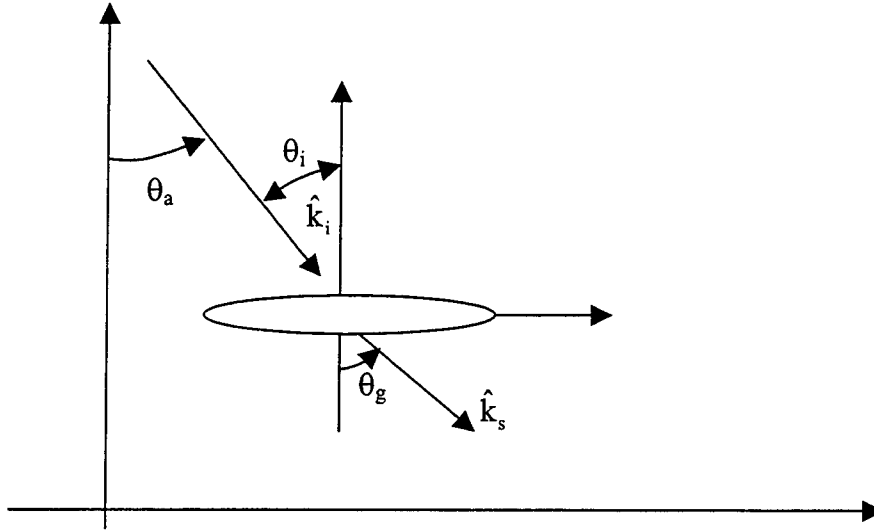


Figure 18: the geometry of the scatterer

If we consider a single scatterer under the narrow band approximation, the expression for the power density *incident on the scatterer* is found under the first order multiple scattering theory to be

$$I(t; \theta_a, \phi_a) = \frac{G_a(\theta_a, \phi_a)}{4\pi r_s^2} \exp\left\{-\int_{r_i}^{r_s} \tilde{k}_e(\mu) d\mu\right\} P_T\left(t - \frac{r_s}{c}\right)$$

here, $P_T(t)$ is the radar's transmitted waveform that has been attenuated by the exponential factor and weighted by the radar's antenna gain $G_a(\theta_a, \phi_a)$ in the direction of the scatterer, (θ_a, ϕ_a) . These angles describe the angle of the scatterer with respect to the antenna in the antenna's reference frame and r_s is the distance from the antenna to the scatterer. Employing the bistatic radar cross-section, $\sigma_{bi}(\hat{k}_s, \hat{k}_i)$, the waveform scattered

in the \hat{k}_s or (θ_s, ϕ_s) direction given an incident field in the \hat{k}_i direction with respect to the scatterer's local coordinates can be written as

$$I(t; \theta_s, \phi_s) = \left\{ \frac{G_a(\theta_a, \phi_a)}{4\pi r_s^2} \exp\left\{-\int_{r_i}^{r_s} \tilde{k}_e(\mu) d\mu\right\} P_T\left(t - \frac{r_s}{c}\right) \right\} \sigma_{bi}(\hat{k}_s, \hat{k}_i) \quad (4)$$

The "scattering pattern" of the scatterer in the direction from the scatterer to the terrain, (θ_g, ϕ_g) , is the analogous normalized antenna pattern of the new source with a normalized antenna pattern given by

$$G_s(\theta_g, \phi_g) = \frac{\sigma_{bi}(\hat{k}_s, \hat{k}_i)}{\sigma_{bi}^{\max}} \quad (5)$$

and the analogous transmitted power density from the scatterer is given by

$$P_{T,S}(t) = \frac{G_a(\theta_a, \phi_a)}{4\pi r_s^2} \exp\left\{-\int_{r_i}^{r_s} \tilde{k}_e(\mu) d\mu\right\} \sigma_{bi}^{\max} P_T\left(t - \frac{r_s}{c}\right) \quad (6)$$

Note that the product of (5) and (6) is equal to (4). Recall that the angles using subscript "a" refer to the angle between the antenna and the scatterer in the antenna's local coordinate system and r_s , refers to the slant range from the antenna to the scatterer; see Figure 17. In the general broadband case, these quantities are not so easily separated since they remain buried in the inverse transforms. This matter requires further investigation.

Next, we consider the foliage-surface scattered power collected by the radar. From the discussions involving the flat surface impulse response, the solution for the average incoherent response of a scatterer over a rough surface can be developed. We begin with an expression for the returned power waveform which is similar to that given in Chapter 2 describing the impulse response method for a rough surface in free space,

$$P_R(t) = \frac{\lambda^2}{(4\pi)^3} \int_0^\infty \int_0^{2\pi} \frac{P_T\left(t - \frac{2(r_0 - \xi(x, y) \sec \theta)}{c_0}\right)}{(r_0 - \xi(x, y) \sec \theta)^4} G^2(\theta, \phi) \sigma^0(\theta, \phi) \rho d\phi d\rho$$

In this case, the transmitter and receiver are at the same location and have the same antenna pattern; the slant range from antenna to surface is simply traversed twice. When the scatterer acts as a source, however, and the radar antenna collects energy, the expression must change to reflect

1. the different distances: from the scatterer to the surface element, $r_g - \xi(x, y) \sec \theta_s$ and from the radar antenna to the surface element, $r_0 - \xi(x, y) \sec \theta$; these range variations affect the delay time as well.
2. the different "antenna patterns": from the scatterer, $G_s(\theta_s, \phi_s)$ with respect to the surface and from the radar antenna, $G_a(\theta, \phi)$, with respect to the surface, each in its own coordinate system.
3. The bistatic radar cross section per unit area with an incident angle, \hat{k}_i or (θ_i, ϕ_i) and scattered angle \hat{k}_s or (θ_s, ϕ_s) with respect to the antenna's coordinate system, see Figure 18.

Hence, the expression for the incoherent power returned from the surface as a function of time due to the scattered energy in the foliage-surface interaction can be written as

$$P_R(t) = \frac{\lambda^2}{(4\pi)^3} \int_0^\infty \int_0^{2\pi} \frac{P_{T,S} \left(t - \frac{(r_g - \xi(x, y) \sec \theta_s)}{c_0} - \frac{(r_0 - \xi(x, y) \sec \theta)}{c_0} \right)}{(r_g - \xi(x, y) \sec \theta_s)^2 (r_0 - \xi(x, y) \sec \theta)^2} \cdot G_s(\theta_s, \phi_s) G_a(\theta, \phi) \sigma^0(\theta_s, \phi_s; \theta, \phi) \rho d\phi d\rho \quad (7)$$

note that the incident power waveform is that from the scatterer, $P_{T,S}$ defined by equation (6). Simplifying this result under the assumption that the surface height is negligible in the amplitude terms, and recognizing the equivalence of the radar coordinates and the polar coordinates defined on the surface, we find

$$P_R(t) \cong \frac{\lambda^2}{(4\pi)^3} \int_0^\infty \int_0^{2\pi} \frac{P_{T,S} \left(t - \frac{(r_g + r_0)}{c_0} + \frac{\xi(x,y)(\sec \theta_s + \sec \theta)}{c_0} \right)}{r_0^2 r_g^2} \cdot G_s(\theta_s, \phi_s) G_a(\theta, \phi) \sigma^0(\theta_s, \phi_s; \theta, \phi) r_0 dr_0 d\phi$$

The integration over the surface is performed in the antenna coordinates. Assuming the angles above can be measured from the mean plane, a relationship between the "scatterer-to-ground" angles, subscripted "s", and the "antenna-to-ground" angles, not subscripted, can be found with respect to the antenna frame of reference in the following symbolic manner. Let

$$\theta_s = f_s(\theta) = \tan^{-1} \left(\frac{(x - x_0)^2 + (y - y_0)^2}{h_s} \right)$$

$$\phi_s = g_s(\phi) = \pm \tan^{-1} \left(\frac{x - x_0}{y - y_0} \right)$$

In addition the slant range from the scatterer to the terrain can be found in terms of the antenna coordinates. Given that the scatterer is located at the coordinates (x_0, y_0, h_s) , the distance from the scatterer to the surface is expressed as follows, see Figure 17

$$r_g^2 = (x - x_0)^2 + (y - y_0)^2 + h_s^2$$

$$\text{with } (x, y) = (r_0 \sin \theta \cos \phi, r_0 \sin \theta \sin \phi)$$

Hence, establishing a reference frame on the antenna, we express all angles relative to the spherical coordinates centered at the antenna. Consequently, expressed entirely in the antenna's frame of reference, the power return waveform becomes

$$P_R(t) \cong \frac{\lambda^2}{(4\pi)^3} \int_0^\infty \int_0^{2\pi} \frac{P_{T,S} \left(t - \frac{(r_g + r_0)}{c_0} + \frac{\xi(x,y)(\sec(f_s(\theta)) + \sec \theta)}{c_0} \right)}{(r_0)^2 (r_g)^2} \cdot G_s(f_s(\theta), f_s(\phi)) G_a(\theta, \phi) \sigma^0(f_s(\theta), g_s(\phi); \theta, \phi) r_0 d\phi dr_0 \quad (8)$$

where each angle and distance is now measured in terms of the antenna/radar coordinates. Averaging these results by the surface heights, ξ , the average incoherent power returned becomes

$$\langle P_R(t) \rangle \cong \int_{-\infty}^{\infty} \frac{\lambda^2}{(4\pi)^3} \int_0^{\infty} \int_0^{2\pi} \frac{P_{T,S} \left(t - \frac{(r_g + r_0)}{c_0} + \frac{\xi(x,y)(\sec(f_s(\theta)) + \sec \theta)}{c_0} \right)}{r_g^2 r_0^2} p_{\xi}(\xi) \cdot G_s(f_s(\theta), f_s(\phi)) G_a(\theta, \phi) \sigma^0(f_s(\theta), g_s(\phi); \theta, \phi) r_0 d\phi dr_0 d\xi \quad (9)$$

where the probability density function (pdf) for the surface heights has been given by $p_{\xi}(\xi)$. With a change of variables for the heights given by

$$\tilde{\xi}(x,y) = \frac{\xi(x,y)(\sec(f_s(\theta)) + \sec \theta)}{c_0}$$

and the corresponding transformation of the pdf given by

$$p_{\tilde{\xi}}(\tilde{\xi}) = \frac{c_0}{(\sec(f_s(\theta)) + \sec \theta)} p_{\xi} \left(\frac{c_0 \tilde{\xi}}{(\sec(f_s(\theta)) + \sec \theta)} \right)$$

the average returned power can be re-written as

$$\langle P_R(t) \rangle \cong \frac{\lambda^2}{(4\pi)^3} \int_0^{\infty} \int_0^{2\pi} \frac{c_0}{(\sec(f_s(\theta)) + \sec \theta)} \int_{-\infty}^{\infty} \frac{P_{T,S} \left(t - \frac{(r_g + r_0)}{c_0} + \tilde{\xi}(x,y) \right)}{r_g^2 r_0^2} p_{\tilde{\xi}}(\tilde{\xi}) d\tilde{\xi} \cdot G_s(f_s(\theta), f_s(\phi)) G_a(\theta, \phi) \sigma^0(f_s(\theta), g_s(\phi); \theta, \phi) r_0 d\phi dr_0$$

the returned average incoherent power can be expressed in a convolutional form, with the symbol \otimes denoting convolution.

$$\langle P_R(t) \rangle \cong \frac{\lambda^2}{(4\pi)^3} \int_0^\infty \int_0^{2\pi} \frac{P_{T,S}\left(t - \frac{(r_g + r_0)}{c_0}\right) \otimes p_{\tilde{\xi}}\left(t - \frac{(r_g + r_0)}{c_0}\right)}{r_g^2 r_0^2} \frac{c_0}{(\sec(f_s(\theta)) + \sec \theta)} \cdot G_s(f_s(\theta), g_s(\phi)) G_a(\theta, \phi) \sigma_s^0(f_s(\theta), g_s(\phi); \theta, \phi) r_0 d\phi dr_0 \quad (10)$$

Taking advantage of the properties of the delta function,

$$\langle P_R(t) \rangle \cong \int_{-\infty}^\infty \frac{\lambda^2}{(4\pi)^3} \int_0^\infty \int_0^{2\pi} \frac{P_{T,S}(t-t') \otimes p_{\tilde{\xi}}(t-t')}{r_0^2 r_g^2} \delta\left(t' - \frac{(r_g + r_0)}{c_0}\right) \frac{c_0}{(\sec(f_s(\theta)) + \sec \theta)} \cdot G_s(f_s(\theta), f_s(\phi)) G_a(\theta, \phi) \sigma_s^0(f_s(\theta), g_s(\phi); \theta, \phi) r_0 d\phi dr_0 dt' \quad (11)$$

Next, we invoke the narrow beam approximation for the dependence of the argument for the pdf and we approximate θ with the boresight angle, θ_0 .

$$p_{\tilde{\xi}}(t) = \frac{c_0}{\sec(f_s(\theta_0)) + \sec \theta_0} p_{\xi}\left(\frac{c_0 t}{\sec(f_s(\theta_0)) + \sec \theta_0}\right)$$

Finally, the expression for the average power returned from the scattering event: antenna-to-scatterer-to-ground-to-antenna, can be represented by the convolutional product

$$\langle P_R(t) \rangle \cong P_{T,S}(t) \otimes p_{\tilde{\xi}}(t) \otimes P_{FS,S}(t) \quad (12)$$

where

$$P_{FS,S}(t) \cong \frac{\lambda^2}{(4\pi)^3} \int_0^\infty \int_0^{2\pi} \frac{\delta\left(t' - \frac{(f_r(r_0) + r_0)}{c_0}\right)}{(f_r(r_0))^2 (r_0)^2} \frac{c_0}{(\sec(f_s(\theta)) + \sec \theta)} \cdot G_s(f_s(\theta), g_s(\phi)) G_a(\theta, \phi) \sigma_s^0(f_s(\theta), g_s(\phi); \theta, \phi) r_0 d\phi dr_0$$

Note that the height of the single scatterer, h_s , and its orientation, Ω , can be made random variables as well; this formulation has yet to be investigated. The random orientation of

the scatterer will require that the boresight angle of G_s , the scatterer's "gain pattern," be a random variable. A scatterer with a random height will result in the distance r_g and the associated angles to become random variables. The final average return power from the surface due to a single scatterer will then require that we average only the modified flat surface impulse response, $P_{FS,S}(t)$. Hence the averaged incoherent power returned will be of the form

$$\langle P_R(t) \rangle \cong P_{T,S}(t) \otimes p_{\tilde{\xi}}(t) \otimes \langle P_{FS,S}(t) \rangle \quad (13)$$

where

$$\langle P_{FS,S}(t) \rangle \cong \frac{\lambda^2}{(4\pi)^3} \int_0^\infty \int_0^{2\pi} \left\langle \frac{\delta\left(t' - \frac{(f_r(r_0) + r_0)}{c_0}\right) \sigma^0(f_s(\theta), g_s(\phi); \theta, \phi)}{(f_r(r_0))^2 (r_0)^2} \right\rangle_{h_s} \cdot \langle G_s(f_s(\theta), g_s(\phi)) \rangle_\Omega G_a(\theta, \phi) r_0 d\phi dr_0$$

where h_s = a random height for scatterer N

Ω = a random orientation for scatterer N

and $\langle \bullet \rangle_\alpha$ is interpreted as ensemble averaging with respect to the random variable α

Now the return from the surface and the scatterer combination is a superposition of the return from the volume and that from the surface. Consequently, the incoherent response from N, randomly oriented, scatterers at random heights can be expressed as

$$\langle P(t) \rangle = P_{T,S}(t) \otimes p_{\tilde{\xi}}(t) \otimes P_{FS}(t) + \sum_{n=1}^N P_{T,S}(t) \otimes p_{\tilde{\xi}}(t) \otimes \langle P_{FS,S}(t) \rangle \quad (14)$$

The first term is the incoherent power received directly from the scatterers as described in the radiative transfer section or the first order multiple scattering description. The second term is the response for N, randomly oriented scatterers at random heights above a

random surface. A third term may be added, if it is expected that there will be significant return directly from the surface without interaction from the scatterers.

4.2.3 Conclusions and Future Efforts

In this section, an outline for predicting the average incoherent power returned from a single scatterer and N randomly oriented scatterers at a random height above a rough surface has been presented. Implemented, this model will accomplish the following with respect to the radiative transfer model.

1. When N scatterers are used, the radiative transfer results should be duplicated if a single interaction is considered along with the narrow beam, narrow bandwidth and restricted scattering pattern assumptions as detailed in Chapter 3, the radiative transfer approach.
2. The above restrictions may be relaxed in the first order multiple scattering approach in order to judge their effect; thus supporting or further generalizing the radiative transfer result of Chapter 3.
 - The scattering pattern may be chosen more realistically
 - The beamwidth of the illuminating antenna and the bandwidth of the signal may be increased (with the possible sacrifice of the convolutional form)
 - Including the higher order interactions between the foliage and the surface may check the single passage assumptions.
 - If the radiative transfer results prove to be too restrictive through the implementation of these generalizations, this model will serve as the next possible approach.
3. Simulation of a single scatterer above a rough surface may be checked via exact numerical calculations as outlined in the next section of this chapter, thus checking the first order multiple scattering approach (with higher order interactions between the surface and the scatterer) and ultimately the radiative transfer model.

The implementation of a single scatterer placed deterministically above a rough surface must be accomplished first. These results will be compared with the exact results as discussed in the next section. The formal implementation of a randomly oriented and randomly positioned particle must then be formulated. Averaging the new Flat Surface Impulse Response will be attempted. Once this accomplished, we extend this technique to N scatterers as discusses in the previous section. Using the Foldy-Lax-Twersky integral equation, we can establish the effective media for the first order multiple scattering results and obtain a result that is similar to the Distorted Wave Born Approximation (DWBA); consequently, these results may be compared with those obtained by Lang [1981]. Finally, the broadband approach must be fully explored. The challenges in this extension include keeping our results in the fully convolutional form obtained for the narrowband case. Most likely, we will choose a scattering function that is simple and practical such as that presented by Schwering [1985]

4.3 Exact Solution to the Single Scatterer above a Rough Surface

The impulse response model, like most radiative transfer models, does not account for any interaction between the scatterers (foliage) and the boundary (surface). In establishing a range of validity for this assumption, a measure and threshold of “no interaction” must be established. Once this measure is established, numerous simulations of the exact scattered field must be examined in order to verify this assumption over a large parameter space including

- the scatterer’s size normalized to wavelength
- the scatterer’s separation from the rough surface normalized to wavelength
- the scatterer’s orientation (if it is not circular)

Consequently, we must assess the magnitude of the contribution of multiple scattering interactions between the scatterer and the rough surface. One approach to establishing the measure of significant interaction would be to include each level of multiple scattering and measure its contribution to the exact solution. Hence, we begin with the assumption that the surface and the scatterer do not interact. Next, we assess the correction for a single scatter interaction.

In order to verify this assumption of independent scattering, an “exact” numerical model has been created using the method of moments (MOM); the numerical solution for the currents on the scatterer and the rough surface accounts for all orders of interactions. After the problem is cast into the proper integral equation, the geometry is discretized in preparation for a solution via the familiar Method of Moments (MOM). Specifically, the Method of Ordered Multiple Interactions (MOMI) has been modified and is implemented as a solution method. This will be described in Section 14.34.3.1. Once the currents are found from the integral equation, the scattered fields can be simply found using the proper radiation integral; the far-field formulation has been used. A brief description of the MOMI as originally applied to rough surfaces can be found in Chapter 2.

4.3.1 Extension of the MOMI to Closed Bodies

The MOMI method, as discussed in Chapter 2, is a solution method for the MOM derived matrix equation of the following form:

$$\psi = \psi^{inc} + P\psi \quad (1)$$

where P is a propagator matrix, ψ is an unknown scalar field and ψ^{inc} is the known incident field. In developing MOMI to analyze scattering from extended rough surfaces, the self-interaction terms P_{ii} were neglected [Kapp and Brown, 1996]. The propagator matrix (P) was thus decomposed into lower triangular (L) and upper triangular (U) matrices, each having zero entries along the diagonal,

$$P \rightarrow L + U \quad (2)$$

After a few simple manipulations, this decomposition led to the MOMI matrix equation given in Chapter 2. However, consistent discretization of (1) requires that the diagonal elements P_{ii} be retained [Toporkov, 1998]. This modification can be incorporated in several ways. In applying MOMI to integral equations having singular kernels, it has been found that optimal convergence properties are obtained by decomposing the propagator matrix as

$$P \rightarrow L + \hat{D} + U \quad (3)$$

where \hat{D} is a diagonal matrix with $\hat{D} = P_{ii}$. Physically, maintaining the self interaction terms in \hat{D} separate from (L) and (U) provides better convergence properties when applying the method to integral equations having singular kernels because these equations exhibit strong coupling between oppositely directed fields on the surface of a scatterer [Adams and Brown, 1997].

The decomposition (3) leads to the matrix equation

$$\psi = (D - U)^{-1} D (D - L)^{-1} \psi^{inc} + P_M \psi \quad (4)$$

where $D = I - \hat{D}$ and the MOMI propagator, P_M , is defined as

$$P_M = (D - U)^{-1} D (D - L)^{-1} L D^{-1} U \quad (5)$$

Neumann iteration of (4) yields the candidate solution

$$\psi = \sum_{n=0}^{\infty} P_M^n (D - U)^{-1} D (D - L)^{-1} \psi^{inc} \quad (6)$$

which is the same as equation (28) of [Kapp and Brown, 1996] under the substitution $D \rightarrow I$. Since $D = I + O(\Delta x)$, the convergence properties of (6) are essentially unchanged from those of equation (28) of [Kapp and Brown, 1996]. When convergence occurs, the candidate solution (6) converges to the exact solution of (1). As discussed below, even in cases for which the infinite series does not converge, the first few terms of (6) can still provide a good approximation to the actual solution.

The MOMI series (6) provides a very robust and rapidly convergent solution to the MFIE for scattering from extended rough surfaces in two dimensions. The series has never been observed to diverge. These desirable properties have been attributed to the manner in which the MOMI series re-sums the multiple scattering terms present in the Neumann series for the original integral equation (1). The Born term in the MOMI series, $(D - U)^{-1} D (D - L)^{-1} \psi^{inc}$, includes the contributions to the current due to all orders of continuous forward scattering $(D - L)^{-1}$, all orders of backscattering, $(D - U)^{-1}$, and one order of interaction between the backward and forward traveling waves on the surface (resulting from the multiplication of these operators). Thus, the Born term includes interactions of up to order N. The largest effect neglected by the order zero iterate of the MOMI series is that of a wave which twice changes directions on the rough surface before again interacting with the currents on the surface - a triple scattering event.

For this reason, the ordering of the unknowns in the original matrix equation (1) can have a drastic effect on the convergence of the MOMI series. This is in contrast to the Neumann series for (1) whose convergence properties are independent of the manner in which the unknowns are ordered in the matrix equation. A different ordering of unknowns in the MOMI series will result in the summation of different multiple scattering terms. In the case of a random ordering of the unknowns in the original matrix equation (1) for the rough surface scattering problem, the number of MOMI iterations required to converge to a given error tolerance can be orders of magnitude larger than in

the case of the physically based forward-backward ordering. It is not immediately clear how the unknowns in (1) should be ordered for the application of MOMI to closed body scattering problems. In the case of elliptical cylinders, at least two ordering schemes incorporate important physical aspects of the scattering problem. These methods of ordering the unknowns in the matrix equation are illustrated in Figure 19. An ordering which is sequential-in- ϕ (SIP) produces an iterative series that mimics the progression of creeping waves around the surface of the cylinder. An alternative approach is one that is sequential-in- x (SIX). This ordering results in a MOMI series for the closed body problem which is somewhat analogous to the forward-backward approach used in [Kapp and Brown, 1996].

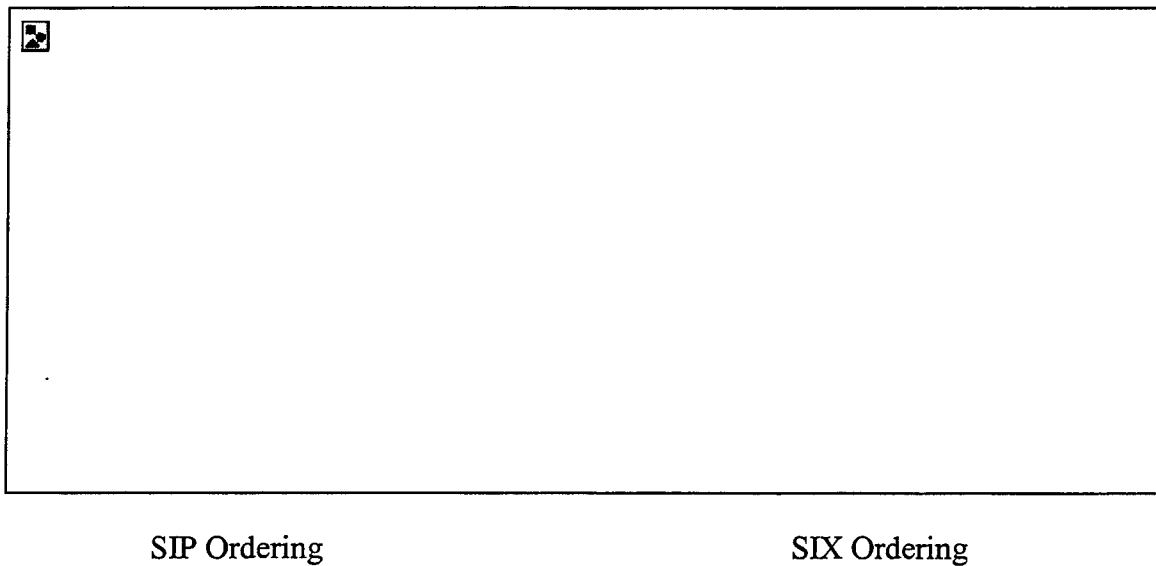


Figure 19 :Ordering of the Unknowns

4.3.2 A Combined Field Formulation

Given this understanding, we next consider a formulation of the scattering problem that does not give rise to a singular or nearly singular integral equation. In the following we consider a combined field integral equation (CFIE) representation [Mautz, 1978]. The CFIE is a linear combination of the MFIE and the EFIE as indicated below.

$$\alpha \text{EFIE} + \text{MFIE} = \text{CFIE}_\alpha$$

While the CFIE can be used to provide a unique solution to the scattering problem, the use of MOMI as formulated with a combined field description of the scattering problem introduces additional difficulties associated with the kernels of the EFIEs. The EFIE kernel for the TE problem is simply the Green's function of the Helmholtz equation. For TM scattering the kernel function is the second normal derivative of the Green's function. In applying the MOMI series to scattering from dielectric surfaces it has been found that the singularities of these kernel functions produce strong coupling between oppositely directed fields [Adams and Brown, 1997]. The singularity present in the EFIE for TM scattering is particularly strong and requires that a modified form of (4.3.1-6) be used. The singularity of the EFIE kernel for TE scattering is much weaker and is therefore more amenable to the MOMI series solution technique. For this reason, in the following we investigate the application of MOMI to the CFIE for TE scattering only.

4.3.3 Selecting an optimal CFIE: A multiple scattering approach

The electric field integral equation (EFIE) for TE scattering from a PEC object is

$$0 = E^{\text{inc}} - \iint_S \frac{\partial E}{\partial n_0} G dS_0 \quad (1)$$

The CFIE for the TE case is obtained by adding this to the MFIE for this problem using the complex constant α . This leads to

$$\frac{\partial E}{\partial n} = 2\alpha E^{\text{inc}} + 2 \frac{\partial E^{\text{inc}}}{\partial n} - 2 \iint_S \frac{\partial E^{\text{inc}}}{\partial n_0} K_\alpha dS_0 \quad (2)$$

where

$$K_{\alpha} \equiv \left(\alpha G + \frac{\partial G}{\partial n} \right) \quad (3)$$

Discretization of this equation is discussed in [Adams and Brown, 1998b]. The resulting matrix equation can be put in the form of (4.3.1-1). The corresponding MOMI series is of the same form as (4.3.1-6).

The CFIE (2) is guaranteed to have a unique solution whenever α is complex. This requirement provides significant freedom in the choice of α . We further constrain α by requiring that it provide optimal convergence properties for an arbitrary incident field. This corresponds to the value of α which minimizes the maximum modulus eigenvalue of P_M .

A physically intuitive way of determining this optimal choice is to minimize the contributions to the total field in (2) which are due to the integral term. Observe that if α is chosen such that $K_{\alpha} \equiv 0$ then no iteration is required to obtain the exact solution to the scattering problem. This is physically interpreted as the case of zero multiple scattering, an example of which occurs in the MFIE ($\alpha = 0$) formulation of scattering from an infinite PEC planar surface. In this case

$$\frac{\partial G}{\partial n} \equiv 0$$

and the integral term in (2) provides no contribution to the total surface current. This results for the flat surface scattering problem because the magnetic field radiated to an observation point on the surface by sources which are also on the surface has no tangential component. Thus, the MFIE for which MOMI was originally developed can be seen as the specialization of (2) to the rough surface case where α is selected such that $K_{\alpha} \equiv 0$ in the unperturbed geometry of the rough surface scattering problem.

If possible, the optimal choice for α would in general be

$$\alpha = -\frac{1}{G} \frac{\partial G}{\partial n} \quad (4)$$

as this would give $K_\alpha \equiv 0$ in all cases. Because this choice is not generally possible, we instead consider asymptotically determined estimates of α . In addition to providing optimal integral formulations, these asymptotic estimates provide information on how the optimal value of α depends on the size and shape of the scatterer. To simplify the following analysis, we consider only the case of circular cylinders.

For small cylinder radii ($k_a \ll 1$) the normal derivative of the electric field on the surface is approximately constant. Thus

$$\iint_S \frac{\partial E}{\partial n} K_\alpha dS_0 \approx \frac{\partial E}{\partial n} \iint_S K_\alpha dS_0 \quad (5)$$

and the contribution of the integral term to the total field in (2) is minimized by choosing

$$\alpha = -\frac{\langle \partial G / \partial n \rangle}{\langle G \rangle} \quad (6)$$

where $\langle \bullet \rangle$ denotes an average of the source point over the surface of the cylinder. Using the small argument forms of the zero and first order Hankel functions

$$H_0^{(2)}(z) \sim 1 - \frac{j2}{\pi} \left[\ln\left(\frac{z}{2}\right) + \gamma \right]$$

where $\gamma = 0.5772156649$, the Euler-Masheroni Constant

$$H_1^{(2)}(z) \sim \frac{j2}{\pi z}$$

substituting above gives

$$\begin{aligned} \alpha &\sim \frac{j2}{a} \left\langle \left(1 - \frac{j2\gamma}{\pi} \right) - \frac{j2}{\pi} \ln \left(ka \left| \sin\left(\frac{\phi - \phi_0}{2}\right) \right| \right) \right\rangle^{-1} \\ &\sim -\frac{1}{a} [j\pi + 2 \ln(ka) - \ln 2 + \gamma]^{-1} \end{aligned} \quad (7)$$

which is seen to be inversely related to the size of the cylinder.

For large cylinder radii ($k_a \gg 1$) the approximation (5) is not valid. Instead we attempt to minimize the contribution of the integral term appearing in (2) by choosing for α the average of (6), i.e.,

$$\alpha = - \left\langle \frac{\partial G / \partial n}{G} \right\rangle$$

Substituting the large argument forms of the zero and first order Hankel functions

$$H_0^{(2)}(z) \sim \sqrt{\frac{2}{\pi z}} e^{-j(z-\pi/4)}$$

$$H_1^{(2)}(z) \sim \sqrt{\frac{2}{\pi z}} e^{-j(z-3\pi/4)}$$

the simplified α becomes¹

$$\alpha \sim jk \left\langle \sin \left(\frac{\phi - \phi_0}{2} \right) \right\rangle = \frac{j2k}{\pi} = \frac{j4}{\lambda} \quad (8)$$

Unlike the small ka limit for which the optimal choice of α was found to vary with a , the value of α suggested by (8) is independent of the cylinder's size.

The physical significance of the value of α given by (8) is understood by observing that, on the surface of the cylinder in the TE problem

$$\frac{\partial E}{\partial n} \hat{y} = j\omega\mu\hat{n} \times \vec{H} = j\omega\mu H_{\tan} \hat{y}$$

Multiplying this equation through by α^{-1} and inserting the asymptotic value of α given by (8) prior to averaging, we have

¹ Although the averaging performed in (7) has been performed over all ϕ_0 , the contributions to the average from points near the observation point (for which the large argument approximations of the Hankel functions are not valid) are of order ka^{-1} when ka is large and do not significantly affect the result for α .

$$\frac{1}{\alpha} \frac{\partial E}{\partial n} = \frac{j\omega\mu}{jk|\sin([\phi - \phi_0]/2)|} = \tilde{\eta} H_{\tan}$$

where

$$\tilde{\eta} = \frac{\eta}{|\sin([\phi - \phi_0]/2)|}$$

and η is the free space impedance. Recalling that a plane wave propagating in the \hat{k} direction satisfies the relation

$$\eta \hat{k} \times \vec{H} = -\vec{E}$$

we see that the choice of α specified by (8) results from the fact that the field at an observation point excited by a distant source point is locally planar. $|\sin([\phi - \phi_0]/2)|$ in the denominator of $\tilde{\eta}$ (which is not present above) arises because the CFIE imposes a boundary condition on the tangential components of the total field. For TE incidence, the electric field is always tangential to the cylinder while the component of the magnetic field tangent to the cylinder varies with the location of the source point.

The optimality of the asymptotic estimates for α provided by (7) and (8) can be evaluated by calculating the eigenvalues of the resulting propagator matrices P_M . Figure 20 and Figure 21 show the magnitude of the largest eigenvalue of the MOMI propagator P_M (in dB) for the TE CFIE as a function of the complex constant α for various cylinder radii.

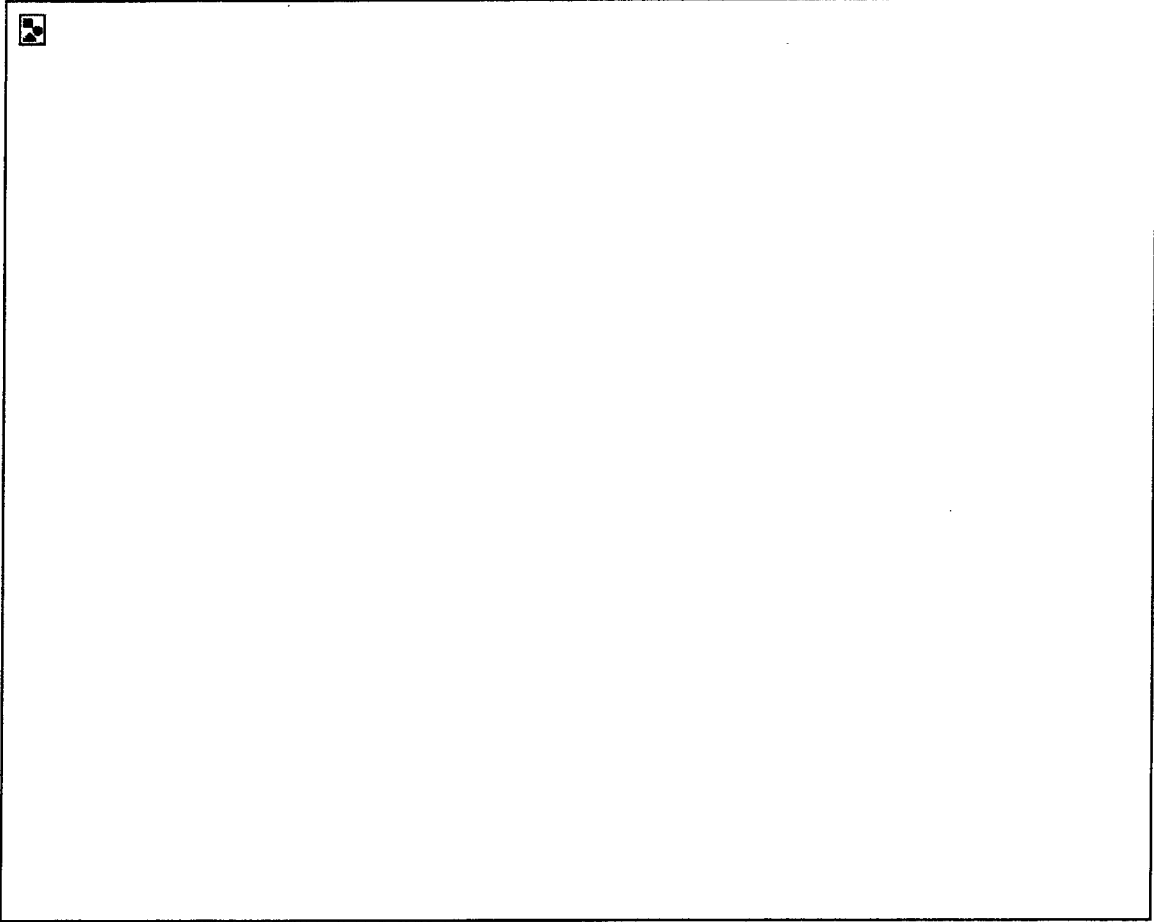


Figure 20: Contours of the largest eigenvalue of P_M (in dB) as a function of the complex constant α for circular cylinders

As anticipated by the above asymptotic analysis, for small radii the choice of α which yields the minimum maximum eigenvalue of P_M varies significantly with the radius of the cylinder. The estimate of α provided by (7) is good through $a = 0.05\lambda$. For the larger radii cases of $a = 1\lambda$ and $a = 5\lambda$ the value of α which yields the minimum maximum eigenvalue remains fairly constant at $\alpha \approx j4/\lambda$, which is in good agreement with the asymptotic value provided by (8).

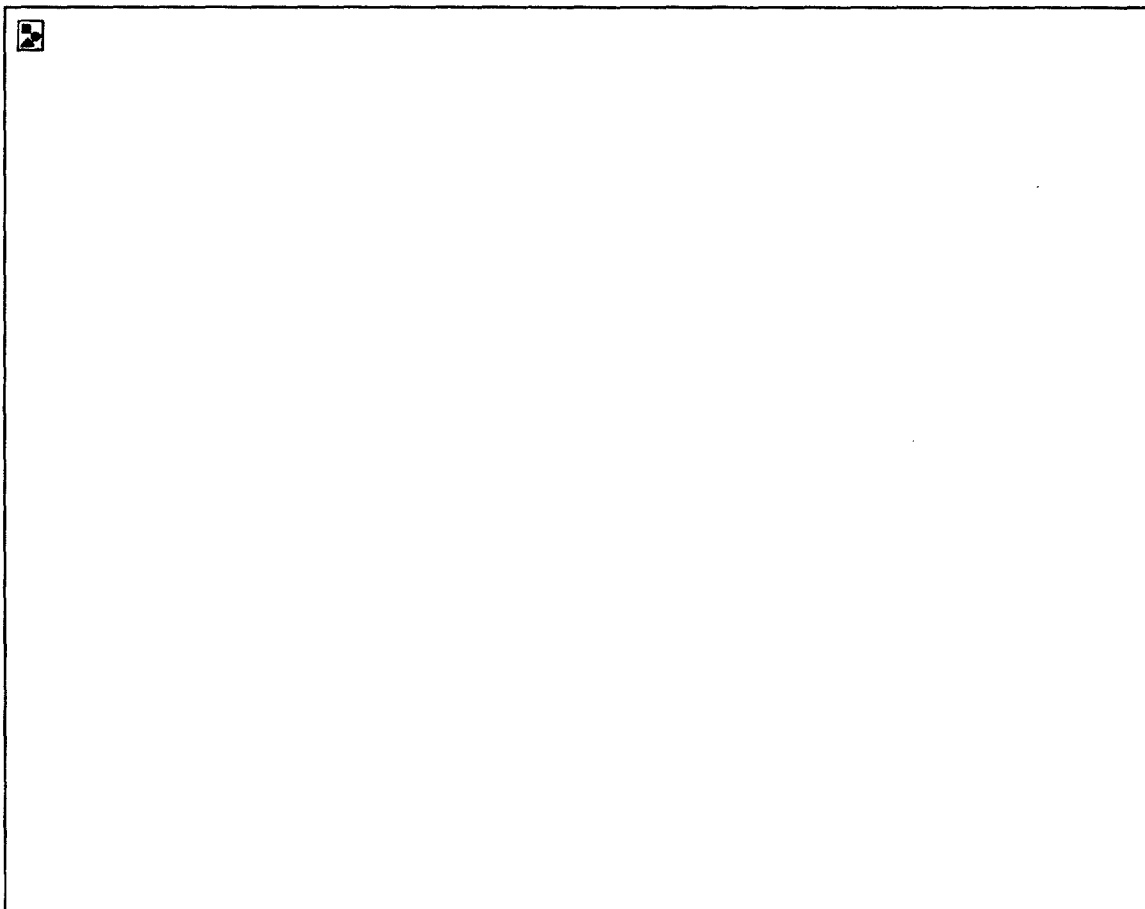


Figure 21: Contours of largest eigenvalue of P_M (in dB) as a function of the complex constant α for circular cylinders

From these figures we also notice that the minimum value of the maximum eigenvalue of P_M as a function of α increases as the cylinder radius increases from 0.01λ to 5λ . This occurs because for large cylinder radii we are able to minimize the integral term's contribution to (2) only by minimizing K_α in an average sense. In the small radii limit the approximation in (5) allowed us to determine the value of α by minimizing the contribution from the integral term itself.

Figure 22 and Figure 23 show the magnitude of the largest eigenvalue of P_M for TE scattering from elliptical cylinders having axial ratios of $a/b = 8$. For small radii we see that the optimal choice of α changes significantly with the size of the ellipse. The smallest maximum eigenvalue of P_M is larger for small elliptical cylinders than for small

circular cylinders due to the breakdown of approximation (5) as the axial ratio, a/b , increases.

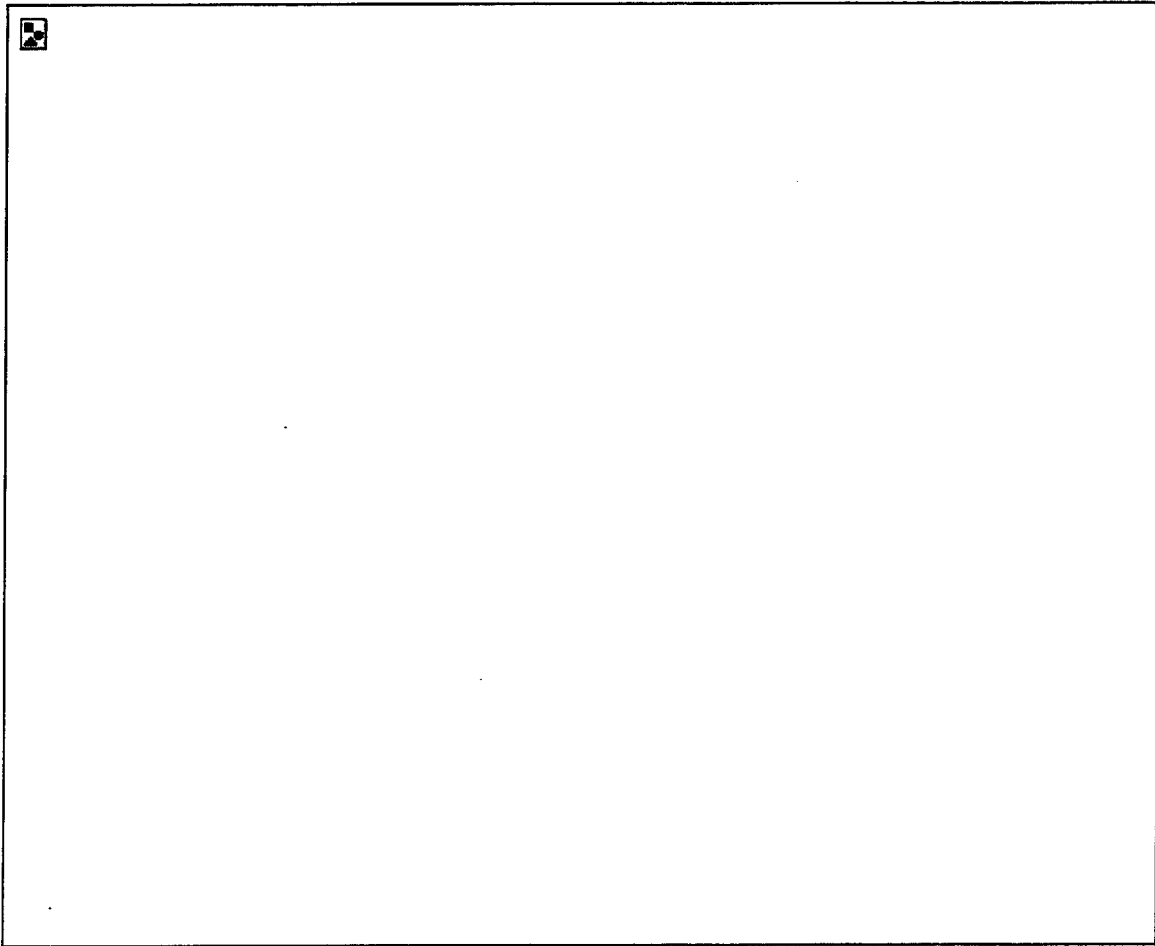


Figure 22: Contours of largest eigenvalues of P_M (in dB) as a function of the complex constant α for elliptical cylinders having $a/b = 8$

Also note that the optimal choice of α appears to bifurcate into two distinct regions in the complex α -plane for small value of a . This is due to the loss of rotational symmetry when ($a/b \neq 1$) and suggests that it may be more appropriate to choose α as a function of position in this case, i.e., $\alpha = \alpha(\rho)$. For larger values of a , the estimate in (8), derived for circular cylinders is seen to provide an excellent choice in the case of $a/b = 8$.

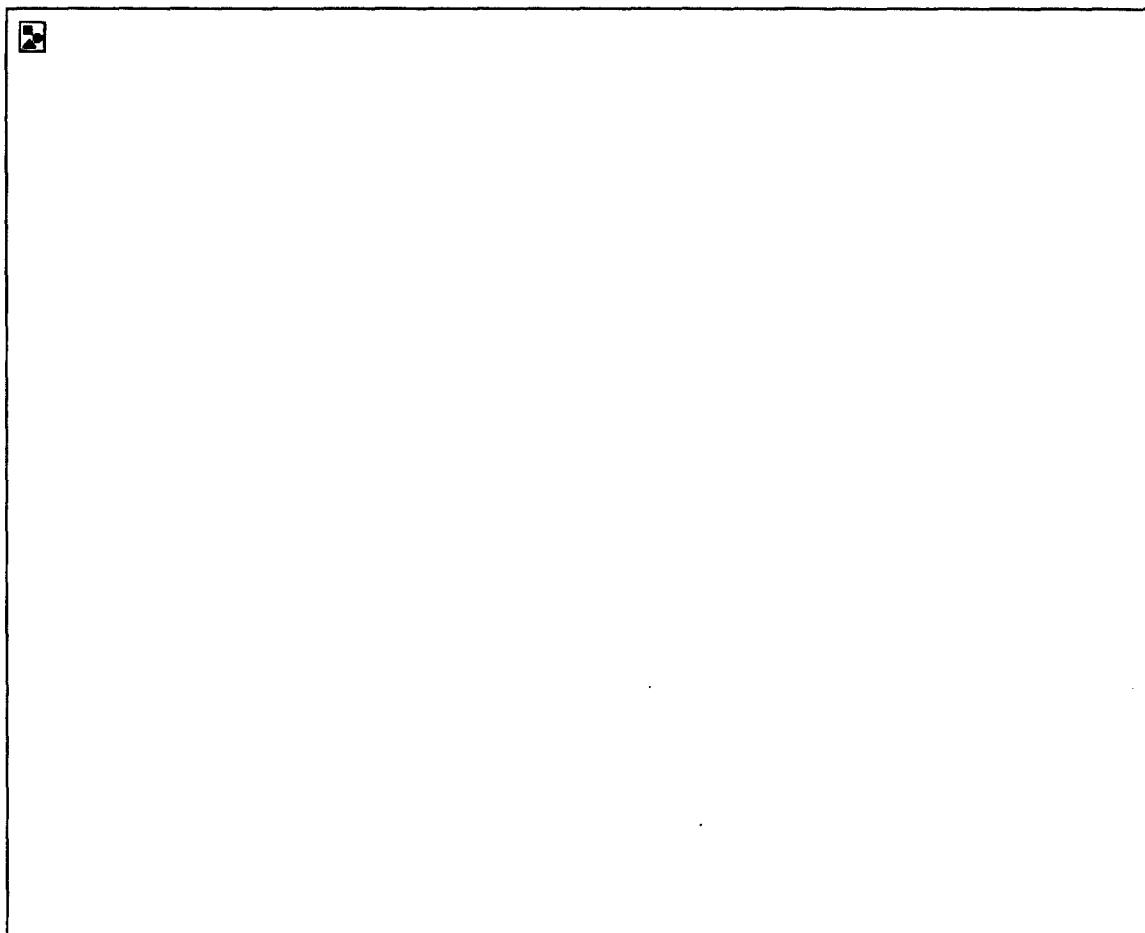


Figure 23: Contours of largest eigenvalues of P_M (in dB) as a function of the complex constant α for elliptical cylinders having $a/b = 8$

4.3.4 Example Results for TE Polarization

Simulations that follow demonstrate the investigations into an elliptical cylinder above a rough surface. A MOMI code was produced which includes unknowns on both an elliptical cylinder and a rough surface. The coupling parameter, α , on each surface was chosen to be the optimum for the observation point on the surface. Consequently, α is the asymptotic value described above on the cylinder and $\alpha = 0$ on the surface. The cylinder was chosen to be elliptical in order to resemble the foliage problem. All of the simulations which follow use TE Polarization and $\lambda/10$ sampling. Other parameters

depend upon the size of the scatterer and its separation from the surface; these include the following

- incident spot size = 20λ to 30λ
- surface length = 100λ to 200λ
- ellipse: major axis = 6λ to 10λ , minor axis = 2λ to 2.5λ
- height of the ellipse = 20λ to 60λ above the mean surface

These variables are identified in Figure 24.

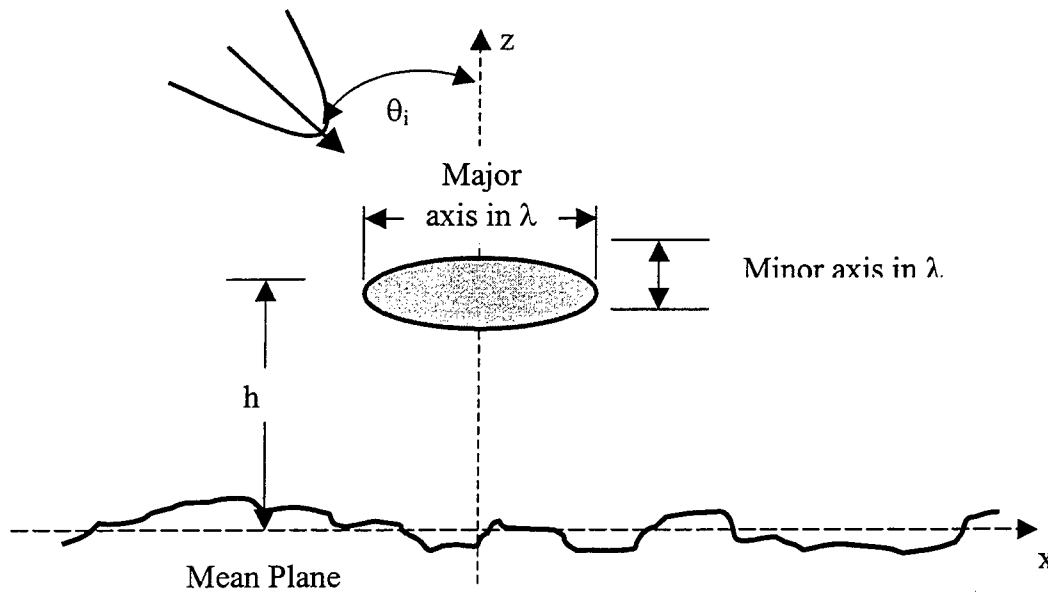


Figure 24: Scatterer over a Randomly Rough Surface

The total cross section of the elliptical cylinder and rough surface combination is plotted in the figures that follow. The far field form of the Hankel function normalizes this value:

$$\sqrt{\frac{2}{\pi k \rho}} e^{jk\rho - j\frac{\pi}{4}}$$

This solution which includes the full interaction will be referred to as the “exact solution”.

In addition to the total cross section of the full interaction problem, the total cross section of various stages of interaction are also included. First of all, the simple incoherent addition of scatter power is included; this case will be referred to as “incoherent addition” (IA) in the examples that follow. This curve will allow the assumptions of the impulse response method (no interaction) to be compared with a full interaction solution. Hence, it is equivalent to calculating the total cross of the ellipse and the surface in isolation and simply adding the resulting power, see Figure 25(a) and Figure 25(b), respectively. The source in this case is will be referred to as the “free-space incident field” and the resulting induced currents as the “incident currents.”

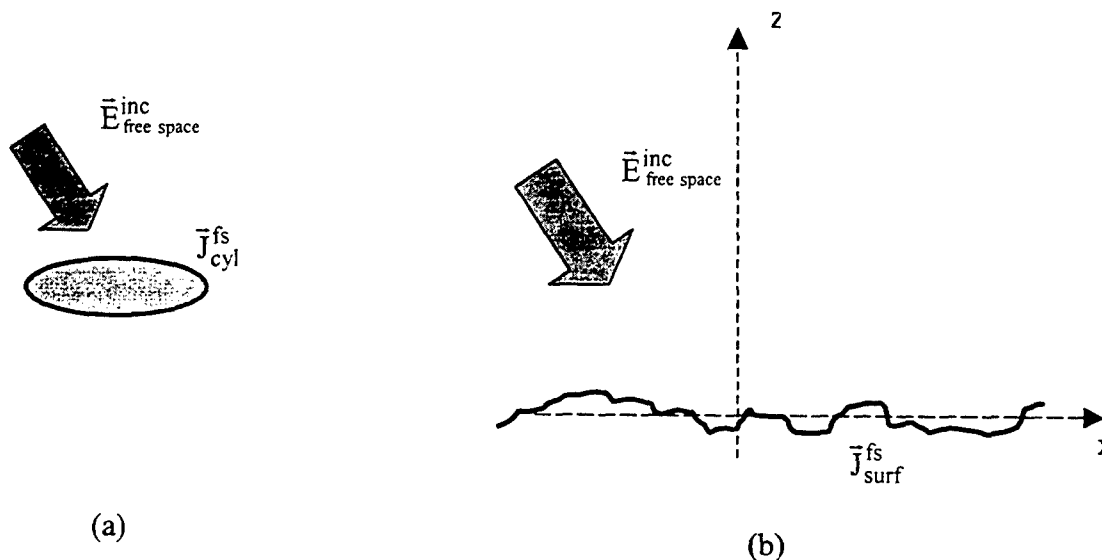


Figure 25: The Single Scatter Approximation: (a) Currents induced on the cylinder in isolation (b) Currents induced on the surface in isolation

The next step is the addition of the first order correction to both the current on the surface and the ellipse. Thus, after the current on the ellipse is calculated in isolation, its radiated field is added to the free-space field incident on the surface, see Figure 26(a). This results in the simple correction of the incident currents and the single scatter currents due to the ellipse. In turn, this corrected current on the surface is permitted to radiate and induce a correction to the current on the ellipse. This results in a double scatter event, yet is still a first order correction to the incident current on the ellipse, see Figure 26(b). Finally, the composite system with the first order corrected currents is allowed to radiate. This result is referred to as the double scatter result in the following example results.

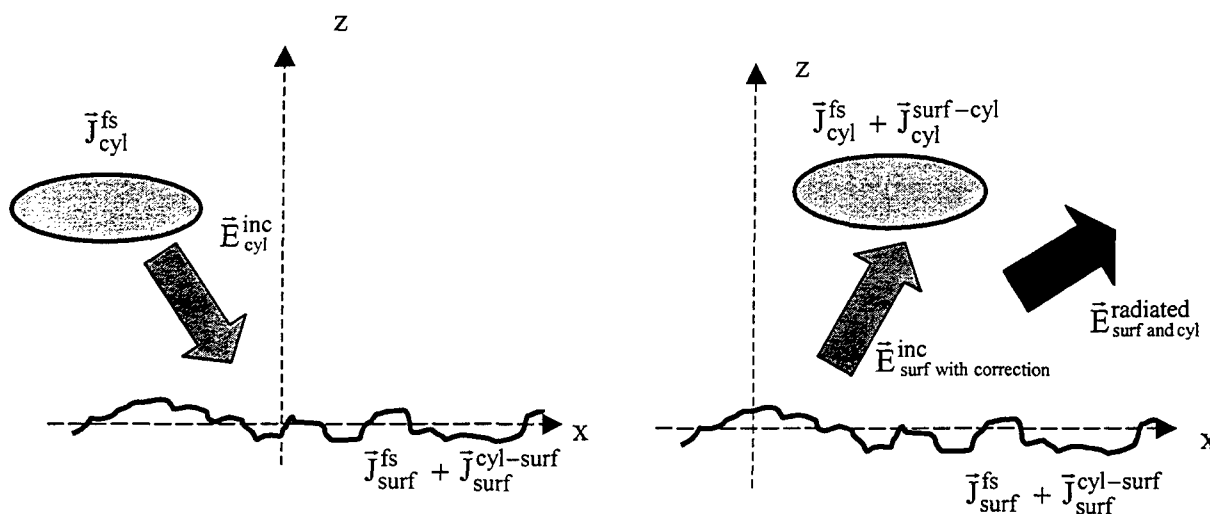


Figure 26: The Single Scatter Approximation: (a) Corrections to currents induced on the surface (b) Correction to Currents induced on the cylinder

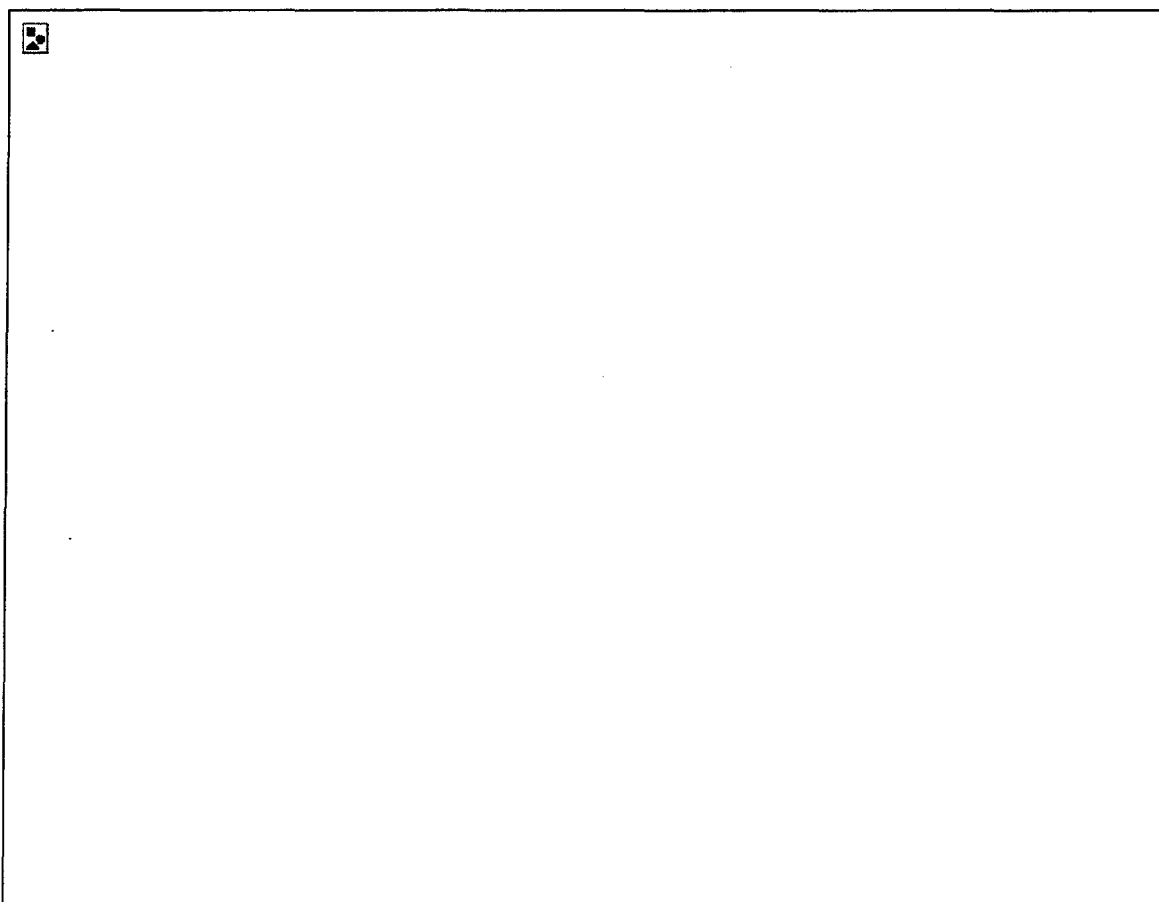


Figure 27: 6 wavelength ellipse, 60 wavelengths above a Gaussian rough surface

In Figure 27 through Figure 29, we see the effect of separation on the total cross section for the elliptical scatter/rough surface system by varying the separation between a 6 wavelength elliptical cylinder and the surface. In these figures, the exact total cross section can be compared with the incoherent addition of the surface and the scatterer (radiative transfer assumption) and the first order interaction between these parts. It is obvious from these figures that the double scatter approximation provides a better estimate of the total cross section of the composite system than the simple incoherent addition of the cross sections of the individual elements. It can also be seen that a larger the separation between the ellipse and the surface results in an increasingly better approximation by the incoherent addition with respect to the exact result. This fact has been verified by examining the cumulative root mean square error (cumulative with respect to the observation angles).

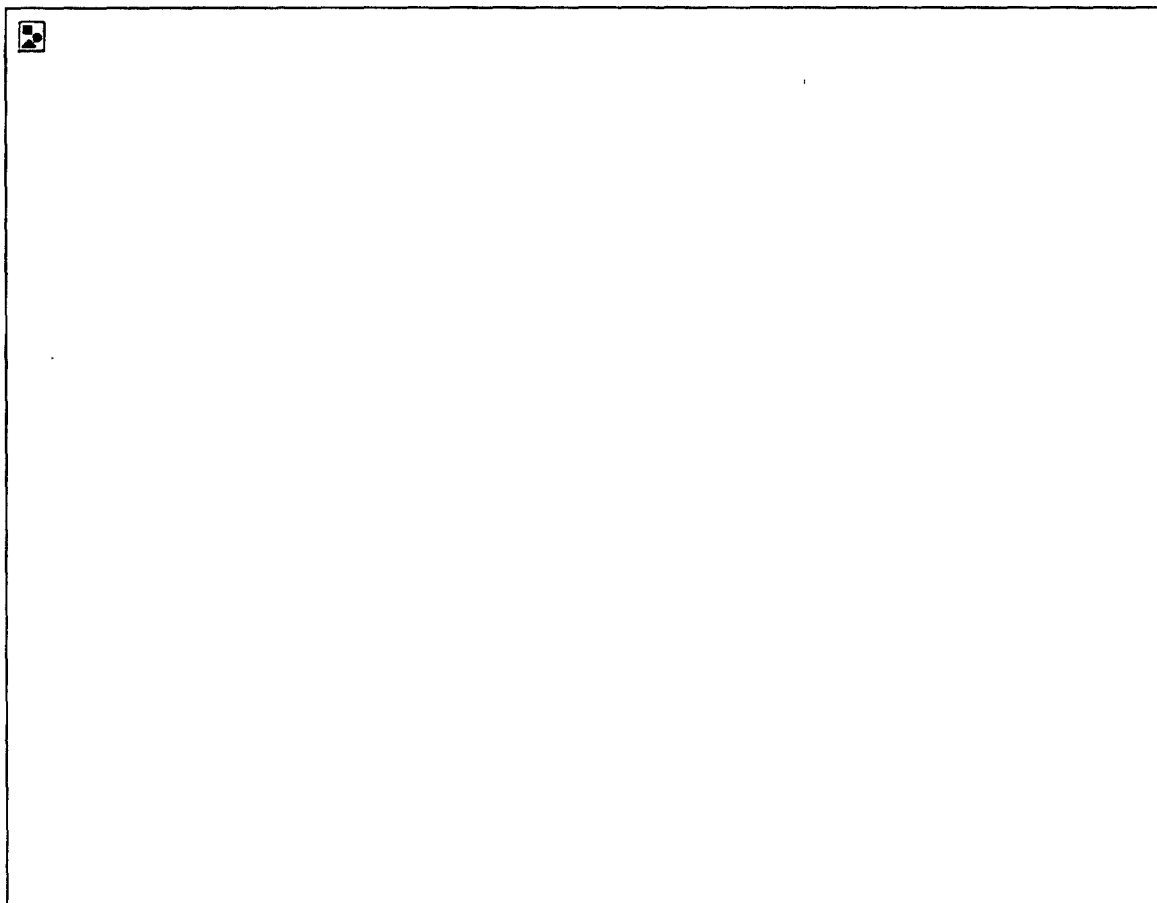


Figure 28: 6 wavelength ellipse, 20 wavelengths above a Gaussian rough surface

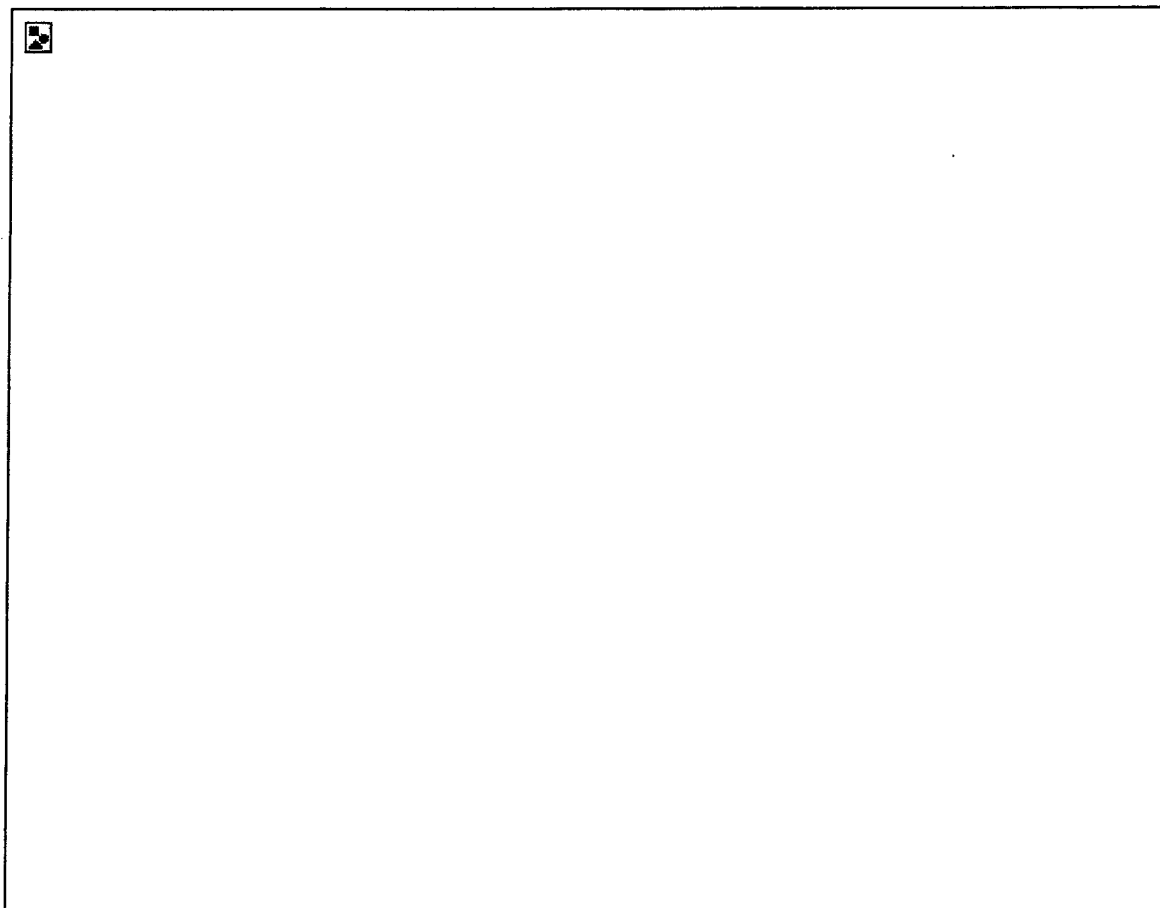


Figure 29: 6 wavelength ellipse, 5 wavelengths above a Gaussian rough surface

Since the agreement between the incoherent addition of the parts and the exact total cross section becomes closer, we can expect a threshold for the distance at which higher order interactions become significant. In addition to the separation, this threshold will most likely depend on the observation direction, the illumination direction and the orientation of the ellipse. Further numerical studies will be required to find these relationships. We can see that the calculation of the returned power for most foliage components will probably not require accounting the higher order interactions. However, a land-based target buried beneath the foliage, may require accounting for these interactions.

4.3.5 Conclusions and Future Efforts

The solution of the cylinder above a rough surface serves as a basis for comparison with the first order multiple scattering approach and ultimately the radiative transfer

approach. The results from these simulations will justify the requirements for higher order interactions in the foliage-surface scattering problem. As one would expect, we have seen an increased importance for the higher order interactions as the scatterer is moved closer to the surface or its size increases. This method is obviously inadequate as the number of scatterers increases or as the incidence angle increases since the problem becomes numerically intractable. The conclusions drawn from the example are not surprising and include the following

- the iterations required increased as the ratio of the body size to height above the surface decreased
- the interaction between the surface and the cylinder decreases as the separation is increased and incidence angle is decreased (measured from the vertical)
- the beamwidth must be significantly larger than the ellipse to see the effects of multiple scattering
- the single/double scatter corrections significantly improve the estimate for power returned relative to the simple power addition (at least for small roughness)

In addition, we have seen slower convergence in our technique as the scatterer is moved closer to the surface. Consequently, a stabilized bi-conjugate gradient solution (BiCSTAB) in combination with the MOMI has been implemented as an aide for the convergence of the problem. We note that the application of the BiCSTAB routine to the MOM equations in one particular example (16λ cylinder major axis, 3λ above the rough surface) did not converge within the number of iterations allotted. Likewise, the straight MOMI solution required 30 iterations. However, when the BiCSTAB routine was applied to the MOM equations *after* the MOMI preconditioner was applied, the ellipse and rough surface system required only 10 MOMI/BiCSTAB iterations.

Two final notes: since these simulations occur with monochromatic waves and the interest in this work involves pulsed energy, the pulse chosen for comparison will be slowly varying and of long duration. Primarily, we are interested in the importance of the interactions, not the solution; consequently, until a time-dependent code is introduced, we will assume that the importance of the interactions in the pulsed energy problem is similar to that in the monochromatic problem. In addition, one further assumption of the

impulse response model requires our attention; the assumption of no wide-angle scattering. This may be significant for all components of foliage and ground based targets.

4.4 Approximate Analytical Solution for the Moments of a Single Scatterer above a Rough Surface

If it is found that the scatterer above the rough surface includes important interactions that are not included in the modified first order multiple scattering solution, this solution must be refined. In addition, if the return from a strong scattering object, such as a vehicle, under the vegetation is desired, then the coherent return may be desired. The exact solution for the problem of multiple scatterers above a rough surface will become numerically intractable as the number of scatterers increase. *Consequently, alternative methods must be used or the exact solution must be simplified.* As we have seen in the previous sections, the exact solution for a single scatterer above the rough surface in combination with the first order multiple scattering will produce some insight into the validity of the radiative transfer result. An alternate approach that simplifies the exact results, yet unlike the first order multiple scattering result, maintains the coherent response, begins with the exact integral equations and incorporates some reasonable assumptions. Like the first order multiple scattering response, we begin with a single scatterer over a rough surface and propose an extension to N scatterers above a rough surface.

We start with coupled integral equations: one representing the current on the rough surface and the other representing that on the scatterer. From equivalence, the MFIE for the current on the scatterer in the presence of the rough surface can be written

$$\begin{aligned} \vec{J}_{s1}(\vec{r}_1) = & 2\hat{n}_1 \times \vec{H}^i(\vec{r}_1) + 2\hat{n}_1 \times \iint_{\substack{\text{Scatterer} \\ \text{Surface}}} \vec{J}_{s1}(\vec{r}_1') \times \nabla' G(\vec{r}_1, \vec{r}_1') dS_1 \\ & + 2\hat{n}_1 \times \iint_{\substack{\text{Rough} \\ \text{Surface}}} \vec{J}_{s2}(\vec{r}_2') \times \nabla' G(\vec{r}_1, \vec{r}_2') dS_2 \end{aligned} \quad (1)$$

where the subscripts 1 and 2 will indicate points or currents on the scatterer and the rough surface, respectively. The current is evaluated at the observation point, which is on the scatterer. Note the presence of the term, the last term. From equivalence, the MFIE for the current on the rough surface in the presence of the scatterer can be written

$$\begin{aligned}
\bar{J}_{s2}(\bar{r}_2) = & 2\hat{n}_2 \times \bar{H}^i(\bar{r}_2) + 2\hat{n}_2 \times \iint_{\substack{\text{Scatterer} \\ \text{Surface}}} \bar{J}_{s1}(\bar{r}_1') \times \nabla' G(\bar{r}_2, \bar{r}_1') dS_1 \\
& + 2\hat{n}_2 \times \iint_{\substack{\text{Rough} \\ \text{Surface}}} \bar{J}_{s2}(\bar{r}_2') \times \nabla' G(\bar{r}_2, \bar{r}_2') dS_2
\end{aligned} \tag{2}$$

The current is evaluated at the observation point, which is on the scatterer. Note the presence of the coupling, the second term. The geometric quantities in these two equations are defined in Figure 30.

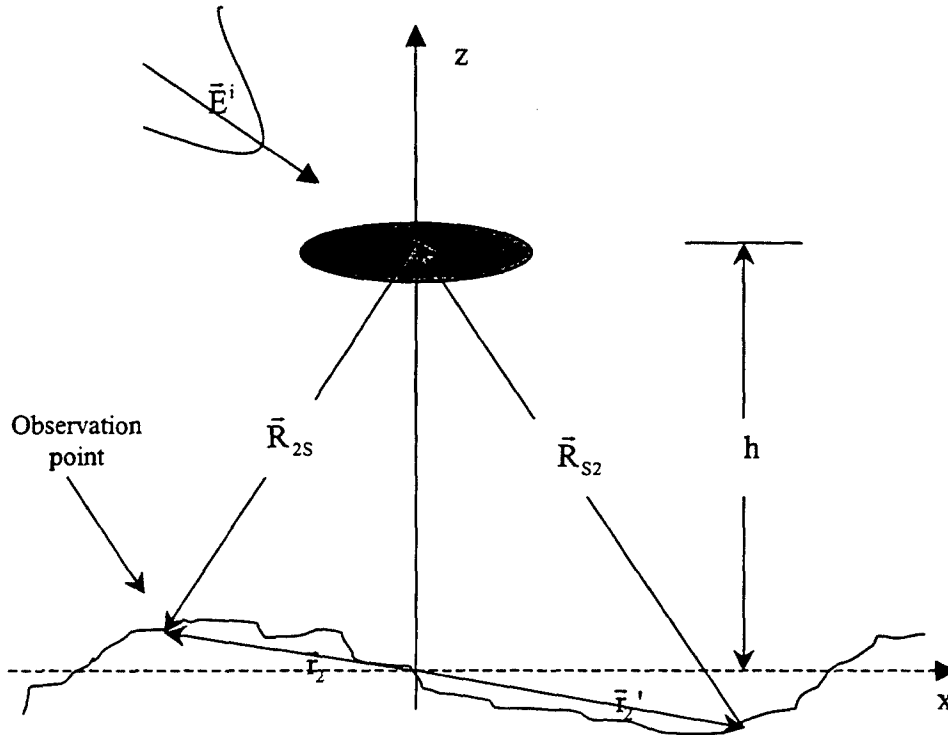


Figure 30: Geometry for the Reduced Integral Equation Approach

4.4.1 The Reduced Integral Representation

The overall goal is to simplify the solution for a single scatterer over a rough surface. Since the scatterer is assumed to be small with respect to the distance to the surface, the far-field form of the Green's function will be used for interactions involving the scatterer as the source and the surface as the observation location. In addition, when

the object is modeled as a smooth ellipse or a disc, the Physical Optics (PO) approximation will be used to estimate the induced currents on the scatterer due to the incident field. In all remaining sections, these two simplifications shall be considered accurate. Starting with the coupled integral equations and substituting into the integrands of (1) and (2) in the previous section, we find for the scatterer

$$\bar{J}_{s1}(\bar{r}_1) = 2\hat{n}_1 \times \bar{H}^i(\bar{r}_1) + 2\hat{n}_1 \times \iint_{\substack{\text{Rough} \\ \text{Surface}}} \bar{J}_{s2}(\bar{r}_2') \times \nabla' G(\bar{r}_1, \bar{r}_2') dS_2 \quad (1)$$

In this formulation, the integral equation for the current on the scatterer still involves two unknowns. For the currents on the rough surface, we find the following equation

$$\begin{aligned} \bar{J}_{s2}(\bar{r}_2) = & 2\hat{n}_2 \times \bar{H}^i(\bar{r}_2) \\ & + 2\hat{n}_2 \times \iint_{\substack{\text{Scatterer} \\ \text{Surface}}} \left[2\hat{n}_1 \times \bar{H}^i(\bar{r}_1) + 2\hat{n}_1 \times \iint_{\substack{\text{Rough} \\ \text{Surface}}} \bar{J}_{s2}(\bar{r}_2') \times \nabla' G(\bar{r}_1, \bar{r}_2') dS_2 \right] \times \nabla' G_{ff}(\bar{r}_2, \bar{r}_1') dS_1 \\ & + 2\hat{n}_2 \times \iint_{\substack{\text{Rough} \\ \text{Surface}}} \bar{J}_{s2}(\bar{r}_2') \times \nabla' G(\bar{r}_2, \bar{r}_2') dS_2 \end{aligned} \quad (2)$$

where $G_{ff}(\bar{r}, \bar{r}')$ is the far-field form of the free space Greens Function. Those vales with a subscripted "1" are in reference to the scatterer and those with a "2" are with respect to the surface. In addition, the primed coordinates reference the sources and unprimed reference the observation points. This integral equation consists of three terms

1. The first term is the well-known Kirchhoff term
2. The second term couples the currents of the surface to that of the scatterer
3. The third term is the familiar multiple scattering term for the surface to surface interactions

Notice that the PO current on the scatterer is known; consequently, the only unknown in the integral equation for the surface current is the surface current itself. Moving the normal unit vectors inside the integrals and using the vector identity

$$\bar{A} \times \bar{B} \times \bar{C} = \bar{B}(\bar{A} \cdot \bar{C}) - \bar{C}(\bar{A} \cdot \bar{B}) \quad (3)$$

Expanding the gradient of the Greens Function:

$$\nabla' G(\bar{r}, \bar{r}') = \left[\frac{1}{|\bar{r} - \bar{r}'|} + jk \right] G(\bar{r}, \bar{r}') \frac{(\bar{r} - \bar{r}')}{|\bar{r} - \bar{r}'|} = \left[\frac{1}{|\bar{r} - \bar{r}'|} + jk \right] G(\bar{r}, \bar{r}') \hat{k}_s \quad (4)$$

where, following the notation of [Ishimaru, 1978], the direction from the source point to the observation point is given by

$$\hat{k}_s \equiv \frac{(\bar{r} - \bar{r}')}{|\bar{r} - \bar{r}'|} = \text{the scattering direction}$$

Employing the far-field approximation, the Greens function and its gradient become

$$G(\bar{r}, \bar{r}') \cong \frac{e^{-jkR}}{4\pi R} e^{-j\hat{k}_s \cdot \bar{r}'} \equiv G_{ff}(\bar{r}, \bar{r}') \quad (5)$$

$$\nabla' G(\bar{r}, \bar{r}') \cong jk \frac{e^{-jkR}}{4\pi R} e^{-j\hat{k}_s \cdot \bar{r}'} \hat{k}_s = jk G(\bar{r}, \bar{r}') \hat{k}_s$$

where $\bar{R} \equiv \bar{r} - \bar{r}'$. Further reduction of integral equations is accomplished by assuming the scatterer has a definite geometrical shape (disc, etc.). In this case the backscatter and forward scatter from known scatterer geometry may have an analytical result, further simplifying the integral equations.

4.4.2 Reduction for a Circular Disk (3-D) Scatterer above a Rough Surface

In 3-D, the integral equations were specialized to a circular disc with random tilt and height above a randomly rough surface and in 2-D, the integral equations were specialized to a strip with random tilt above a corrugated surface. Only the results of these derivations will be given in this report. These results should include more interaction terms with the surface than the first order multiple scattering theory but with less computational demand than the exact solution. For a flat disc, horizontally suspended over a rough surface, the current on the rough surface is

$$\begin{aligned}
\bar{J}_s(\bar{r}_2) = & 2\hat{n}_2 \times \bar{H}_i(\bar{r}_2) + jk \frac{\exp\{-jkR_{2s}\}}{2\pi R_{2s}} \exp\{-jk\hat{R}_{2s} \cdot \hat{z}h\} \\
& \cdot \iint_{S_1} \left[(-\hat{n}_2 \cdot \hat{R}_{2s}) (\hat{z} \times \bar{H}_i(\bar{r}_1')) + \hat{R}_{2s} (\hat{n}_2 \cdot [\hat{z} \times \bar{H}_i(\bar{r}_1')]) \right] \exp\{-jk\hat{R}_{2s} \cdot \bar{r}_1'\} dS_1' \\
& + 2 \iint_{S_2} \left\{ \bar{J}_s(\bar{r}_2') (\hat{n}_2 \cdot \hat{R}_{2s'}) - (\hat{n}_2 \cdot \bar{J}_s(\bar{r}_2')) \hat{R}_{2s'} \right\} |\nabla' G(\bar{r}_2, \bar{r}_2')| dS_2' \\
& + \frac{\exp\{-jkR_{2s}\}}{4\pi^2 R_{2s}} kA \exp\left\{ \frac{-jkh^2}{R_{2s}} \right\} J_1(kA) \\
& \cdot \iint_{S_2} \left\{ \left[\bar{J}_s(\bar{r}_2') (\hat{n}_2 \cdot \hat{R}_{2s}) - (\hat{n}_2 \cdot \bar{J}_s(\bar{r}_2')) \hat{R}_{2s} \right] \frac{h}{R_{S_2}} - \left[(\hat{n}_2 \cdot \hat{R}_{2s}) \hat{R}_{S_2} - (\hat{n}_2 \cdot \hat{R}_{S_2}) \hat{R}_{2s} \right] (\hat{z} \cdot \bar{J}_s(\bar{r}_2')) \right\} \\
& \frac{\exp\{-jkR_{S_2}\}}{4\pi^2 R_{S_2}} \exp\left\{ \frac{-jkh^2}{R_{S_2}} \right\} dS_2'
\end{aligned} \tag{1}$$

where the Bessel Function of the first kind, $J_1(x)$, has arisen due to the circular disk and A is the area of one face of the disk. It has been assumed that the disk is very thin. The first term is the Kirchhoff current on the surface. The second term, the first integral term, is an additional Kirchhoff current term due to the incident field from the Kirchhoff current on the disk: the Kirchhoff current on the disk radiates to the surface. Shadowing must be accounted for in the use of this term: the Physical optics current on the underside of the disk, due to the incident field will typically be zero. The third term is the surface in isolation. Finally, the fourth term is a multiple interaction result: the current on the surface radiates to the disk and is re-radiated to the surface again ... ad nauseum. Note that this integral equation has only one unknown: the current on the surface.

The integral equation for the disk simply involves Kirchhoff current and the current due to the surface radiating to the disk. Note that this equation is fully coupled to the solution for the current on the surface

$$\bar{J}_1(\bar{r}_1) = 2\hat{z} \times \bar{H}_i(\bar{r}_1) + 2 \iint_{S_2} \left\{ \bar{J}_{s_2}(\bar{r}_2') \left[\left(\frac{1}{|\bar{r}_1 - \bar{r}_2'|} + jk \right) \frac{h}{|\bar{r}_1 - \bar{r}_2'|} G(\bar{r}_1, \bar{r}_2') \right] + \nabla' G(\bar{r}_1, \bar{r}_2') (\hat{z} \cdot \bar{J}_{s_2}(\bar{r}_2')) \right\} dS_2' \quad (2)$$

If the surface is gently undulating, the z-directed currents will be nearly zero, hence, the integral equations for the currents become

$$\begin{aligned} \bar{J}_s(\bar{r}_2) = & 2\hat{n}_2 \times \bar{H}_i(\bar{r}_2) + jk \frac{\exp\{-jkR_{2s}\}}{2\pi R_{2s}} \exp\{-jk\hat{R}_{2s} \cdot \hat{z}h\} \\ & \cdot \iint_{S_1} \left\{ (-\hat{n}_2 \cdot \hat{R}_{2s}) (\hat{z} \times \bar{H}_i(\bar{r}_1')) + \hat{R}_{2s} (\hat{n}_2 \cdot [\hat{z} \times \bar{H}_i(\bar{r}_1')]) \right\} \exp\{-jk\hat{R}_{2s} \cdot \bar{r}_1'\} dS_1' \\ & + 2 \iint_{S_2} \left\{ \bar{J}_s(\bar{r}_2') (\hat{n}_2 \cdot \hat{R}_{22'}) - (\hat{n}_2 \cdot \bar{J}_s(\bar{r}_2')) \hat{R}_{22'} \right\} |\nabla' G(\bar{r}_2, \bar{r}_2')| dS_2' \\ & + \frac{\exp\{-jkR_{2s}\}}{4\pi^2 R_{2s}} kA \exp\left\{ \frac{-jkh^2}{R_{2s}} \right\} J_1(kA) \\ & \cdot \iint_{S_2} \left\{ [\bar{J}_s(\bar{r}_2') (\hat{n}_2 \cdot \hat{R}_{2s}) - (\hat{n}_2 \cdot \bar{J}_s(\bar{r}_2')) \hat{R}_{2s}] \frac{h}{R_{s2}} \right\} \frac{\exp\{-jkR_{s2}\}}{4\pi^2 R_{s2}} \exp\left\{ \frac{-jkh^2}{R_{s2}} \right\} dS_2' \end{aligned} \quad (3)$$

and

$$\bar{J}_1(\bar{r}_1) = 2\hat{z} \times \bar{H}_i(\bar{r}_1) + 2 \iint_{S_2} \bar{J}_{s_2}(\bar{r}_2') \left[\left(\frac{1}{|\bar{r}_1 - \bar{r}_2'|} + jk \right) \frac{h}{|\bar{r}_1 - \bar{r}_2'|} G(\bar{r}_1, \bar{r}_2') \right] dS_2' \quad (4)$$

A more complex result is available for a disk with arbitrary tilt and in 2-D, a strip with arbitrary tilt.

4.4.3 Conclusions and Future Work

This section has started with the exact coupled integral equations for a rough surface in the presence of a single scatterer and reduced these using the far-field form of the Green's function for the scattered field due to the scatterer and the physical optics solution to the scatterer's current. Furthermore, we have isolated an approximate integral equation for the surface scattering in the presence of the disk. This integral equation only involves one unknown, the current on the rough surface.

In addition we have simplified the expression for a scatterer that is a circular disk. In addition, the term that represents the multiple interactions between the scatterer and the surface has been isolated and should be evaluated relative to the surface in isolation. This investigation will yield an analytical solution as to the validity of the single interaction assumption for the radiative transfer result. The next step in this process is to numerically implement the above integral equations. These results may then be compared with those obtained with MOM/MOMI. Concurrently, the average results will be attempted analytically for a random height and then the random orientation. These results should be implemented numerically.

In the extension to N scatterers above a rough surface, no interaction between scatterers will be accommodated; the result will include interaction with the surface, like the first order multiple scattering result. Unlike the first order multiple scattering result discussed earlier, these results will include a more comprehensive treatment of the interaction with the surface in addition to the preservation of the coherent field. Numerical solutions and comparison with MOM results for two to three scatterers can be performed in an effort to assess the mutual interactions among the scatterers themselves (ignored by the presented single scatter theory). An attempt to derive analytic expressions for the field moments from these equations will be made, including the mutual coherence functions.

In addition to a volume return component, this reduced integral equation formulation result will produce the most comprehensive treatment of the scattered field from a collection of scatterers above a rough surface. We note that many useful methods already

exist which predict both the coherent and incoherent responses from a volume of discrete scatterers that may be combined with these results in order to produce a comprehensive model. These include the DWBA [Lang, 1981], Cumulative Forward Scatter, Single Backscatter theory [deWolf ,1971], its extension to pulse propagation [Ishimaru,1980] and the related spectral approach [Rino, 1988].

5 Conclusions and Future Action

In predicting the radar return from vegetation, a number of approaches have been developed. Typically, the overly cumbersome radiative transfer seems to be very popular. Exceptions to this trend have been found in the works of [Schwering, 1985], and [Brown and Adams, 1998a]. Schwering has used a simple scattering function to represent the scattering properties of all components of the volume. A notable wave approach to this problem is that of Lang [Lang, 1981] who has used the Distorted Wave Born Approximation. In this study we have formulated a simple model that is numerically efficient and depends on the empirical identification of effective parameters. However, there are a number of verification studies that must be performed and several different levels of verification have been outlined in this report. The major thrust of these verifications is to identify the necessary level of approximation for the foliage-surface interaction.

The Impulse Response (Convolutional) model allows a superposition of surface and volume responses. Its numerical implementation is via the Fast Fourier transform, FFT, which allows a fast numerical solution. This approach, although originally derived from the radar equation and then by the radiative transfer equations, has been shown to be equivalent to the "first order multiple scattering theory." This equivalence has been derived under the assumptions of narrow-band and narrow-beamwidth with a limited scattering pattern. From this equivalence, we have proposed a method using the first order multiple scattering to verify the single passage assumption for foliage-surface interaction that is inherent in the radiative transfer approach.

The future direction of this work will involve thoroughly investigating the assumptions of the impulse responses and consequently, establishing the range of their validity; these investigations may in turn expand the applicability of the model. Generalizing the model to include lower frequencies, larger beamwidths, etc. will require an investigation into the range of validity of each of the above limitations and may involve generalization of the model. Some of these investigations and extensions have been performed. The most straightforward model improvement will be the addition of

polarization. The use of the Stokes vector will allow for polarization dependence in the model. Depolarization will enter naturally through the Stokes vector definition, existing models, and measured data. After accounting for the polarization effects, the incident beam waveform can be given a pulse shape. This pulse will be constructed using Fourier analysis in order to recreate pulse scattering with an incident beam using a full radiative transfer approach. This pulsed waveform result is then directly comparable to our impulse response model. For large bandwidth signal, each Fourier component of the pulse may be treated separately in radiative transfer theory; hence, the scattering characteristic of the scatterers can be changed with frequency. When derived from the single (or higher order multiple) scattering approach, the impulse response model will require a more general form for the two frequency mutual coherence function. Investigations into the other approximations will require investigations into the effects of wide-angle and multiple scattering.

The effects of multiple scattering may be established by inserting the next higher-order scattering correction in our model. Through these corrections, we may estimate the system parameters or foliage and surface conditions that will either cause the model to fail completely, e.g. become grossly invalid, or give rise to significant changes in the expected effective parameters in the model. Beginning with the development of the impulse response method using multiple scatter theory, we have developed a rigorous formalism that will simplify to the impulse response model under the given assumptions. Under this model, higher order scattering corrections may be added in each of the interaction regions: foliage-foliage, surface-surface or foliage-surface. For example, known numerical techniques may be applied to correct for multiple scattering among surface elements; the applicability of the facet model used by the impulse response model may be directly compared with these numerical techniques. The multiple interactions and the effect of wide-angle scattering between the foliage constituents and the surface can also be implemented numerically but this creates a numerically intractable problem as the number of foliage components grows. Hence, we have looked to reduce this problem and only characterize the important interactions between the foliage and the surface.

Although the mutual interactions between the scatters comprising the vegetation are neglected in our first order model, some interaction between each of these scatterers and the surface may be non-negligible. In the first order model, the backscattered power density from the rough surface and the foliage volume separate into two distinct components. Consequently, by construction, this model assumes that there is no interaction between the surface and the volume scattering elements other than the exponential decay of the surface scattered power through the volume. In the course of our research, we have developed an exact integral equation approach that simulates the interaction of a one-dimensional, statistically rough surface in the presence of an elliptical cylinder at some distance above the surface. This effort is necessary in order to compare the first order multiple scattering result with a result with known accuracy. These results provide a basis of comparison for the impulse response.

Implemented via the MOMI method of solution to the MOM problem, this numerical model permits the specification of each order of interaction that is present in the result, e.g. the first and second order interactions, between the scatterer and the surface. To accommodate strong interactions between surface and foliage, several advanced numerical techniques have been (will be) implemented, e.g. the method of multiple ordered interactions, the stabilized bi-conjugate gradient algorithm and the fast multipole method. The results presented are restricted to the TE incidence but they have also been extended to the construction of the MOMI model for TM polarization for an elliptical cylinder over a rough surface. We have found that a simple incoherent addition of the scattered power will be accurate for most foliage components; this will depend on the ratio of the scatterer's largest dimension to its displacement above the rough surface. A large object such as a target embedded within the foliage, on the other hand, will require multiple scattering and wide-angle corrections for an accurate scattering prediction. It has been observed that the interaction between the surface and a nearby object can be significant, particularly when the scatterer is closer to the surface and as incidence angle is further removed from nadir.

If these interactions between surface and scatterer have a significant effect on the returned power waveform, we may resort to the full first order multiple scatter theory,

which includes wide-angle scattering. This theory will more fully account for foliage-surface interaction and extend the impulse response model. Although this will add complexity to the model, some advantages of the convolutional approach may be retained. A plan has been presented to extend the first order multiple scattering solution for foliage and foliage-surface interaction to both broadbeam and broadband cases: this is not possible in the radiative transfer approach as presented. By including double scattering events (scattering between the foliage and every surface component), the assumption of pure forward scatter and backscatter will be abandoned. Through this extension of the impulse response method each component of the foliage will interact with every surface element (facet) rather than a single surface element. This numerical model may also be used to establish the multiple scattering significance for a target embedded within our vegetated surface. Such a target may be found through a comparison of the return waveform from the vegetated rough surface with that of the vegetated rough surface with an embedded target. We may then tailor our system parameters (pulse length, beamwidth, etc.) to more readily identify its presence.

The full, first-order multiple scatter theory will also test the validity of the narrow beamwidth assumption in the foliage-surface interaction. However, for the foliage-foliage interaction another more complete test will involve a solution of the unsimplified radiative transfer equation. This solution will test the effects of higher orders of multiple interactions on the received waveform. This assumption presumes that the returned power is confined to a small region around the transmitting beam axis. Beam broadening through wide-angle scattering and multiple scattering in a tenuous media can be neglected if the receiver and transmitter beamwidths are narrow since multiple scattering effects and wide-angle scattering are negligible within a small illuminated volume. Through comparison with the impulse response model, a range of validity for the narrow beam assumption will be established. Although the steady state solution of the radiative transfer equations for a *plane wave* incident to a random media is widely available in literature, this solution must be extended to account for an actual antenna pattern. To this end, we have constructed a radiative transfer solution for beam incidence and are in the

process of evaluating the role of multiple scattering, wide-angle scattering and beam broadening.

In addition to the impulse response approach, a second analytical approach has been formulated which begins with the exact integral equations. We hope to find an analytical, or at least computationally efficient, solution to both the mean and second order, time dependent power density for the single scatterer above a rough surface. Like the impulse response approach, the incoherent results for the superposition of N scatterers will provide a new look at the single scattering theory for an ensemble of particles above a rough surface and should serve as a check against the impulse response result. However, unlike the impulse response method, this approach will provide the coherent field returned from the volume and the rough surface and it will include higher orders of multiple scattering. This result should be directly comparable to the Distorted Wave Born Result (DWBA), see [Lang, 1981]. Hence, one additional task includes constructing a DWBA model including a rough surface, based on Lang's work and in order to compare with this reduced integral equation result.

References

Cherland, E., Fitzpatrick, R. 1999. Psychotic Side Effects of Psychostimulants: A 5-Year Review. *Canadian Journal of Psychiatry*, 44, 811-813.

Farid, N. A., Bergstrom, R. F., Ziege E., A., Parli, C. J., Lemberger, L. 1985. Single-Dose and Steady-State Pharmacokinetics of Tomoxetine in Normal Subjects. *Journal of Clinical Pharmacology*. 25(4): 296-301.

Goodman, A., G., Rall, T. W., Nies, A. S., Taylor, P. 1991. *The Pharmacological Basis of Therapeutics*, 8th edition. New York. Pergamon Press.

Hoffmann, Heinrich. 1844. *Struwwelpeter*: In English Translation. Dover Publications. 1995.

Jandowsky, David S., M.D., Khaled El-Yousef, M., M.D., Davis, John M., M.D., Sekerke, Joseph H., Ph. D. 1973. Antagonistic Effects of Physostigmine & Methylphenidate in Man. *American Journal of Psychiatry*. p 1374.

Kimko, H. C., Cross, J. T., Abernathy, D. R., Pharmacokinetics and Clinical Effectiveness of Methylphenidate. *Clinical Pharmacokinet*. p. 457-70.

King, V. L., Brooner, R. K., Kidorf, M.S., et al. 1999. Attention Deficit Hyperactivity Disorder and Treatment Outcome in Opioid Users Entering Treatment. *J Nerv Ment Dis* 187(8): 487-495.

Leven, F. R., Evans S. M., Kleber H. D. 1999. Practical Guidelines for the Treatment of Substance Abusers with Adult-Attention Deficit Hyperactivity Disorder. Psychiatr Serv. P 1001-1003.

Szatmari, P. 1992. The Epidemiology of Attention-Deficit Hyperactivity Disorder. In "Child and Adolescent Psychiatric Clinics, Weiss G., guest ed. Philadelphia: W. B. Saunders.

Volkow, N. D., Ding, Y. S., Fowler, J. S., Wang, G. J., Logan, J., Gatley, J. S., Dewey, S., Ashby, C., Lieberman, J., Hitzemann, R., et al. 1995. Is Methylphenidate Like Cocaine? Studies on Their Pharmacokinetics and Distribution in the Human Brain. Arch Gen Psychiatry. 52(5): 456-463.

Appendix A First Order Multiple Scattering

The simplest approach to propagation through a random media is via single scatter theory. Single scatter theory retains its simplicity by incorporating the assumption that the field incident on a random media interacts with each scatterer only once and no multiple interactions occur among the scatterers that encompass the random media. This creates a scattered field, which is a power-like summation of scattered power from each scatterer.

In a previous section, the impulse response approach was introduced as an efficient means for computing the average intensity from a rough surface. In this section this impulse response technique is again extended to a tenuous (sparse) random media covering a rough surface. Like the radiative transfer extension, this method will use the convolutional approach. Unlike the extension from the radiative transfer theory, the following method applies the convolutional approach to a strongly scattering, yet tenuous media, which accounts for scattering out of the radial path with respect to the antenna; the

radiative transfer approach only accounts for strictly forward scattering and backscattering.

A.1 Review of Classical Single Scatter Theory

Assuming plane wave is incident on the scatterer, the incident field and the associated mean power density in free space are written as

$$\bar{\mathbf{E}}_i(\bar{\mathbf{r}}) = E_0 e^{-j\bar{\mathbf{k}}_i \cdot \bar{\mathbf{r}}} \hat{\mathbf{k}}_i, \quad \bar{\mathbf{S}}_i = \frac{1}{2} \left(\bar{\mathbf{E}}_i(\bar{\mathbf{r}}) \times \bar{\mathbf{H}}_i^*(\bar{\mathbf{r}}) \right) = \frac{1}{2\eta_0} |\bar{\mathbf{E}}_i(\bar{\mathbf{r}})|^2 \hat{\mathbf{k}}_i \quad (1)$$

where the incident direction is denoted by $\hat{\mathbf{k}}_i$ and the impedance of free space is given as

$$\eta_0 = \sqrt{\mu_0 / \epsilon_0}$$

In the development of the single scatter theory in a random media, the total received power, P_R , is written as a summation of the power scattered once by each particle. This simplification is due to the randomness of the scatterers in the media: all interference effects are neglected [Ishimaru, 1997]. The scattered field, $\bar{\mathbf{E}}_s(\bar{\mathbf{r}})$, and power density, $\bar{\mathbf{S}}_s$, due to the scatterer can be represented as

$$\bar{\mathbf{E}}_s(\bar{\mathbf{r}}) = \bar{f}(\hat{\mathbf{k}}_s, \hat{\mathbf{k}}_i) \frac{\exp(-jkR)}{R}, \quad \bar{\mathbf{S}}_s = \frac{1}{2} \left(\bar{\mathbf{E}}_s(\bar{\mathbf{r}}) \times \bar{\mathbf{H}}_s^*(\bar{\mathbf{r}}) \right) = \frac{1}{2\eta_0} |\bar{\mathbf{E}}_s(\bar{\mathbf{r}})|^2 \hat{\mathbf{k}}_s \quad (2)$$

where $\bar{f}(\hat{\mathbf{k}}_s, \hat{\mathbf{k}}_i)$ is the scattering amplitude, R is the range from the radar to the particle and the incident direction is denoted by $\hat{\mathbf{k}}_i$ and the scattering direction is denoted by $\hat{\mathbf{k}}_s$. Next we make several definitions concerning the radar cross-section of this scatterer. First is the differential radar cross-section, σ_d for given incident and scattered field directions

$$\sigma_d(\hat{k}_i, \hat{k}_s) = \lim_{R \rightarrow \infty} \left\{ \frac{R^2 S_s}{S_i} \right\} = |\bar{f}(\hat{k}_i, \hat{k}_s)|^2 \quad (3)$$

Consequently, the backscattering cross-section will be denoted as σ_b which will imply the following: $4\pi\sigma_d(\hat{k}_i, -\hat{k}_i)$. Another important cross-section in this work is the total observed cross-section (the scattering cross-section), σ_s . Denoting a differential unit of solid angle as $d\Omega$, this cross-section is written

$$\sigma_s = \iint_{4\pi} \sigma_d d\Omega$$

In the development of the single scatter theory in a random media, the total received power, P_R , is written as a summation of the power scattered once by each particle. This simplification is due to the randomness of the scatterers in the media: all interference effects are neglected [Ishimaru, 1997]. Consequently, summing up the power, P_R , returned from a continuum of scatterers to the radar from a random media due to the transmitted power, P_T , can be expressed using the standard radar equation

$$P_R = P_T \int_V \frac{\lambda^2 [G(\theta, \phi)]^2 \rho \sigma_b(\theta, \phi)}{(4\pi)^3 R^4} dV \quad (4)$$

where: λ = wavelength of the carrier

$G(\theta, \phi)$ = radar antenna gain in the direction (θ, ϕ) or \hat{k}_i

$\sigma_b(\theta, \phi)$ = particle backscattering cross section per unit area

dV = elemental volume

R = slant range from the radar to dV

ρ = particle density per unit volume

In this expression the transmitted power is assumed to be a continuous wave signal; consequently, the frequency dependence is monochromatic and monochromatic

dependence is implicit in the backscattering cross-section and the transmitting and receiving subsystems as well as any assumptions related to the intervening media.

In an attempt to improve this formulation, an accounting for the loss into the media from the source to the scatterer has results in *first order multiple scattering* and takes the a modified form with respect to the previous expression for the received power [Ishimaru, 1997]. This modified form can be described as follows. Once the absorption of the scatterer is included, this lost energy, represented by the absorption cross section, σ_a , is added to the scattering cross section to form the total or extinction cross section, $\sigma_t = \sigma_a + \sigma_s$. Hence, as a coherent wave travels through an uncorrelated random media, the coherent field is diminished by the total cross section of the scatterers encountered. Hence over a differential change in distance, the coherent power density can be written as in the following expression

$$\frac{\partial S_i(R; \hat{k}_i)}{\partial R} = -\sigma_t(R; \hat{k}_i) S_i(R; \hat{k}_i)$$

Hence the incident power density at the elemental scattering area, dV , at a depth R into the media can be written as

$$S_i(R; \hat{k}_i) = S_i(R_0; \hat{k}_i) \exp \left\{ - \int_0^R \rho \langle \sigma_t \rangle dR \right\}$$

where $\langle \sigma_t \rangle$ is the average total cross section. In terms of the transmitted power

$$P_i = \frac{P_T G(\theta, \phi) \exp \left\{ - \int_0^R \rho \sigma_t dR \right\}}{4\pi R^2}$$

Note the lack of any forcing or source terms since energy cannot scatter into the coherent field when the media is random with no correlation among the particles. The power received by the antenna is then expressed as

$$P_R = P_T \iiint_{\text{volume of scatterers}} \frac{\lambda^2 [G(\theta, \phi)]^2 \sigma_b(\theta, \phi)}{(4\pi)^3 R^4} \exp\left\{-2 \int_0^R \rho \sigma_t dR\right\} dV \quad (5)$$

This power density returned is identical to the power density predicted by the convolutional radiative transfer result; however, the integrations have been re-arranged and time dependence is ignored at this point.

A.2 The Scattered Pulse

In order to construct the response of the media to a scattered pulse, the correlation of the output-scattered fields must be derived. Loosely following the notation and development of Ishimaru [1997], a general expression for the correlation is found in the following equation

$$B_u(t_1, t_2) = \int_{-\infty}^{\infty} d\omega_1 \int_{-\infty}^{\infty} d\omega_2 U_i(\omega_1) U_i^*(\omega_2) \Gamma \exp\{-j(\omega_1 t_1 - \omega_2 t_2)\} \quad (6)$$

where $U_i(\omega)$ is the complex envelope of the incident wave form at the time harmonic frequency ω and Γ is the *two-frequency mutual coherence function*. The two-frequency mutual coherence function is the correlation of the time-varying, frequency domain transfer function, $H(\omega, t)$, at two different frequencies and two different times

$$\Gamma \equiv \Gamma(\omega_0 + \omega_1, \omega_0 + \omega_2; t_1, t_2) = \langle H(\omega_0 + \omega_1, t_1) H^*(\omega_0 + \omega_2, t_2) \rangle \quad (7)$$

Once the two-frequency mutual coherence is constructed, the scattered intensity is found when $t_1 = t_2 = t$ and $\Gamma \rightarrow \Gamma_0$ [Ishimaru, 1997]

$$I(t) = \int_{-\infty}^{\infty} d\omega_1 \int_{-\infty}^{\infty} d\omega_2 U_i(\omega_1) U_i^*(\omega_2) \Gamma_0 \exp\{-j(\omega_1 - \omega_2)t\} \quad (8)$$

In first order multiple scattering theory, the transfer function at a single frequency can be simply derived from the transform of the spatial scattering function $\bar{f}(\hat{k}_s, \hat{k}_i)$ modified by the loss in the media and gain of the antenna at the given frequency. For simplicity, antenna gain at a given frequency for monostatic operation can be represented as follows

$$G_R(\theta, \phi; \omega) = G_T(\theta, \phi; \omega) = G(\omega) \quad (9)$$

Note the monostatic assumption: transmitting and receiving directions are identical. Next, we rewrite the gain of the transmit antenna as

$$\frac{1}{4\pi} G_T(\hat{k}_i, \omega) = g_T^2(\hat{k}_i, \omega) \quad (10)$$

Additionally, assume that the gain on transmit and the effective aperture area on receive are represented by

$$\frac{\lambda^2}{4\pi} G_R(\omega) = g_R^2(\omega) \quad (11)$$

Assuming the media is stationary in time, the frequency domain transfer function at the single frequency ω , can be expressed as follows [Ishimaru, 1997]

$$H(\omega) = g_T(\omega) g_R(\omega) \tilde{F}(\omega) \frac{e^{-2jkR}}{R^2} \exp \left\{ -2 \int_0^R \rho \langle \sigma_t \rangle dR \right\} \quad (12)$$

where, the Fourier transform of the scattering function at a given frequency yields

$$\tilde{F}(\omega) = \tilde{F}(\omega; \hat{k}_s, \hat{k}_i) = \mathfrak{F} \{ \tilde{f}(\hat{k}_s, \hat{k}_i) \}$$

Once the two-frequency mutual coherence function is constructed, the backscattered intensity has been found

$$I(t) = \iiint_{\text{volume of scatterers}} \left[\int_{-\infty}^{\infty} A\left(\omega_1, t - \frac{2R}{c}\right) e^{j\omega_1 t} d\omega_1 \right] \left[\int_{-\infty}^{\infty} A\left(\omega_2, t - \frac{2R}{c}\right) e^{j\omega_2 t} d\omega_2 \right]^* \rho dV \quad (13)$$

where

$$A(t, \omega_n) = U_i(\omega_n) \tilde{F}(\omega_n; \hat{k}_s, \hat{k}_i) g_T(\omega) g_R(\omega) \frac{e^{-2jkR}}{R^2} \exp \left\{ -2 \int_0^R \rho \langle \sigma_t \rangle dR \right\}$$

$U_i(\omega_n) =$ the complex envelope of the incident signal at the frequency, ω_n

and the asterisk signifies the complex conjugate. When the bandwidth of the pulse is narrow with respect to the carrier frequency, the *narrow-band approximation* can be made. In this case, the scattering function, as a function of frequency, is roughly constant and can be evaluated at the center, carrier frequency. Once this narrow bandwidth approximation assumption is made, the only frequency dependence in the two-frequency mutual coherence function appears in the Fourier kernel. A change of variables to the difference frequency $\omega_d = \omega_1 - \omega_2$ yields a simpler expression. The two frequency mutual function for a narrow band input signal becomes [Ishimaru, 1997]

$$\Gamma_0 \approx |F(\omega_0)|^2 \frac{\exp\{j\omega_d 2R/c\}}{R^4} \rho dV \quad (14)$$

When a finite number of discrete scatterers is present, in contrast to the formulation above, the volume integration over the density of scatterers will be replaced with a discrete summation.

With the narrow beamwidth and narrow band approximations, the inverse transforms are easily performed and the backscattered waveform reduces to [Ishimaru, 1997]

$$\begin{aligned} I(t) &= \iiint_{\text{volume of scatterers}} \frac{\lambda^2 G^2(\theta, \phi)}{(4\pi)^3 R^4} \rho \sigma_b(\theta, \phi) \exp\left\{-2 \int_{R_1}^R \rho(\sigma_t) dR\right\} \left|u_i\left(t - \frac{2R}{c}\right)\right|^2 dV \\ &= \iiint_{\text{volume of scatterers}} \frac{\lambda^2 G^2(\theta, \phi)}{(4\pi)^3 R^4} \rho \sigma_b(\theta, \phi) \exp\left\{-2 \int_{R_1}^R \tilde{k}_e(R) dR\right\} P_T\left(t - \frac{2R}{c}\right) dV \end{aligned} \quad (15)$$

Rearranging the order of integration, this can be seen to be equivalent to the radiative transfer result derived in Chapter 3. Assuming the speed of light is the same everywhere, the radiative transfer approach yields

$$I(-\hat{r}; r, \theta, \phi, t) = \int_{r_{10} + \xi(x) \sec \theta_1}^{r_{10} + \xi(x) \sec \theta + d_1 \sec \theta} \sigma_b(\alpha) I_0\left(t - \frac{2\alpha}{c_0}\right) \exp\left\{-2 \int_{r_{10} + \xi(x) \sec \theta_1}^{\alpha} \tilde{k}_e(\mu) d\mu\right\} d\alpha$$

When we integrate this radiative transfer result over the surface, substitute for the incident intensity, simplify the limits and compensate for the effective receiving area of the antenna, identical results are realized for the radiative transfer (see Chapter 3) and the first order multiple scattering approaches.

$$P_R(t) = \int_0^\infty \int_0^{2\pi} \int_{R_1}^{R_2} \sigma_b(\alpha) \left\{ \frac{\lambda^2 G^2(\theta, \phi)}{(4\pi)^3 R^4} P_T \left(t - \frac{2\alpha}{c_0} \right) \right\} \exp \left\{ -2 \int_{R_1}^\alpha \tilde{k}_e(\mu) d\mu \right\} d\alpha \rho d\phi d\rho \quad (16)$$

In addition, note that the particle density per unit volume, ρ , is assumed to be unity.

Like the radiative transfer result, the first order multiple scattering result can accommodate a spatially varying velocity and may be re-cast into a convolutional, impulse response form when the narrow-band and narrow-beamwidth approximations are employed. More importantly, a further limitation of the radiative transfer approach has been identified: use of a narrow bandwidth approximation. This assumption is expected due to the use of constant forward and backscatter coefficients with respect to frequency in deriving the radiative transfer results. The use of the narrow beamwidth approximation has already been identified in the radiative transfer approach. However, using the full expression for two-frequency mutual coherence function, it is possible that the impulse response approach may be extended to broader bandwidth pulses in addition to broader beamwidth antenna patterns while maintaining some convolutional aspects. This premise is still under investigation.

STATISTICAL ANALYSIS OF THE NONHOMOGENEITY DETECTOR FOR NON-GAUSSIAN INTERFERENCE BACKGROUNDS

M. Rangaswamy

U.S. Air Force Research Laboratory/SNHE
80 Scott Drive
Hanscom AFB, MA 01731-2909
Tel:(781)377-2987, Fax:(781)377-8984
Email:Muralidhar.Rangaswamy@hanscom.af.mil

J.H. Michels and B. Himed

U.S. Air Force Research Laboratory/SNRT
26 Electronic Parkway
Rome, NY 13441
Tel:(315)330-4432, Fax: (315)330-2528
Email:James.Michels@rl.af.mil

ABSTRACT

We derive the nonhomogeneity detector (NHD) for non-Gaussian interference scenarios and present a statistical analysis of the method. The non-Gaussian interference scenario is assumed to be modeled by a spherically invariant random process (SIRP). We present two methods for selecting representative (homogeneous) training data based on our statistical analysis of the NHD for finite sample support used in covariance estimation. In particular, exact theoretical expressions for the NHD test statistic probability density function (PDF) and its moments are derived. Additionally, we note that for SIRP interference, a simple transformation of the NHD test statistic admits an elegant representation as the ratio of a central-F distributed random variable and a beta distributed loss factor random variable.

1. INTRODUCTION

An important issue in space-time adaptive processing (STAP) for radar target detection is the formation and inversion of the covariance matrix underlying the clutter/ interference. In practice, the unknown interference covariance matrix is estimated from a set of independent identically distributed (iid) target-free training data which is assumed to be representative of the interference statistics in a cell under test. Frequently, the training data is subject to contamination by discrete scatterers or interfering targets. In either event, the training data becomes nonhomogeneous. As a result, it is non representative of the interference in the test cell. Estimates of the covariance matrix from nonhomogeneous training data result in severely undernulled clutter. Consequently, CFAR and detection performance suffer. Significant performance improvement can be achieved by employing pre-processing to select representative training data.

The problem of target detection using improved training

strategies has been considered in [1–8]. The impact of non-homogeneity on STAP performance is considered in [8–11]. The works of [1–4, 8, 12] have addressed the use of the non-homogeneity detector (NHD) based on the generalized inner product (GIP) measure for STAP problems involving Gaussian interference scenarios. This work was extended significantly in [13, 14] to include the effects of finite sample support used for covariance matrix estimation. However, the corresponding problem for non-Gaussian interference scenarios has received limited attention.

In this paper, we derive the NHD for non-Gaussian interference scenarios, which can be modeled by spherically invariant random processes (SIRP) and present a statistical analysis of the resultant NHD test statistic. In general, the problem of non-homogeneity detection for SIRPs is quite difficult due to the fact that the underlying SIRP covariance matrix and characteristic PDF are unknown. For convenience, knowledge of the SIRP characteristic PDF is assumed in this paper.

2. PRELIMINARIES

Let $\mathbf{x} = [x_1 \ x_2 \ \dots \ x_M]^T$ denote a complex spherically invariant random vector (SIRV) having zero mean, positive definite Hermitian covariance matrix \mathbf{R} and characteristic PDF $f_V(v)$. The PDF of \mathbf{x} is given by [15]

$$f(\mathbf{x}) = \pi^{-M} |\mathbf{R}|^{-1} h_{2M}(q) \quad (1)$$

where $|\cdot|$ denotes determinant and

$$h_{2M}(w) = \int_0^\infty v^{-2M} \exp\left(-\frac{w}{v^2}\right) f_V(v) dv. \quad (2)$$

Every SIRV admits a representation of the form [16] $\mathbf{x} = \mathbf{z}V$, where \mathbf{z} has a complex-Gaussian PDF, $CN(0, \mathbf{R})$, and V is a statistically independent random variable with PDF

$f_V(v)$. In practice, \mathbf{R} and $f_V(v)$ are unknown. For the purpose of this paper, we assume knowledge of $f_V(v)$ and treat the problem of non-homogeneity detection with respect to unknown \mathbf{R} .

Previous work [1–4, 8, 12–14] employed the GIP based NHD for Gaussian interference scenarios. However, the GIP based method relying on the statistics of $Q = \mathbf{x}^H \hat{\mathbf{R}}^{-1} \mathbf{x}$ is unsuitable for SIRV interference scenarios. This is due to the fact that the covariance matrix estimate for this problem can be obtained to within a constant of the covariance matrix underlying the Gaussian component of the SIRV. Typically, this constant is unknown in practice. Consequently, the PDF of Q , its moments, and the threshold setting for the goodness-of-fit test proposed in [13] cannot be determined. Consequently, we seek a test statistic, which is invariant to the unknown scaling.

3. NONHOMOGENEITY DETECTOR FOR NON-GAUSSIAN INTERFERENCE SCENARIOS

Let $\mathbf{x} \sim \text{SIRV}[0, \mathbf{R}_T, f_V(v)]$ denote the complex SIRV test data vector, where \mathbf{R}_T is unknown. Further, \mathbf{x}_i , $i = 1, 2, \dots, K$ denote iid complex $\text{SIRV}[0, \mathbf{R}_x, f_V(v)]$ target free training data. For homogeneous training data, $\mathbf{R}_T = \mathbf{R}_x = \mathbf{R}$. The first step in deriving the NHD detector for SIRVs involves obtaining the maximum likelihood estimate of the underlying covariance matrix. This estimate is then used in a test statistic which exhibits maximal invariance with respect to the unknown scaling of the estimated covariance matrix. The resulting test statistic takes the form of a normalized adaptive matched filter (NAMF), which has been extensively analyzed in [17, 18] and references therein.

3.1. Covariance Matrix Estimation

The unknown covariance matrix is estimated from target free training data consisting of independent identically distributed SIRVs sharing the covariance matrix of the noise in the test cell. Maximum likelihood (ML) estimation of the covariance matrix for SIRVs was first considered in [19]. The work of [19] showed that covariance matrix estimation for SIRVs can be treated in the framework of a complete-incomplete data problem and pointed out that the maximum likelihood estimate of the covariance matrix is a weighted sample matrix. Since the problem does not permit a closed form solution, [19, 20] uses an iterative method known as the expectation-maximization (EM) algorithm. More precisely, let \mathbf{x}_i , $i = 1, 2, \dots, K$ denote independent identically distributed training data sharing the covariance matrix of the test data vector \mathbf{x} . The work of [19, 20] shows that the ML estimate of the covariance matrix is given by

$$\hat{\mathbf{R}} = \frac{1}{K} \sum_{i=1}^K c_i \mathbf{x}_i \mathbf{x}_i^H \quad (3)$$

where

$$c_i = -\frac{h'_{2M}(q_i)}{h_{2M}(q_i)} \quad (4)$$

$$h'_{2M}(w) = \frac{\partial h_{2M}(w)}{\partial w} = -h_{2M+2}(w)$$

and $q_i = \mathbf{x}_i^H \hat{\mathbf{R}}^{-1} \mathbf{x}_i$, $i = 1, 2, \dots, K$. Clearly the transcendental nature of the estimate precludes obtaining a closed form solution. Consequently, [19] used the EM algorithm to obtain an iterative solution to the problem. We adopt the approach of [19] for obtaining the covariance matrix estimate in this work. A derivation of the covariance matrix estimate is contained in Appendix A. It is shown in Appendix A that the EM algorithm at convergence produces an estimate which is to within a multiplicative constant of the covariance matrix estimate of the Gaussian component underlying the SIRV. Details pertaining to the initial start and convergence properties of the EM algorithm can be found in [19]. The next step is to use this estimate in a maximally invariant decision statistic for non-homogeneity detection.

3.2. Maximally Invariant NHD Test Statistic

The maximal invariant statistic for different scaling of test and training data is given by [17]

$$\Lambda_{NAMF} = \frac{|\mathbf{s}^H \hat{\mathbf{R}}^{-1} \mathbf{x}|^2}{[\mathbf{s}^H \hat{\mathbf{R}}^{-1} \mathbf{s}][\mathbf{x}^H \hat{\mathbf{R}}^{-1} \mathbf{x}]} \quad (5)$$

where $\mathbf{s} = \frac{1}{\sqrt{M}}[1 \ 1 \ \dots \ 1]^T$. Invariance properties of the test statistic of eq (5) and its geometrical representation have been studied in [17] and references therein for the case of Gaussian interference statistics using a sample covariance matrix estimate. In SIRP interference, however, each training data vector realization is scaled by a different realization of V . Consequently, maximal invariance of the test statistic of eq (5) afforded by the sample covariance matrix estimate no longer applies. This is due to the fact that the sample covariance matrix is no longer the maximum likelihood estimate of the covariance matrix for SIRV scenarios. However, using an estimated covariance matrix of the form of eq (3) restores the maximal invariance property of the test statistic of eq (5). This is due to the fact that the resultant covariance matrix estimate is to within a multiplicative constant of the covariance matrix corresponding to the Gaussian component of the SIRV.

3.3. PDF and Moments of the Non-Gaussian NHD Test Statistic

The PDF and moments of the NHD test statistic are readily determined in terms of the corresponding quantities of an equivalent random variable defined by

$$\Lambda_{eq} = \frac{\Lambda_{NAMF}}{1 - \Lambda_{NAMF}} \quad (6)$$

It has been shown in [17,21,22] that Λ_{eq} admits a representation as the ratio of an F-distributed random variable and a beta-distributed loss factor. In this effort, we are interested in the PDF of Λ_{NAMF} under the condition where no target is present in the test data vector \mathbf{x} . Specifically, it can be shown from the work of [17,21,22] that the PDF of Λ_{NAMF} is given by

$$f_{\Lambda_{NAMF}}(r) = \int_0^1 \frac{L(1-\gamma)f_{\Gamma}(\gamma)(1-r)^{L-1}d\gamma}{[1-\gamma r]^{L+1}} \quad (7)$$

where $L = K - M + 1$ and Γ is the loss factor random variable, whose PDF is given by

$$f_{\Gamma}(\gamma) = \frac{1}{\beta(L+1, M-1)} \gamma^L (1-\gamma)^{M-2}. \quad (8)$$

The mean of Λ_{NAMF} is somewhat difficult to calculate. Consequently, we work with the mean of Λ_{eq} given by

$$E(\Lambda_{eq}) = \frac{K}{(K-M)(M-2)}. \quad (9)$$

The statistical equivalence of Λ_{eq} to within a scalar of the ratio of a F-distributed random variable and a beta-distributed loss factor in that it permits rapid calculation of the moments of Λ_{eq} . More importantly, it is extremely useful in Monte-Carlo studies involving simulation of Λ_{NAMF} . For homogeneous training data, the use of (6) circumvents the need to explicitly generate the test data vector \mathbf{x} and the training data vectors used for covariance estimation. For large M and perforce K , significant computational savings can be realized from the method of (6). It is instructive to note that the PDF of Λ_{NAMF} as well as its mean depend only on M and K , which are under the control of a system designer, and not on nuisance parameters such as the true covariance matrix underlying the interference scenario. Furthermore, for $K \rightarrow \infty$ the mean of eq (9) converges to $E(\Lambda_{eq}) = \frac{1}{(M-2)}$, corresponding to the mean of an F-distributed random variable.

3.4. Goodness-of-Fit Tests

Since the PDF and mean of Λ_{NAMF} are known, a formal goodness of fit test can be used for non-homogeneity detection in non-Gaussian interference scenarios. In particular, we form empirical realizations of Λ_{NAMF} from each training data realization using a moving window approach. In this approach each training data vector is treated as a test cell data vector, whose covariance matrix is estimated from neighboring cell data according to eq (3). We then test for statistical consistency of these realizations of Λ_{NAMF} with the PDF of eq (7). For this purpose a convenient type-I error (typically between 0.01 and 0.1) given by

$$P_e = \int_0^1 \frac{f_{\Gamma}(\gamma)}{[1 + (1-\gamma)\eta]^L} d\gamma \quad (10)$$

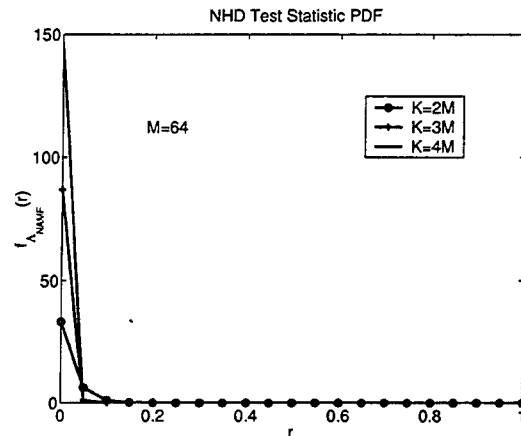


Fig. 1. NHD Test Statistic PDF

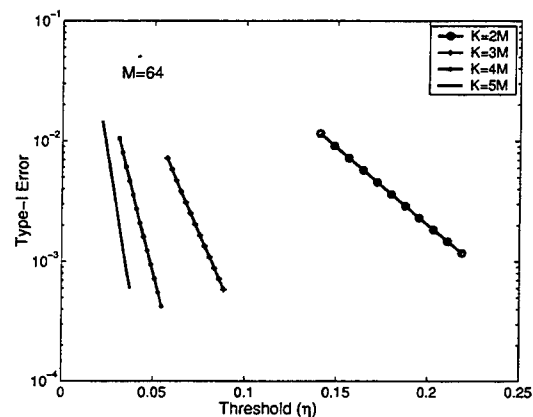


Fig. 2. Type-I Error vs Threshold for NHD Test Statistic

is chosen. The threshold, η , is determined by a numerical inversion of eq (10). Realizations of Λ_{NAMF} , which exceed η correspond to nonhomogeneous training data. A second test for training data nonhomogeneity is based on comparing each realization of Λ_{eq} with its theoretically predicted mean given by eq (9) and retaining those realizations which exhibit the least deviation. Performance analysis of these NHD methods is presented in the next section.

4. PERFORMANCE ANALYSIS

Performance of the goodness-of-fit test with simulated and measured data is presented here. Figure 1 shows the plot of the PDF of Λ_{NAMF} with K as a parameter. Observe that the variance of Λ_{NAMF} decreases with increasing K . Figure 2 shows a plot of the Type-I error versus the threshold, η , with K as a parameter. For a given type-I error, the threshold decreases with increasing K , in conformance with the results of Figure 1. Figure 3 shows the performance of the goodness-of-fit test for simulated homogeneous data

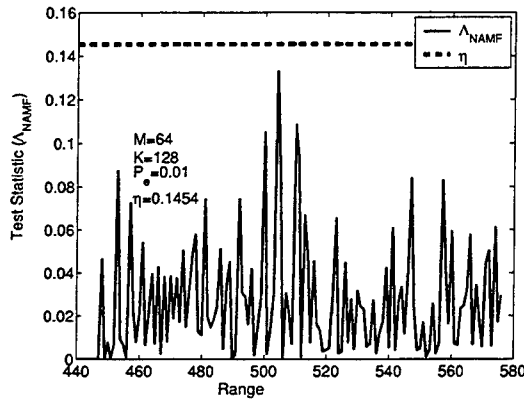


Fig. 3. Type-I Error vs Threshold for NHD Test Statistic

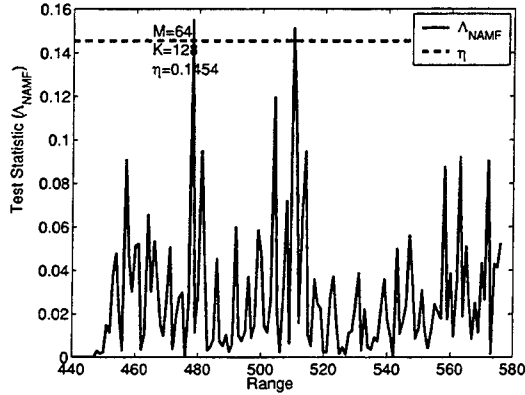


Fig. 4. Type-I Error vs Threshold for NHD Test Statistic

from the K-distribution [15] with shape parameter 0.5 using the covariance estimate of eq (3). The results reveal the lack of nonhomogeneity in that no realization of Λ_{NAMF} exceeds the threshold. Figure 4 shows the performance of the goodness-of-fit test in non-homogeneous K-distributed clutter with shape parameter 0.5. The K-distributed amplitude PDF is given by

$$f_R(r) = \frac{\beta^{\alpha+1} r^\alpha}{2^{\alpha-1} \Gamma(\alpha)} K_{\alpha-1}(\beta r) \quad r \geq 0, \beta, \alpha > 0 \quad (11)$$

where β and α are the distribution scale and shape parameters, respectively, $K_\nu(\cdot)$ is the modified Bessel function of the second kind of order ν and $\Gamma(\cdot)$ is the Euler-Gamma function. Small values of α result in heavy-tails for the PDF of (11). The corresponding $f_V(v)$ and $h_{2M}(\cdot)$ are given by

$$\begin{aligned} \frac{2\beta}{\Gamma(\alpha)} (\beta v)^{2\alpha-1} \exp(-\beta^2 v^2) & \quad 0 \leq v \leq \infty \\ h_{2M}(w) = \frac{2\beta^{2M}}{\Gamma(\alpha)} (\beta \sqrt{w})^{\alpha-M} K_{\alpha-M}(2\beta \sqrt{w}) & \quad (12) \end{aligned}$$

Nonhomogeneity of the data is evident in those range bins where Λ_{NAMF} exceeds η . Figure 5 shows the results of the goodness of fit test for the MCARM data [23] using acquisition 220 on Flight 5, cycle e for 8 channels and 16 pulses.

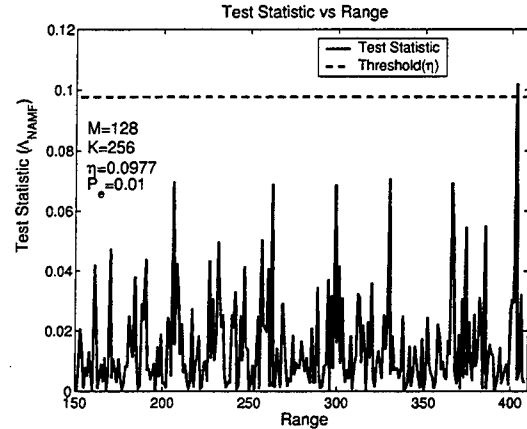


Fig. 5. NHD Test Statistic vs Range

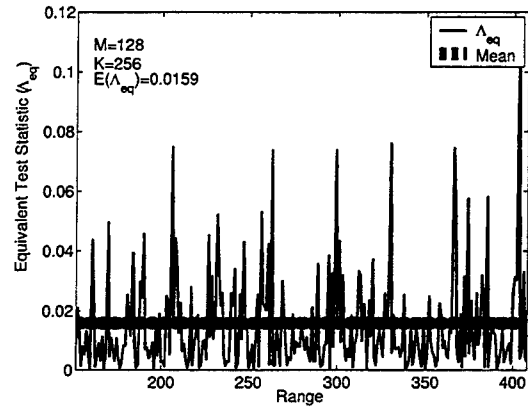


Fig. 6. NHD Test Statistic vs Range

The NHD test statistic, Λ_{NAMF} , and the threshold, η , are plotted as a function of range. Statistical analysis of the data indicates that the data is well approximated by the Gaussian distribution. This fact considerably simplifies the analysis in that the covariance matrix estimate is simply the sample covariance matrix. Non-homogeneity of the training data is evident in those bins for which Λ_{NHD} exceeds η . Figure 6 shows the results from the selection procedure based on comparing the empirically formed Λ_{eq} with its theoretically predicted mean given by eq (9). The data set used for this example is identical to the data used in Figure 5. Relevant test parameters are reported in the plot. We observe a significant increase in the number of deviations from the theoretically predicted mean given by eq (9). This is due to the fact that we are dealing with a limited number of realizations of the NHD test statistic.

5. CONCLUSION

This paper provides a rigorous statistical characterization of the NHD for non-Gaussian interference scenarios which

can be modeled as a spherically invariant random process. It is noted that the NHD statistic admits a simple representation in terms of a ratio of an F distributed random variable and a beta distributed loss factor. A formal goodness-of-fit test based on this representation, which follows a randomized F-distribution, is derived. Performance analysis of the method is considered in some detail using measured data from the MCARM program. The illustrative examples validate the approach taken and confirm the results. Future work would include extensive performance analysis using simulated and measured data showing the resulting impact on STAP performance. The performance of several STAP algorithms in Gaussian and non-Gaussian interference scenarios has been considered in [18]. Future work will address performance of the methods treated in [18] with suitable NHD pre-processing.

6. ACKNOWLEDGMENT

This work was supported by the Air Force Office of Scientific Research (AFOSR) through a U.S. Air Force Research Laboratory contract under contract number F30602-00-C-0231, AFRL in-house research programs and AFOSR project 2304E8.

7. REFERENCES

- [1] P. Chen, "On testing the equality of covariance matrices under singularity," tech. rep., for AFOSR Summer Faculty Research Program, Rome Laboratory, August 1994.
- [2] P. Chen, "Partitioning procedure in radar signal processing problems," tech. rep., for AFOSR Summer Faculty Research Program, Rome Laboratory, August 1995.
- [3] W. Melvin, M. Wicks, and R. Brown, "Assessment of multichannel airborne radar measurements for analysis and design of space-time adaptive processing architectures and algorithms," in *Proceedings of the IEEE National Radar Conference*, (Ann Arbor, MI), 1996.
- [4] W. Melvin and M. Wicks, "Improving practical space-time adaptive radar," in *Proceedings of the IEEE National Radar Conference*, (Syracuse, NY), 1997.
- [5] D. Rabideau and A. Steinhardt, "Improving the performance of adaptive arrays in nonstationary environments through data-adaptive training," in *Proceedings of the 30th Asilomar Conference on Signals, Systems, and Computers*, (Pacific Grove, CA), 1996.
- [6] D. Rabideau and A. Steinhardt, "Power selected training for false alarm mitigation in airborne radar," in *Proceedings of the Adaptive Sensor Array Processing Workshop (ASAP)*, (MIT Lincoln Laboratory, Lexington, MA), 1996.
- [7] D. Rabideau and A. Steinhardt, "Improved adaptive clutter cancellation through data-adaptive training," *IEEE Trans. on Aerospace and Electronic Systems*, vol. AES-35, no.3, pp. 879-891, 1999.
- [8] B. Himed, Y. Salama, and J. H. Michels, "Improved detection of close proximity targets using two-step NHD," in *Proceedings of the International Radar Conference*, (Alexandria, VA), 2000.
- [9] R. Nitzberg, "An effect of range-heterogenous clutter on adaptive Doppler filters," *IEEE Trans. on Aerospace and Electronic Systems*, vol. 26, no.3, pp. 475-480, 1990.
- [10] W. L. Melvin, J. R. Guerci, M. J. Callahan, and M. C. Wicks, "Design of adaptive detection algorithms for surveillance radar," in *Proceedings of the International Radar Conference*, (Alexandria, VA), 2000.
- [11] W. L. Melvin, "Space-time adaptive radar performance in heterogenous clutter," *IEEE Trans. on Aerospace and Electronic Systems*, vol. 36, no.2, pp. 621-633, 2000.
- [12] P. Chen, W. Melvin, and M. Wicks, "Screening among multivariate normal data," *Journal of Multivariate Analysis*, vol. 69, pp. 10-29, 1999.
- [13] M. Rangaswamy, B. Himed, and J. Michels, "Statistical analysis of the nonhomogeneity detector," in *Proceedings of the 34th Asilomar Conference on Signals, Systems, and Computers*, (Pacific Grove, CA), 2000.
- [14] M. Rangaswamy, B. Himed, and J. Michels, "Performance analysis of the nonhomogeneity detector for STAP applications," in *Proceedings of the 2001 IEEE Radar Conference*, (Atlanta, GA), May 2001.
- [15] M. Rangaswamy, J. Michels, and D. Weiner, "Multichannel detection for correlated non-Gaussian random processes based on innovations," *IEEE Trans. on Signal Processing*, vol. SP-43, pp. 1915-1922, 1995.
- [16] K. Yao, "A representation theorem and its applications to spherically invariant random processes," *IEEE Trans. on Information Theory*, vol. IT-19, pp. 600-608, 1973.
- [17] S. Kraut, L. L. Scharf, and L. McWhorter, "Adaptive subspace detectors," *IEEE Trans. on Signal Processing*, vol. 49, pp. 1-16, 2001.

- [18] J. Michels, B. Himed, and M. Rangaswamy, "Performance of STAP tests in Gaussian and Compound-Gaussian Clutter," *Digital Signal Processing*, vol. 10, no.4, pp. 309–324, 2000.
- [19] R. J. Little and D. B. Rubin, *Statistical Analysis With Missing Data*. New York: John Wiley & Sons, 1987.
- [20] M. Rangaswamy and J. H. Michels, "Adaptive Processing in Non-Gaussian Noise Backgrounds," in *Proceedings of the Ninth IEEE Workshop on Statistical Signal and Array Processing*, (Portland, OR), 1998.
- [21] J. Michels, M. Rangaswamy, and B. Himed, "Performance of STAP tests in compound Gaussian clutter," in *Proceedings of the First IEEE Workshop on Sensor Array and Multichannel Processing (SAM-2000)*, (Cambridge, MA), 2000.
- [22] C. Richmond, "Performance of the adaptive sidelobe blanker detection algorithm in homogeneous environments," *IEEE Trans. on Signal Processing*, vol. SP-48, no.5, pp. 1235–1247, 2000.
- [23] MCARMDATA, "View [www@http://128.132.2.229](http://128.132.2.229)." Data from the Multichannel Airborne Radar Measurement Program of the U.S. Air Force Research Laboratory, Rome, NY.
- [24] J. P. Burg, D. G. Luenberger, and D. L. Wenger, "Estimation of structured covariance matrices," *Proceedings of the IEEE*, vol. 70, No.9, pp. 963–974, 1982.

Appendix A: EM Algorithm for Covariance Matrix Estimation

We discuss the maximum likelihood estimation of the SIRV covariance matrix in this appendix. Let \mathbf{X} denote a data matrix, whose columns \mathbf{x}_i , $i = 1, 2, \dots, K$ are independent identically distributed target-free training data vectors, which are distributed as $SIRV[0, \mathbf{R}_x, f_V(v)]$. The likelihood function for estimating \mathbf{R} is given by

$$g[\mathbf{X}|\mathbf{R}] = \prod_{i=1}^K \pi^{-M} |\mathbf{R}|^{-1} h_{2M}(q_i). \quad (13)$$

Direct maximization of the likelihood function of (13) over \mathbf{R} is rendered difficult due to the fact that there is missing information. Consequently, it is helpful to treat the problem in the context of a complete-incomplete data problem [19]. Recall from the representation theorem for SIRVs [16] that $\mathbf{x}_i = \mathbf{z}_i V_i$, where \mathbf{z}_i , $i = 1, 2, \dots, K$ are statistically independent $CN(0, \mathbf{R})$ random vectors, and V_i , $i = 1, 2, \dots, K$ are statistically independent random variables with PDF $f_V(v)$. For this problem, the complete data

is either \mathbf{z}_i , V_i , $i = 1, 2, \dots, K$ or \mathbf{x}_i , V_i , $i = 1, 2, \dots, K$. However, the observed data \mathbf{x}_i , $i = 1, 2, \dots, K$, contains no explicit information about V_i , $i = 1, 2, \dots, K$ and thus constitutes the incomplete data. The complete data likelihood function is given by the joint PDF of \mathbf{x}_i , V_i , $i = 1, 2, \dots, K$, which is expressed as

$$g_c[\mathbf{X}, V_i|\mathbf{R}] = \prod_{i=1}^K f(\mathbf{x}_i|V_i) \prod_{i=1}^K f(v_i) \quad (14)$$

Taking the natural logarithm of (14) yields the complete-data log-likelihood function of the form

$$L[\mathbf{X}, V_i|\mathbf{R}] = -KM \log(\pi) - K \log(|\mathbf{R}|) - \sum_{i=1}^K q_i v_i^{-2} + \sum_{i=1}^K \log[v_i^{-2M} f(v_i)]. \quad (15)$$

Note that given an initial estimate of \mathbf{R} denoted by $\hat{\mathbf{R}}$, the quantity,

$$E\{\log[v_i^{-2M} f(v_i)]|\hat{\mathbf{R}}\} \quad (16)$$

depends only on $\hat{\mathbf{R}}$ and not on \mathbf{R} . Consequently, the relevant terms for the maximization over \mathbf{R} are given by

$$L_1[\mathbf{X}, V_i|\mathbf{R}] = -K \log(|\mathbf{R}|) - \sum_{i=1}^K q_i v_i^{-2} \quad (17)$$

The missing data, v_i , $i = 1, 2, \dots, K$, are assumed to be missing at random (MAR) [19]. Consequently, given an initial estimate of \mathbf{R} denoted by $\hat{\mathbf{R}}$, the complete data sufficient statistic [19] is given by

$$c_i = E[V_i^{-2}|\hat{\mathbf{R}}, \mathbf{x}_i]. \quad (18)$$

Note that $f(v_1) = f(v_2) = \dots = f(v_K) = f_V(v)$ (since v_i , $i = 1, 2, \dots, K$ are independent identically distributed random variables). Therefore,

$$f_{V_i|\mathbf{x}_i, \hat{\mathbf{R}}}(v_i|\mathbf{x}_i, \hat{\mathbf{R}}) = \frac{f(\mathbf{x}_i|v_i, \hat{\mathbf{R}}) f_V(v_i)}{f_{\mathbf{x}_i|\hat{\mathbf{R}}}(\mathbf{x}_i|\hat{\mathbf{R}})}. \quad (19)$$

However,

$$\frac{f(\mathbf{x}_i|v_i, \hat{\mathbf{R}}) f_V(v_i)}{f_{\mathbf{x}_i|\hat{\mathbf{R}}}(\mathbf{x}_i|\hat{\mathbf{R}})} = \frac{v_i^{-2M} \exp(q_i v_i^{-2}) f(v_i)}{h_{2M}(q_i)}. \quad (20)$$

Consequently,

$$c_i = E[V_i^{-2}|\hat{\mathbf{R}}, \mathbf{x}_i] = -\frac{h'_{2M}(q_i)}{h_{2M}(q_i)}. \quad (21)$$

Having specified the complete data sufficient statistic, we seek the maximization of (17). For this purpose, we reproduce the following matrix differentiation identities from [24].

$$\begin{aligned} \delta[\mathbf{R}^{-1}] &= -\mathbf{R}^{-1} \delta[\mathbf{R}] \mathbf{R}^{-1} \\ \delta[\log|\mathbf{R}^{-1}|] &= -\text{tr}\{\mathbf{R}^{-1} \delta[\mathbf{R}]\} \end{aligned} \quad (22)$$

Further, we recognize that $q_i = \sum_{i=1}^K \text{tr}[\mathbf{R}^{-1} \mathbf{x}_i \mathbf{x}_i^H]$. Consequently,

$$\delta L_1[\mathbf{X}, V_i | \mathbf{R}] = K \text{tr}\{\mathbf{R}^{-1} \delta[\mathbf{R}]\} - \text{tr}[\mathbf{R}^{-1} \delta[\mathbf{R}] \mathbf{R}^{-1} \sum_{i=1}^K c_i \mathbf{x}_i \mathbf{x}_i^H]. \quad (23)$$

Maximization of (17) results from setting (23) equal to zero. Therefore, the maximum likelihood estimate of \mathbf{R} is given by

$$\hat{\mathbf{R}} = \frac{1}{K} \sum_{i=1}^K c_i \mathbf{x}_i \mathbf{x}_i^H. \quad (24)$$

Clearly the transcendental nature of the estimate precludes obtaining a closed form solution.

In summary, the EM algorithm for the problem of covariance matrix estimation considered here consists of the following steps.

1. E-Step: Given an initial estimate of \mathbf{R} denoted by $\hat{\mathbf{R}}$, calculate c_i for $i = 1, 2, \dots, K$.
2. M-Step: Calculate $\hat{\mathbf{R}} = \frac{1}{K} \sum_{i=1}^K c_i \mathbf{x}_i \mathbf{x}_i^H$.
3. Iterate until convergence. Convergence is determined through a suitable error criterion.

In this paper, the convergence criterion is an error of 10^{-6} defined to be the absolute value of the difference between the values of $\hat{\mathbf{R}}$ resulting from two successive iterations. Convergence of the algorithm is dictated by the choice of the initial estimate of \mathbf{R} . Any positive definite Hermitian matrix is suitable for the initial estimate of \mathbf{R} . Two choices, that arise readily are the $M \times M$ identity matrix and the sample covariance matrix given by $\mathbf{S} = \frac{1}{K} \sum_{i=1}^K \mathbf{x}_i \mathbf{x}_i^H$. We employ the latter choice in this paper due to the fact that it yields faster convergence.

The simulated data examples considered in this paper involve the calculation of the modified Bessel function of the second kind for specifying $h_{2M}(\cdot)$ and its derivative. Numerical errors in their calculation for $\alpha = 0.1$ tend to be rather large. Consequently, convergence of the algorithm is extremely slow for $\alpha = 0.1$.